Two-Dimensional Modelling of Novel Back-Contact Solar Cells

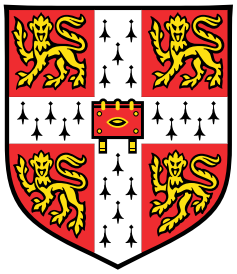

Robin D. Lamboll

Department of Physics
University of Cambridge

This dissertation is submitted for the degree of
Doctor of Philosophy

Christ's College

October 2017

I would like to dedicate this thesis to my parents for a lifetime of teaching.

Declaration

I am the author of this dissertation and hereby give the University the right to make my dissertation available in print form.

My dissertation is my own original work and a product of my own research endeavours and includes nothing which is the outcome of work done in collaboration with others except as declared in the Acknowledgements and specified in the text. I hereby assert my moral right to be identified as the author of the dissertation.

The deposit and dissemination of my dissertation by the University does not constitute a breach of any other agreement, publishing or otherwise, including any confidentiality or publication restriction provisions in sponsorship or collaboration agreements governing my research or work at the University or elsewhere.

Robin D. Lamboll
October 2017

Acknowledgements

I am grateful for funding by the Engineering and Physical Sciences Research Council (EPSRC) and detailed supervision by Neil Greenham. There were also many insightful theoretical discussions with Richard Friend, Felix Descheler, Johannes Richter and Luis Pazos-Outón.

As a primarily computational work, it is dependent on experimental data from dedicated experimentalists, so I am also grateful to Mejd Alsari-Almheiri, Greg Tainter and Monika Szumiło for devices and photocurrent microscopy data, to Mojtaba Abdi-Jalebi and Aditya Sadhanala for photothermal deflection spectroscopy measures, and Johannes Richter for spectroscopy data. They provided the actual physics that allows this work to say anything about the real world.

I'm also thankful to Alex Crook for helping me resolve many computational issues and to Girish Lakhwani for setting me up with drift-diffusion simulations. I'm thankful to Richard Gymer and Radoslav Chakalov for helping me manage experiments and access the right equipment. I'd also like to thank Gilly Walker, Alison Barker and Rachel Henderson for admin work and encouraging me to spend money.

I would like to thank Zhongyang Xing, Darshana Joshi, Sam Schott, Kee Hoon Kang Mejd Alsari-Almheiri, Angela Wittmann and Ned Booker for exposing me to world cuisine, and to them and other labmates who have offered me friendship over this period. Finally I would like to thank my parents again, for a whole thesis-worth of things.

Abstract

This dissertation computationally and analytically investigates ways to model solar cells when the lateral motion of charge carriers and light are relevant. We focus on back-contact perovskite solar cells as an example system, and assess the experimental technique of scanning photocurrent microscopy as a means to investigate them.

Solar cells are three-dimensional objects frequently modelled as being one-dimensional. However, for laterally variable designs of solar cell or if the cell is only illuminated at one point, one-dimensional modelling is insufficient. In the first study, some conditions for reducing the complexity of multi-dimensional drift-diffusion simulations are investigated for a back-contact perovskite solar cell. This frequently occurs if the system length is many times the height and when less than half the charges that are generated recombine, although there is deviation from these rules near the edges of electrodes. Analytic expressions for the relationship in both the low extraction velocity and high extraction velocity regimes are demonstrated, and the conditions where these approximations break down are investigated. These findings are then applied a point-excited film with an extended electrode, a problem encountered during scanning photocurrent microscopy. It is demonstrated that we expect the current recorded in this case to decay exponentially with the distance between the excitation point and the electrode, with a decay constant that can be related to device parameters. The characteristic equilibration time for the system to reach this current, which we show can be extracted from the phase delay in a lock-in amplifier measurement, is demonstrated to increase linearly with distance. Between this gradient and the exponent, information about the diffusion and recombination mechanics can be extracted from a wide variety of systems.

Photon recycling is the process in solar cells whereby photogenerated carriers recombine to generate light that is absorbed again within the solar cell. In the second section, we apply the findings of the first section to show that experimental results published elsewhere are best explained by photon recycling in methylammonium lead iodide perovskite back-contact solar cells. However we do not have an established theoretical model for long-ranged lateral optical transport in these solar cells. Three models are developed: a bimolecular model for unscattered, coherent transport; a photon diffusion model for frequently scattered, noncoherent light; and a monomolecular, assisted-diffusion model. The modal nature of

coherent optical transport is considered and modifications to previous one-dimensional theories are made. The nature of the photon diffusion model is discussed, as are theoretical shortcomings of this and the assisted-diffusion model. All three models are then solved numerically and compared to experimental results. The low-scattering photon diffusion models correspond well to the experiment.

The third investigation involves the performance of different architectures of back-contact perovskite solar cells. These cells potentially offer increased current due to less shadowing by front electrodes. We compare them to each other and to traditional vertical structures. It is found that, in terms of internal transport, the back-contact solar cells give less efficient performance than the vertical design. The best of the back-contact cells investigated is a flat interdigitated design. The increase in efficiency from optical factors would have to exceed 10% for the overall efficiency of back-contact cells to be higher than vertical devices.

We develop a model of photon recycling appropriate for short-ranged, bulk 2D transport and demonstrate that in our perovskite systems under uniform illumination, it produces little change in predicted power conversion efficiency (although a small change in short-circuit voltage) when compared with the standard drift-diffusion equations with the second-order recombination constant adjusted.

Table of contents

Chapter 1

Introduction

The world grows warmer, suffocates
As reddened light re-radiates.
Instead of burying drill-heads in the ground
Let's use the profusion of sun that abounds.
Here, to stimulate great solar sales
We'll simulate grates on solar cells

A solar cell changes light into an excitement:
A travelling electron and hole where you'd expect one
This e and this h will diffuse and displace
(If they feel an E-field), until one of two fates
Be collected at electrodes or entwine, recombine
As they bleed out in heat or unite into light.
The first case is worse than a waste,
But scintillating is exciting
Absorbed again, you're photon recycling.
This PhD will model all three in 2D.

The next chapter gives background theory
Introduces perovskites, our substance of query
Derives our equations of drift and diffusion
Outlines computational means of solution
Then thermodynamics of photon recycling
Are briefly outlined, we hope it's enlightening.

In chapter three, we take the 3D cells
And make 1D expressions that compress it quite well
And show that even with point illumination
The behaviour is modelled by a simple equation.

Furthermore, chapter four adds in spreading light
We develop three models to match perovskites'
Long-range behaviour, find we must factor in
Photon diffusion with low scattering.

In chapter five, we've applied this to back-contact cells
But find that the vertical work just as well.
We check how recycling makes charge rearrange
But uniform illumined cells show little change.

Chapter six has conclusions and work still to do
And then we will end with an appendix or two
Of extra maths that you don't have to read
So that's our structure, now let's proceed.

Or, in prose

In the face of growing problems from climate change, humanity seeks energy sources other than burning fossil fuels. The most prominent source of available energy is sunlight, underpinning the web of life on Earth's surface. Fossil fuels, biofuels and wind power are all indirect means of harnessing this. Photovoltaic solar cells can directly convert sunlight into electricity, without moving parts or negative environmental effects during operation, and can in principle deliver many times more energy than humans currently use. However, while solar power use is increasing exponentially, continuous technological and structural development of cell design is needed to financially motivate further investment as supply management and storage costs increase. This development requires the cooperation of materials scientists, engineers, physicists and interdisciplinary researchers to develop both the raw materials for solar cells, the interfaces between materials and the optimal architectures that these materials fit into.

This thesis bridges the gap between the pure modelling community, where detailed simulations of specific cell designs are considered, and the experimental community, where results are often considered in the context of greatly simplified, one-dimensional models of device behaviour. Real solar cells are not laterally uniform and may require both lateral and vertical modelling of the two charge carriers, mobile electrons and holes. There may also be effects resulting from 'photon recycling', whereby light absorbed in one place is re-emitted and absorbed elsewhere in the solar cell. Ironically, this is a close analogue of the greenhouse gas effect, the primary driver of climate change. We will consider how this effect can influence measurements and device performance.

In the next chapter, we will go through the background theory and introduce perovskites, a promising materials group for solar cells applications. These are a highly active area of research, where optimisation of cell design has yet to occur. Since this is a computational study, we will also outline here the computational frameworks used to investigate devices.

In chapter 3 we study how and when 1D expressions can be used to accurately model solar cell performance under both uniform illumination and point illumination. We will explain how to extract device parameters from point illumination measurements.

In chapter 4, we will investigate ways to incorporate optical transport in the point illumination model developed earlier. Several different models will be developed and compared with experimental results.

In chapter 5 we will look at different cell architectures for perovskite back-contact solar cells and compare them to vertical devices. A model for including photon recycling in a 2D drift-diffusion framework will also be developed.

Finally, we will write up our conclusions and further work. There are also two appendices with additional mathematical discussion of how to judge when models fit and how to relate results to experimental outputs.

Chapter 2

Background theory

2.1 Solar cell basics

Solar cells output power when light shines on them. There are many physical systems that do this, but the most commercially successful to date has been silicon solar cells, so we will outline the basic physics and measurement procedures with regard to them.

Silicon solar cells absorb light, which excites an electron out of the mostly-full valence band, into the mostly-empty conduction band. We can generally treat the place left behind in the valence band as a positively charged particle that moves when other electrons fill the space in, called a hole. The cell consists of at least two sections with different levels of impurities, or dopants. These result in different energy levels for the bands that encourages electrons to flow into one portion of the cell and holes into another. This results in a potential difference across the cell, and when electrodes are attached to the system, a current can flow through the external circuit [114].

Solar cell operation is characterised by the parameters V_{oc} – the voltage at open-circuit ($J = 0$), J_{sc} – the current density at short-circuit ($V = 0$), and FF, the fill factor. These values are illustrated in figure 2.1. Multiplying all three values together (or equivalently, multiplying J and V at the maximum power point) gives the total power output per unit area, which is most usefully expressed as a fraction of the total intensity of incident light. This is called the power conversion efficiency (PCE). Generally speaking, these values are quoted for a cell illuminated with a characteristic spectrum and intensity of sunlight passing through 1.5 typical atmospheres (air mass 1.5, AM1.5), based on measurements by NREL and considered an average value for the irradiance hitting the surface of the USA [116, 132]. The intensity of this spectrum is is often referred to as ‘one sun’.

Solar cells do not absorb all incident light, and primarily absorb light with energy higher than their bandgap. Above-bandgap radiation will generate ‘hot’ carriers with high amounts

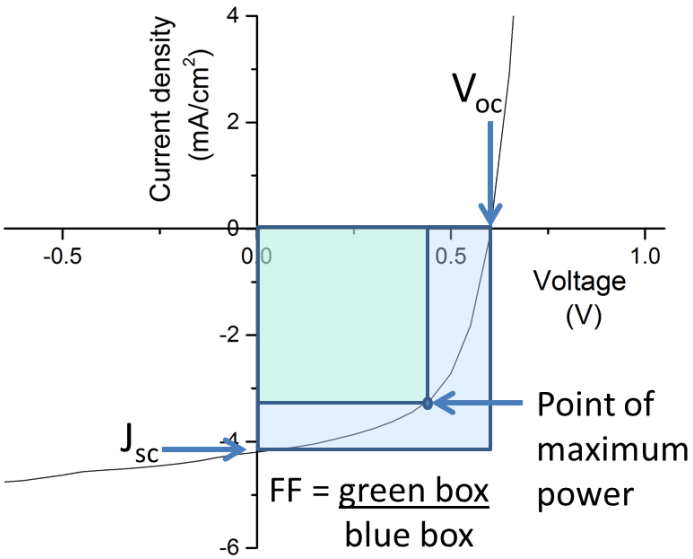

Fig. 2.1 Example voltage-current density plot, illustrating the closed-circuit current density (J_{sc}), open-circuit voltage (V_{oc}) and fill factor (FF, ratio of the maximum power output to $V_{oc}J_{sc}$). The data is from an organic solar cell made of P3HT and PCBM, under 1 sun illumination but is purely illustrative.

of kinetic energy, however the carriers will soon cool to the band edge and so the voltage that can be extracted is usually limited to this value. Maximising the total power output gives us the Shockley-Queisser limit of efficiency for a solar cell, which balances the total incoming energy with the internal losses and required black-body radiation [145]. This limit of just over 30% can be overcome if the absorption onset is not tied to the maximum energy extracted, as happens in multi-junction cells (where different layers of the junction can extract energy from different wavelengths) or due to mechanisms like multiple exciton generation [119]. The limit will also be affected by the precise illuminating spectrum.

To test solar cells, we want a reliable and constant source of 'sunlight'. The device used for testing solar cells, the solar simulator, has a characteristic emission spectrum but variable intensity. To investigate a cell with the same internal excitation as under standardised sunlight, we must calculate the spectral mismatch.

The response function of the cell to incident light of different wavelengths is investigated under zero applied bias. This is referred to as the external quantum efficiency (EQE), 'external' because we normalise by the incident light not the absorbed light and 'quantum'

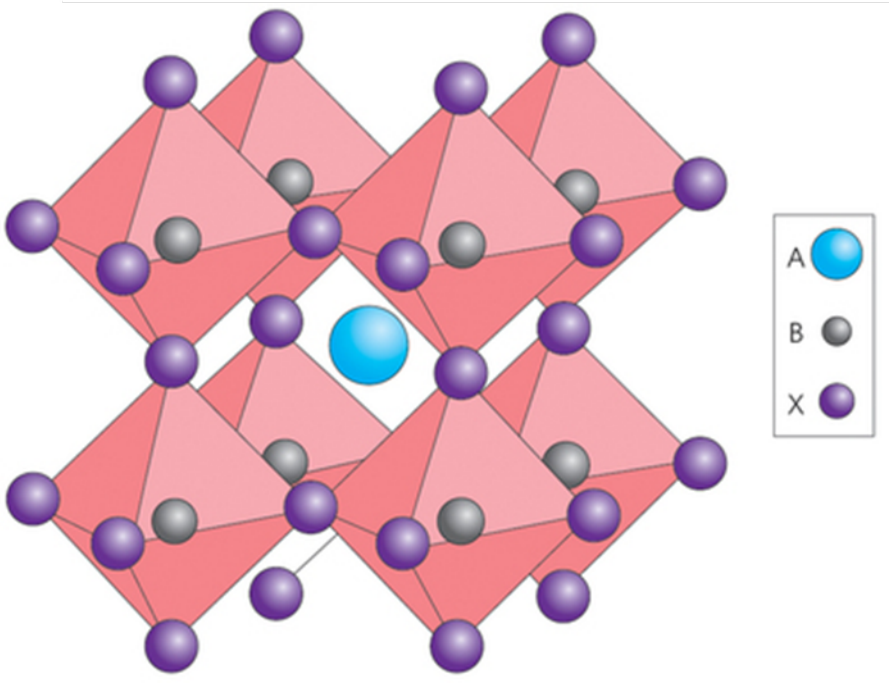

Fig. 2.2 Diagram of a perovskite crystal structure, taken from [59].

because we are interested in the number of electrons out, not the power they carry. We can then calculate the difference between the response to the spectrum the device is actually exposed to and the ideal AM1.5 spectrum. We then modify the intensity of light from the solar simulator so that it creates the same concentration of carriers inside the device as we would get under the AM1.5 spectrum, and measure the JV curve as in figure 2.1.

2.2 Perovskite solar cells

Perovskites are the class of crystal structure found in calcium titanate, found in compounds with the formula ABX_3, where X is an anion and A and B are cations of different sizes (A being larger than B) [59]. There are several slight crystallographic variants [69], but an image of the traditional cubic form can be found in figure 2.2.

The ions can be either all inorganic or mixed organic-inorganic, usually with A being organic. The crystal structure is often solution-processable. Some members of this crystal structure, particularly organic-lead halide cells, have been shown to work as a new variety of highly-efficient thin solar cells that have gained tremendous interest since 2013 [147, 128], following their rapid improvements in efficiency from 13% up to over 20% [117], which is unparalleled for a solution-processable material. Initially they were suggested as a sensitiser placed in small quantities on a titanium dioxide frame in dye-sensitised solar cells [81] with

impressive 8% efficient dye-sensitised cells published in 2009 [82]. However Lee *et al.* found they were more efficient when the conductive TiO_2 was replaced with nonconductive alumina and recognised the perovskites themselves were transporting carriers over long distances [89]. This paved the way for even more efficient bulk-perovskite solar cell. They are now investigated as the bulk material by a large and growing field of researchers, although many efficient designs still feature a mesoporous framework to assist in carrier transport and as a physical scaffold for device manufacture [147, 31].

For solar cell applications, the main perovskites of interest are lead-iodides, with either methylammonium, formamidinium or both types of organic A ions [94], although there is also recent interest in all-inorganic perovskites using caesium as the A ion [175]. Methylammonium (MA) gives rise to bandgaps of around 1.55 eV, whereas formamidynium (FA) gives rise to bandgaps around 1.45 eV [141], closer to the maximum efficiency bandgap around 1.3-1.4 eV given by the Shockley-Queisser limit [134]. FAPbI is less thermodynamically stable, though, and harder to make, since it has a non-perovskite yellow δ-phase formed under much the same conditions as the perovskite. Ensuring a pure perovskite phase in the FAPbI is most easily mediated by including some MAPbI [68], or infilling the FAPbI into an existing MAPbI framework [174].

One of the advantages of perovskites is that the crystal structure is able to incorporate many elemental variations, and incorporating various dopants may improve device stability or performance [152]. We require the radii of the different elements involved to give a tolerance factor t of around one, where

$$t = \frac{r_A + r_x}{\sqrt{2}(r_B + r_x)}. \tag{2.1}$$

If this significantly varies from one, alternative structures become energetically favourable, such as the hexagonal phase at $t > 1$, or the orthorhombic phase for $t < 1$ [69]. However, for instance, bromide and iodide are both stable in methylammonium-lead structures at room temperature, as are mixtures of the two. Research has also highlighted the applicability of these mixed perovskites for LEDs, where, by substituting in different amounts of bromide instead of the iodide, the bandgap can be tuned, both in the optical [156] and infrared regions [85].

Another attractive feature of perovskites is their mobilities, which can exceed 100 cm^2/s [150, 37] for single-crystal samples, very high for a solution-processed material although not high for inorganics [28]. This is in large part because single-crystals have fewer trap states than polycrystaline samples, by around 2-3 orders of magnitude. The differences between electron and hole mobilities are small, with these measurements indicating that electrons have smaller mobilities. There is significant disagreement on this later part for multicrystal films [53], and many different processing techniques values orders of magnitude apart [63],

although the electron and hole diffusion constants are within an order of magnitude of each other within a given manufacturing and measuring system.

Methylammonium perovskites also have low degrees of recombination from defects, which create either no trap states or only shallow ones [77, 170]. This is due to having a bandgap between different sets electron orbitals, rather than a gap between bonding and antibonding orbitals. Density functional theory calculations for MAPbI show that the unoccupied orbitals are based on Pb *p*-orbitals, whereas the occupied orbitals are derived from I *p*-orbitals. Intrinsic defects with low formation energy tend to result in the insertion of energy levels between and around the normal bonding and antibonding energy levels. In the case of most semiconductors, such as gallium arsenide, this means deep traps within the bandgap [173], however in MAPbI these will be near the band edge, and therefore will not efficiently mediate recombination. Escape from these traps may be thermally mediated, however they could be responsible for variation in the mobilities measured. It is also experimentally found that the system is very tolerant to many types of extrinsic defects, which can occur at levels of several parts per million without significantly affecting performance [79, 125], and indeed allowing for doping of the system. This defect tolerance is particularly useful as solution-processing techniques typically produce high defect densities, which are limiting factors for organic solar cell performance.

Perovskites also have low rates of bimolecular recombination, due to a subtle offset in the *k*-space position of the valence and conduction band energy extrema. The optical absorption onset is still quite sharp, as excitation can occur at the nearby direct bandgap, but carriers are swiftly thermalised to states separated by an indirect bandgap with a lower probability of recombining [50, 7]. This *k*-space split results from a phenomenon called the Rashba effect, where spin degeneracy is broken by strong spin-orbit coupling (from the heavy elements) and the asymmetry of the crystal under inversion. This shifts the energy minimum of the conduction band in momentum space [172], causing a small momentum gap between the electron and hole energy minima. Recombination between these states therefore requires a phonon to conserve momentum, so happens at a reduced rate. This is implicitly helpful for the performance metrics of the perovskites, however does also mean that the absorption is not as strong as it should be, necessitating a thicker layer, and also requiring us to have lower nonradiative recombination. As will be discussed in section 2.5, the ratio of radiative recombination to incoming light gives us a photoluminescence quantum efficiency or PLQE, which is a performance metric indicating a higher output voltage. Research to passivate nonradiative recombination is therefore essential to improve efficiency [34], and structural alterations to the cell which improve outcoupling of luminescence is also important to consider [130].

Historically, perovskites have suffered from large degrees of hysteresis and time-dependent variation in their current-voltage curve, which both punishes long-term performance and complicates device characterisation [148]. There are several rival explanations of why this occurs. Firstly, it is known that perovskites have defect sites that are mobile at room temperature [43], which can move to counteract the internal electric field [118]. A second suggestion is trap filling [143, 88], and by filling in the traps, Shao et al. were able to remove all hysteresis from their system. However van Reenen et al. [159] claim that both ion migration and traps are needed to find the experienced hysteresis. While the controversy over the source of hysteresis is unsolved, the practical importance of it is limited now that we have established procedures that both reduce the hysteresis and improve solar cell performances.

An ongoing unfortunate aspect of perovskite solar cells is that the most efficient ones still contain soluble lead. There has been some success in replacing the lead with tin, however this results in breakdown products like SnI_2, which can have similar toxic effects to the lead [8], and efficiencies and stabilities remain unimpressive. There have been many attempts at 'double perovskites', where two unit cells are combined with one fewer B group than might be expected, resulting in the formula $A_3B_2X_9$, for instance $Cs_3Sb_2I_9$ [74]. This opens wide a large armory of elements, allowing us to construct all-inorganic cells with neither tin nor lead. Others have focused on the defect-tolerant aspect of perovskites and searched for other materials with similar bandstructures, irrespective of their crystal structures [16]. However, so far none of the cells found in this way have produced comparable efficiencies to lead halides [54].

Another problem is that perovskite cells typically have short lifetimes [90], often losing a significant proportion of their efficiency after a month. This is caused by the sensitivity of the cell to moisture and a tendency to thermally degrade at moderate temperatures, as well as reacting with electrodes or with the sealants in the same way as many solar cells. This all degrades the crystal quality and therefore creates traps and recombination pathways. There are a range of solutions being investigated, such as better encapsulation to prevent outgassing or incoming water, or replacing the electrodes with substances less liable to react with the perovskite, to improve this [5]. There have also been attempts to modify the active layer. The use of formamidinium helps this, provided it is not in the yellow δ phase [174]. There are other routes such as doping with caesium, which has little effect on the optical properties of the layer but improves the stability of the devices [169].

In spite of all these challenges, there are already attempts at commericalisation of perovskite solar cells, for various applications where the lead content and lifetime are not limiting factors. Primarily the applications are for perovskite-silicon tandem cells, which takes advantage of the slight increase in efficiency at low processing cost, adding a perovskite

layer to an already cheaply-manufactured silicon solar cell. This is considered the easy entry to the market, given the existing lead in photonic management, engineering and chemistry that silicon cells enjoy [142].

2.3 Drift-diffusion models

2.3.1 Fundamental derivation

In this work we will make extensive use of the drift-diffusion equations, sometimes referred to as the Shockley equations, so it is worth outlining their derivation in full. There are two main ways to derive these equations, and we will briefly explore both. We will assume an isotropic medium for simplicity in both cases.

The first derivation, found in [136], involves combining the continuity equation for both carriers with the Poisson equation and the separate expressions for drift and diffusion current. With $J_{n(p)}$ the current due to electrons (holes), the continuity equations for the two carriers are

$$q\frac{dn}{dt} = \nabla J_n + q(G-R) \tag{2.2}$$

$$q\frac{dp}{dt} = -\nabla J_p + q(G-R), \tag{2.3}$$

where G and R are the generation and recombination rates of carriers and q is the magnitude of the electron charge. These rates can in principle differ for the two carrier types but are identical in any process that conserves charge; charge injection is possible but will be considered as a boundary condition. One might, however, add charge trapping/detrapping to either species, which would appear in these terms.

Fick's law of diffusion [120] gives the flux rate, J_ψ, of a substance at concentration ψ due to diffusion as $J_\psi = -D_\psi \nabla \psi$, for D_ψ the diffusion constant. The current flux will then be the product of this and the carrier charge. The definition of mobility, $\mu = \frac{|v_d|}{E}$ for the drift velocity v_d and electric field E, gives us the drift current. Collectively these give

$$J_n = qD_n \nabla n + q\mu_n n\mathbf{E} \tag{2.4}$$

$$J_p = -qD_p \nabla p + q\mu_p p\mathbf{E}\,. \tag{2.5}$$

Finally we add to this the Poisson equation to determine the electric field from the carrier concentrations:

$$\varepsilon \nabla \cdot \mathbf{E} = q\,(p - n + N_d)\,, \tag{2.6}$$

where ε is the (homogeneous) permittivity of the medium and N_d the concentration of any dopants, impurities or trapped carriers, weighted by their relative charges.

While simple, this derivation gives no particular insight into the possible failures of the model. The conservation laws hold precisely, and Poisson's equation is a good approximation in our system, however equations 2.4-2.5 have more circumstantial validity. Therefore a more complete derivation from Boltzmann transport theory will also be illustrated. The Boltzmann equation, derived from the Liouville theorem in classical statistical physics, governs the evolution of the distribution function, $f(\mathbf{r},\mathbf{k})$, the density of carriers in phase-space (the $\mathbf{k}$ vector relates to momentum as $\mathbf{p} = \hbar\mathbf{k}$) [162]. Within a relaxation-time approximation [161], where f is close to the equilibrium value f_0, the equation for each carrier is (in one dimension)

$$v\frac{\partial f}{\partial x} + \frac{q_s E(x)}{\hbar}\frac{\partial f}{\partial k} = -\frac{f - f_0}{\tau_m}, \tag{2.7}$$

where v is the velocity, $q_s = \pm q$ with the negative sign for electrons and positive for holes, and τ_m the relaxation time. In this formulation, we define a current density contribution as

$$J(x) = q_s \int v(k) f(k,x) \frac{dk}{\pi},$$

therefore using an expression for f from equation 2.7,

$$J(x) = q_s \int_{-\infty}^{\infty} \frac{dk}{\pi} v(k) \left(f_0 - \tau_m v(k) \frac{\partial f}{\partial x} - \frac{q_s \tau_m E(x)}{\hbar} \frac{\partial f}{\partial k} \right). \tag{2.8}$$

f_0 is symmetric in v, so we can eliminate the first term, and as we have assumed τ_m is constant, we can move the partial derivative in the second term. This gives us

$$J(x) = -q_s \tau_m \frac{\partial}{\partial x} \int_{-\infty}^{\infty} \frac{dk}{\pi} v^2(k) f - \frac{q_s^2 \tau_m E(x)}{\hbar} \int_{f(x,-\infty)}^{f(x,\infty)} \frac{df}{\pi} v. \tag{2.9}$$

If we may assume parabolic bands, so that $v = \hbar k/m$, this simplifies. The first integral is the concentration-weighted mean squared velocity of the system. In thermal equilibrium, this is $k_B T/m$ for each dimension. We define the concentration as $\phi = \int \frac{dk}{\pi} f(k,x)$. The second may be integrated by parts – the distribution function must rapidly tend to zero for large k so the constant term is zero. The v integral may then be viewed as an integral over k, producing

$$J(x) = -q_s \tau_m \frac{\partial}{\partial x} \left(\psi(x) \frac{k_B T}{m} \right) + \frac{q_s^2 \tau_m E(x)}{\hbar} \frac{\hbar \psi(x)}{m}. \tag{2.10}$$

Identifying $\mu = q\tau_m/m$ from Drude theory for ballistic carrier transport [6], and using the Einstein relation $D = k_B T\mu/q$ (assuming T is constant), we find

$$J(x) = -q_s \frac{\partial \psi(x)}{\partial x} D + \mu q E(x)\psi(x). \tag{2.11}$$

This result is identical to those in equations 2.4-2.5, however we are aware of the limits on its validity: the relaxation-time approximation, the parabolic band approximation, Drude theory, the Einstein relation, a global temperature and the near-equilibrium nature of the velocity distribution. Other than Drude theory and the parabolic band approximation, these assumptions are usually good for small electric fields and low excitations. Drude theory is questionable for systems where electrons and holes are strongly localised, such as organic semiconductors, and these systems may also have nonparabolic bands, or interplay between band states and trap states. In many cases, the validity of the approximations can be improved if nonconstant diffusion constants and mobilities (varying with electric field or carrier density) are introduced [161].

2.3.2 Reformulation

Quasi-Fermi levels

The drift-diffusion equations may be reformulated in terms of several different sets of variables. Combining equations 2.2, 2.3, 2.4, 2.5, and 2.6, and using $\mathbf{E} = -\nabla\phi$ we have the 'natural variable formulation' in terms of n, p, ϕ. These are the coupled equations

$$\frac{\partial n}{\partial t} = \nabla \cdot (D_n \nabla n + \mu_n n \nabla \phi) + G - R \tag{2.12}$$

$$\frac{\partial p}{\partial t} = \nabla \cdot (D_p \nabla p - \mu_p p \nabla \phi) + G - R \tag{2.13}$$

$$\nabla \cdot (\varepsilon \nabla \phi) = -q(p - n + N_d). \tag{2.14}$$

We may formulate the carrier concentrations in terms of quasi-Fermi levels. Quasi-Fermi levels describe carrier populations that have reached thermal equilibrium with themselves, but electrons and holes have not reached thermal equilibrium with each other and have separate Fermi levels. Under continuous excitation, the steady state retains this non-equilibrium, so this is usually the scenario of interest. If the system is non-degenerate, we may use a simple expression for the carrier concentrations in terms of the local quasi-Fermi potentials, ϕ_n and ϕ_p for electrons and holes respectively. With the local energy level of the conduction

(valence) band as $E_{c(v)}$, and their effective densities of states as $N_{c(v)}$ we have

$$n = N_c \exp\left(\frac{E_c - q\phi_n}{k_B T}\right),\ N_c = 2\left(\frac{m_c k_B T}{2\pi\hbar^2}\right)^{3/2}, \tag{2.15}$$

$$p = N_v \exp\left(\frac{q\phi_p - E_v}{k_B T}\right),\ N_v = 2\left(\frac{m_v k_B T}{2\pi\hbar^2}\right)^{3/2}, \tag{2.16}$$

for $m_{c(v)}$ the effective mass of the carriers in that band. Their product, in equilibrium when $\phi_N = \phi_p$, is

$$np = n_i^2 = N_c N_v e^{-E_g/k_B T}, \tag{2.17}$$

This is the law of mass action [6], and defines the intrinsic carrier concentration n_i [114].

In the limit of no doping, in thermal equilibrium charge neutrality requires $n = p = n_i$. If we are not in the thermal equilibrium but are nondegenerate enough for Boltzmann statistics for both carrier types, we have instead

$$n = n_i \exp\left(q\frac{\phi - \phi_n}{k_B T}\right), \tag{2.18}$$

$$p = n_i \exp\left(q\frac{\phi_p - \phi}{k_B T}\right), \tag{2.19}$$

provided we set the absolute level of ϕ to be 0 when the system is in equilibrium with no net charge. This is required for the Fermi level to be in the middle of the bandgap so the system has no net charge. If the system is doped, an offset is required. This relation enables the quasi-Fermi level formulation of the drift-diffusion equations. The convenience of this formulation is that, if we make the assumption that the Einstein relationship is valid, we can write

$$J_n = qD_n\nabla n + q\mu_n n\mathbf{E} = q\left(\frac{D_n qn}{k_B T}(\nabla\phi - \nabla\phi_n) - \mu_n n\nabla\phi\right) = -q\mu_n n\nabla\phi_n \tag{2.20}$$

$$J_p = -qD_p\nabla p + q\mu_p p\mathbf{E} = q\left(-\frac{D_p qp}{k_B T}(-\nabla\phi + \nabla\phi_p) - \mu_p p\nabla\phi\right) = -q\mu_p p\nabla\phi_p \tag{2.21}$$

Slotboom variables

The relationships in equations 2.20-2.21 are concise, but not as convenient as might be imagined, as n and p are no longer the primary variables of this set of equations (although they are readily calculable in terms of the quasi-Fermi levels). So, although these equations are a workable and often favoured as the means to solve the drift diffusion equations in steady-state [161], there is another formulation that is slightly more mathematically elegant,

known as the Slotboom variables [29, 112]. This is governed by the variables ρ_n, ρ_p, defined by

$$n = \rho_n e^{\varphi} \tag{2.22}$$

$$p = \rho_p e^{-\varphi}, \tag{2.23}$$

where we have rescaled the electric potential using $\varphi \equiv \phi / V_T$, for $V_T \equiv k_B T / q$, the thermal voltage. Unlike equations 2.18 and 2.19, equations 2.23 and 2.23 are valid for lightly-doped systems too, although extension to degenerate conditions is more challenging. We can then express the currents as

$$J_n = -qD_n e^{\phi} \nabla \rho_n \tag{2.24}$$

$$J_p = qD_p e^{-\phi} \nabla \rho_p. \tag{2.25}$$

In the time-independent case, we can then set the equations up as a matrix

$$-\nabla \cdot \begin{pmatrix} D_n e^{\varphi} \nabla \rho_n \\ D_p e^{-\varphi} \nabla \rho_p \\ \varepsilon \nabla \varphi \end{pmatrix} = \begin{pmatrix} G - R \\ G - R \\ q^2 (p - n + N_d)/k_B T \end{pmatrix}, \tag{2.26}$$

where the left hand side contains all the flux terms in terms of the Slotboom variables, and the right-hand side all the source terms (which require the carrier concentrations).

The physical dimensions of the problem are rescaled by a lengthscale λ, so $\nabla \to \frac{\nabla}{\lambda}$, and $G, R, \rho \to \frac{G,R,\rho}{\lambda^3}$. This gives us

$$-\nabla \begin{pmatrix} D_n e^{\varphi} \nabla \rho_n \\ D_p e^{-\varphi} \nabla \rho_p \\ \varepsilon \nabla \varphi \end{pmatrix} = \begin{pmatrix} (G - R)\lambda^2 \\ (G - R)\lambda^2 \\ q^2 (p - n + N_d)/k_B T \lambda \end{pmatrix}. \tag{2.27}$$

The time-dependent form of these equations is not as convenient, as the full solution requires the extra terms

$$\frac{\partial n}{\partial t} = e^{\varphi} \left(\frac{\partial \rho_n}{\partial t} + \rho_n \frac{\partial \varphi}{\partial t} \right), \qquad \frac{\partial p}{\partial t} = e^{-\varphi} \left(\frac{\partial \rho_p}{\partial t} - \rho_p \frac{\partial \varphi}{\partial t} \right) \tag{2.28}$$

added to the left of the first two lines of both equations 2.27 and 2.26.

2.3.3 Recombination

Shockley-Read-Hall

There are several potential sources of recombination in solar cells. In most systems, recombination at low excitation levels arises primarily from defect or trap states [114]. This is called 'Shockley-Read-Hall recombination', as it was proposed roughly simultaneously by Shockley and Read [146] and Hall [61]. It is often simply referred to as 'monomolecular recombination', as it is first-order in minority carrier concentration when one carrier type predominates. In general systems, the net rate of recombination is

$$R_{SRH} = \frac{np - n_i^2}{\tau_p(p + p_t) + \tau_n(n + n_t)}, \tag{2.29}$$

where n_t (p_t) is the density of electrons (holes) in filled traps and τ_n (τ_p) is the time for electrons (holes) to be captured by trap states. Note that although n_t only explicitly occurs in the denominator, τ_n increases with trap density, so more traps will make recombination more common. We can explicitly write n_t as the product of the density of traps and a capture cross-section, $t_n = n_t B_n$. Note also that equation 2.29 still conserves charge, as one electron and one hole are absorbed, and is not strictly monomolecular (i.e. first-order in any carrier concentration) when the carrier densities are roughly equal. Monomolecularity emerges when, say, $\tau_p \sim \tau_n$ and $p \gg n \geqslant n_i$, so we can approximate equation 2.29 to $R_{SRH} = n./\tau_n$. It also emerges if $n = p \gg n_i, p_t, n_t$, when $R_{SRH} = n/(\tau_n + \tau_p)$.

SRH recombination can be either luminescent or non-luminescent [124], but is typically non-luminescent. The degree of SRH is always dependent on the material parameter and so is regarded as an 'avoidable' form of recombination [114].

Surface and grain boundary recombination

Surfaces and grain boundaries represent regions where there are likely to be a large concentration of trap states, due to broken bonds and higher concentrations of impurities. Because the traps are concentrated in a small space, it is more useful to consider the density per unit area than per unit length [114]. We can define the surface recombination velocities, $S_{n,p}$, by multiplying the density of traps per unit area, N_t with the capture cross-section, B_n as before. The recombination times, $\tau_{n,p}$ are equal to the product of the thickness of the layer (Δx) and $S_{n,p}$. The recombination per unit area is therefore

$$R_{Surf}\Delta x = \frac{np - n_i^2}{(p + p_t)/S_n + (n + n_t)/S_p}. \tag{2.30}$$

In the limit of electrons being scarce and holes plentiful, $R_{Surf}\Delta x = S_n(n - n_0)$. The result for holes being rare is similar.

Band-to-band recombination and van Roosbroeck-Shockley relations

Band-to-band recombination involves the recombination of an electron and hole without an intermediate stage, and therefore is bimolecular in the low-doping case. Balancing with band-to-band generation in equilibrium, we have the net rate of recombination as $R_{bb} = B(np - n_i^2)$ for B the bimolecular recombination constant [161]. In direct-bandgap semiconductors, this process is optically generated, otherwise it may also involve phonon absorption or emission.

These transitions are the inverse of the optical generation of carriers. This has two consequences: we expect light to be generated by this type of recombination, and we can in principle calculate thermodynamically the expected B coefficient. In practice, there may be recombination that has a similar carrier-dependence rate ($\sim np$) but not arising from optical transitions, therefore the B coefficient measured from recombination may be higher than the optical emission B coefficient.

The van Roosbroeck-Shockley relation relates the generation of carriers by the black-body spectrum to the recombination rate, which must generate the same distribution of carriers [160]. In thermal equilibrium, using the Boltzmann approximation for the distribution of light (without the $+1$ term in the denominator when $E \gg k_B T$)

$$Bn_i^2 = \int_0^\infty \frac{8\pi n_s^2}{c^2} \frac{\alpha \nu^2 d\nu}{\exp(h\nu/k_B T)}, \tag{2.31}$$

for α and n_s the absorption coefficient and refractive index of the medium, both functions of wavelength and material condition, and ν the frequency of light. In practice, this is a difficult relation to apply due to the strong dependency on n_i, which is usually only known approximately, and the B coefficient is much more easily measured spectroscopically, as discussed below. Because of this fundamental link between B and α, this recombination is usually regarded as 'unavoidable' – primarily dependent on the fundamental material, not on impurities or fabrication methods. Our desire for complete absorption of the solar spectrum means we either need to have a large B or a very thick film, as in the case of silicon solar cells, where an indirect bandgap results in suppression of the absorption and emission [114]. This suppression is due to the requirement that a phonon is created or destroyed in the absorption process to conserve momentum. As the recombination converts the energy into light which can be re-absorbed (see section 2.5), not all of this recombination is necessarily wasteful.

The same van Roosbroeck-Shockley relation without the integral also relates the absorption and emission spectrum, meaning that we expect the emission of light to be proportional to the absorption. This is called the Kubo-Martin-Schwinger or Kennard-Stepanov relation, [14, 67] and is often presented as

$$PL(\nu)d\nu \propto \alpha(\nu)\nu^2 d\nu \exp\left(-h\nu/k_B T\right). \tag{2.32}$$

An important caveat must be made for using formulae 2.31 and 2.32. While these thermodynamic relations hold for the correct, state-dependent definition of α, for the more usual and more useful definition of α these relations only hold for excitations of states in complete thermal equilibrium simultaneously linked only to each other. The more useful definition of α is the absorption cross-section for an empty upper band and a full lower band, whereas the equations given relate instantaneous absorption and emission coefficients for a fixed carrier distribution [14].

Auger recombination and impact ionisation

Auger recombination occurs when two similar carriers collide and one is excited while the other recombines with a carrier of the opposite type. The excited carrier will soon thermalise, so the energy transfer is not useful. Impact ionisation is the inverse process, whereby a carrier is excited by two carriers colliding [161]

Auger recombination is mostly relevant when carrier concentrations are very high, due to requiring three carriers. It can also be relevant if we have little other recombination, such as in indirect bandgap materials with very low impurity levels, like in very pure silicon [114]. As it does not involve an optical transition, Auger recombination is not suppressed by indirect bandgaps. It occurs at a net rate of

$$R_a = C_n\left(pn^2 - n_0^2 p_0\right) + C_p\left(p^2 n - n_0 p_0^2\right), \tag{2.33}$$

where C_n, C_p are constants of the material.

Impact ionisation, as a net generation process, only requires two carriers, however requires a large amount of excess energy. It is strongly dependent on having large electric fields present in the material, and so will not be relevant to the systems investigated in this study [161].

2.3.4 Boundary conditions

As with most differential equations, the solutions of the drift-diffusion equations require boundary conditions to be specified. Solar cells in particular will not generate energy unless there is either a spatial inhomogeneity in the system or different boundary conditions at the two different electrodes. Usually boundary conditions of interest are either semiconductor-insulator, semiconductor-semiconductor or semiconductor-metal.

Semiconductor-insulator junctions

At a junction between a semiconductor and an insulator too thick to tunnel through, our boundary conditions are limits on the current perpendicular to this edge, as they have nowhere to go. There can be trap states at the boundary, where recombination must be matched by incident current. We therefore specify $-\mathbf{j_n} \cdot \hat{\mathbf{n}} = \mathbf{j_p} \cdot \hat{\mathbf{n}} = qR_{Surf}(n,p)\Delta x$, where $\hat{\mathbf{n}}$ is the vector orthogonal to the insulator surface. If the insulator also represents the end of the system of interest, we must also set the perpendicular component of the electric field to zero to isolate our system from the surroundings. This condition arises from the overall electrical neutrality of our system [163]. Since this means any current has to be diffusive, all these boundary conditions are Neumann boundary conditions on the natural variables, boundary conditions that fix the derivatives of components perpendicular to a boundary interface.

In the quasi-Fermi level formulation, these can be written in the form $\nabla\phi \cdot \hat{\mathbf{n}} = 0,\ n\nabla\phi_n \cdot \hat{\mathbf{n}} = p\nabla\phi_p \cdot \hat{\mathbf{n}} = R_{Surf}(n,p)\Delta x$. This would be considered 'generalised Neumman conditions', as there are prefactors to our derivative terms. Similarly in Slotboom format, we append $e^{\pm\varphi}\nabla\rho_{n(p)} \cdot \hat{\mathbf{n}} = R_{Surf}(n,p)\Delta x$ to the condition on the potential.

Semiconductor-conductor junctions

At metal-semiconductor junctions, the potential is externally fixed. Typically, these junctions are at the electrodes. Band-bending is required to match the nonexcited Fermi levels of the materials, which creates an energy barrier for one carrier type but not the other, known as a Schottky barrier. An example is depicted in figure 2.3, although we must usually consider the impact of both electrodes simultaneously.

In the quasi-Fermi and Slotboom formulations as described above, making the system electrically neutral requires setting the average of the two electrode potentials to zero. The built-in potential, V_{bi}, is the potential difference over the system that exists when no external voltage is imposed across the system, when the system is in equilibrium. In our work it is brought about by differences between the work function (the energy difference between Fermi level and vacuum) of the different electrodes or electron/hole blocking layers, although

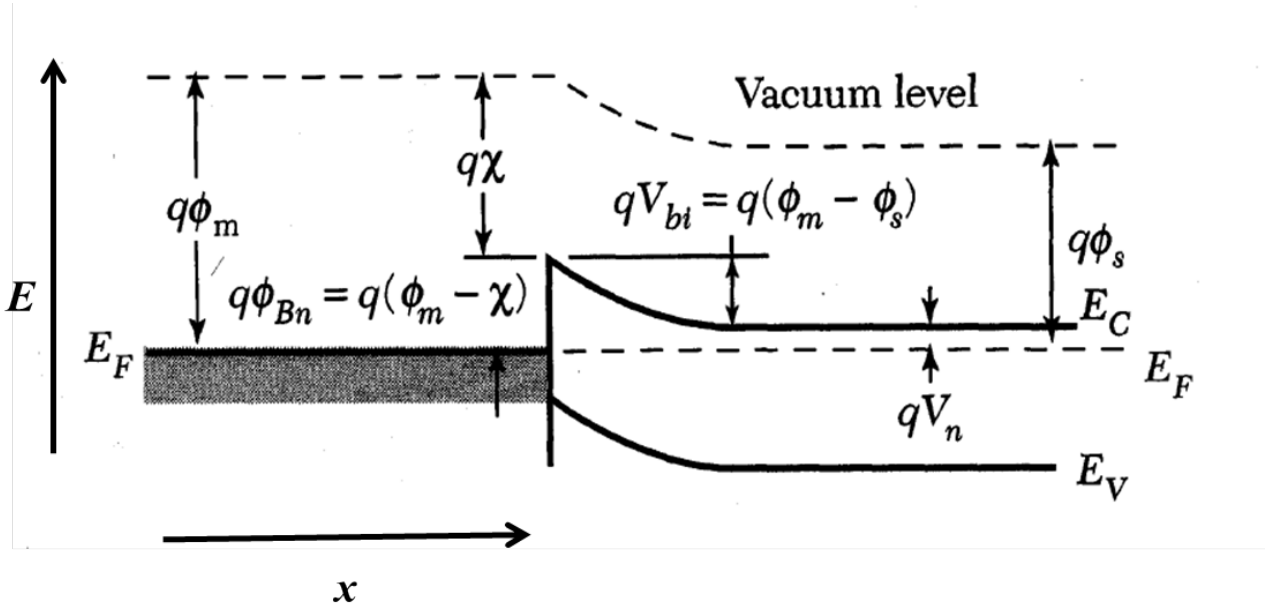

Fig. 2.3 Energy diagram of a Schottky barrier, a metal-semiconductor interface. The work functions of the metal and semiconductor are ϕ_m and ϕ_s, respectively. χ is the electron affinity of the semiconductor. The electron affinity of the semiconductor does not depend on the applied field, but the work function does. This results in a fixed barrier height of ϕ_{Bn} for electrons coming from the metal side but a variable barrier of V_{bi} for electrons coming from the semiconductor. Holes, by contrast, have no energy barrier either way. Figure modified from [154], and assumes all band-bending occurs at one electrode, as in figure 2.4b and d.

inhomogeneity of the band gap, density of states or electron affinity of the semiconductor can also give effective or actual built-in fields [114]. In an ideal case, V_{bi} is simply the difference between the electron affinities of the electrodes, however in practice, energy-level pinning at the interface may reduce this. V_{bi} corresponds to a bending of the energy bands, as shown in figure 2.4, but not to a change in Fermi level, hence it does not give any current unless there are non-equilibrium levels of carriers. The applied voltage difference bends both the energy bands and the Fermi levels.

In equilibrium, the Fermi energies of all the layers must be equal. If the work function (defined to be positive) of a semiconductor is smaller than the metal next to it, electrons are removed from the semiconductor (and/or holes injected) to establish an electrostatic potential of V_{bi} that equalises the layers, as shown in figure 2.3. It imposes an energy barrier to carrier extraction and injection for electrons, but not for holes. However, if a potential is applied across the barrier, the Fermi level of the semiconductor is moved and the effective V_{bi} is changed. Raising the semiconductor Fermi level allows carriers to leave the semiconductor more easily, exponentially increasing the current out. However lowering the Fermi level does not reduce the energy barrier of the metal, hence the injection current is less adjustable. This results in rectification of the electron current; in addition, the electron current is expected to be very low except at high voltages, due to the energy barrier. Holes, however, have no energy barrier either way, although typically will have low concentration due to the distance between the Fermi energy and the valence band, hence we have a low electrically generated hole current [154]. However, when the system is photoexcited, this consideration is irrelevant and holes are easily conducted out of the system but electrons are mostly trapped. The boundary condition in either case is 'Ohmic' – the hole concentration at the interface is pinned to the level expected by the Fermi distribution [114]. Alternatively, the current may be given by a (large) extraction velocity, $v_{r,p}$, times the difference between the carrier concentration at the interface and the thermal equilibrium value [30], $|J_p| = qv_{r,p}(p|_{interface} - p_0)$. The electron current may either be set to zero [129] or, for more precise calculations, set equal to the interface recombination (as for the insulator) plus the dark current from any voltage dropped over the Schottky barrier. If we have no interface recombination, then this can be given by a similar expression to the hole condition, with a smaller recombination velocity for selective contacts: $|J_p| = qv_{r,n}(n|_{interface} - n_0)$.

If the Fermi level of the semiconductor is larger than that of the metal (i.e. further from vacuum energy, the opposite to the case depicted in figure 2.3), we have the opposite direction of band bending, as seen in figure 2.4b and d, and all the above statements have electron and hole interchanged. In practical devices, we often use a highly-doped semiconducting blocking layer between the metal electrode and the active layer. This allows finer-scale

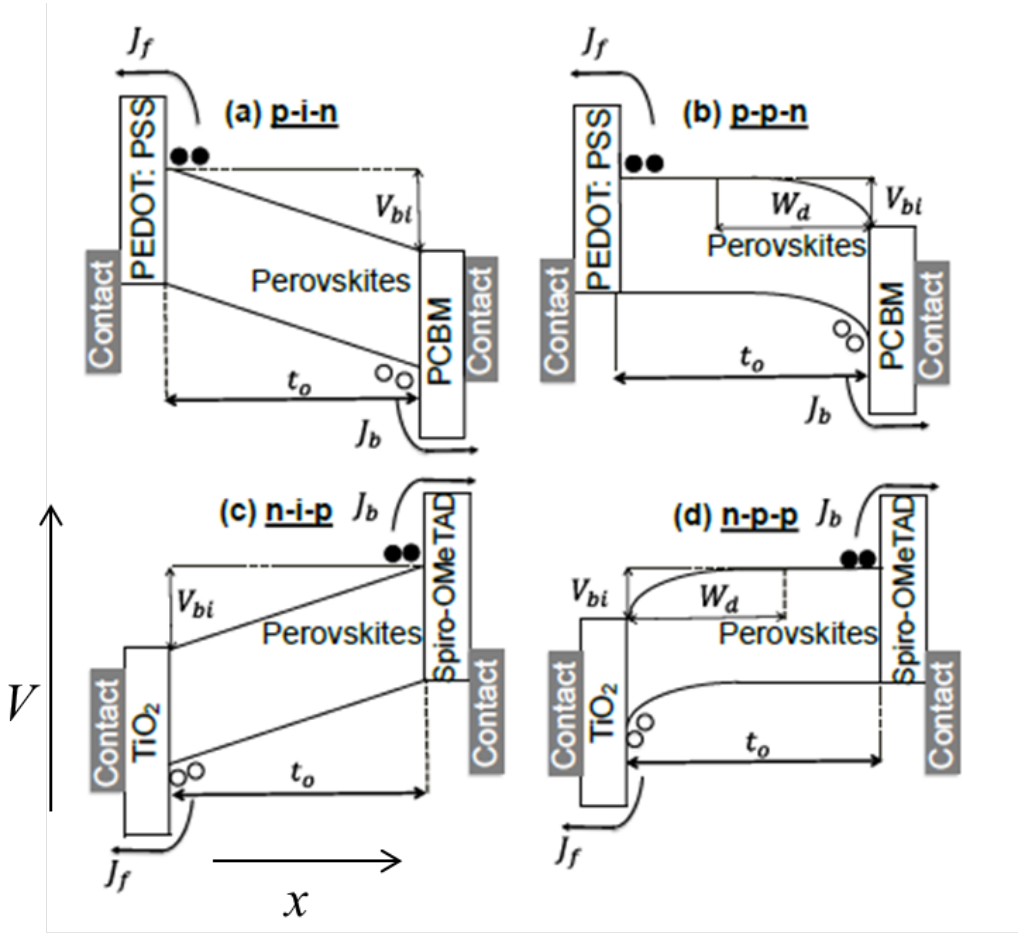

Fig. 2.4 Examples of band-bending and built-in voltage for different perovskite solar cells. The different cell configurations are: (a,b): PEDOT:PSS as the electron-blocking layer, PCBM as a hole-blocking layer. Light enters from the left, and these cells are referred to as 'traditional', as holes are extracted from the front; (c,d): Spiro-OMeTAD as the electron-blocking layer, Ti_2 as the hole-blocking layer. These are referred to as 'inverted' devices, as holes are extracted from the rear. It is generally argued that good perovskite cells are intrinsic (i), having a low carrier density unless illuminated, however some are p-doped (p), which marks the difference between (a,c), p-i-n cells, and (b,d), p-p-n. In intrinsic devices, there is a uniform field across the device, whereas in p-type devices all the voltage is dropped in a 'depletion region' of width W_d next to the hole-blocking layer, where the concentration of holes is much lower than expected. J_f and J_b represent front and back contact minority carrier extraction that will decrease the overall extracted current. t_0 is the thickness of the cell. Diagram reproduced from [151], with alteration.

control of the energy levels involved and fewer interface trap states. It also results in the same band-bending as the Schottky junction, but some of the bending now occurs in the blocking layer, as unlike the metal, its resistivity is appreciable. This means we can impose a larger barrier to the blocked material without the Fermi level getting too close to the band edge at any point [114], and also allows us to prevent there being any energy states for the blocked carrier to tunnel into. The boundary conditions to impose will largely be the same.

2.4 Numerical solution techniques

So far, we have stated what the equations to be solved are, but not thought about the method of solving them. While there are simplified cases and where analytic solutions are available, e.g. the Hovel model [98, 151, 99], for the most part these coupled partial-differential equations (PDEs) are not analytically solvable. There are two main computational approaches to numerically solving these PDEs: finite difference (FD) and finite element (FE). In both cases, the domain of the solution must be finite, and is broken down into subsections or subdomains. In one dimension, each of these are just lengths, but in higher dimensions there is more freedom to choose the nature of the subdomains, with some choosing squares/cubes and others choosing triangles/tetrahedrons.

2.4.1 Finite element analysis

FE analysis involves approximating the solution to the PDE on each subdomain using a set of polynomial basis functions. The boundary conditions on each section must be upheld by the basis functions – where subdomains contact other subdomains, the solution must be continuous, otherwise it must match the external boundary conditions. The solution to the PDE can then be specified as a linear combination of the basis functions on each element, and the relationships between the basis functions from all boundary conditions and the PDE can be assembled into a single matrix equation. This equation is then solved [153]. This approach can easily include complex boundary conditions, including both unusual (but polygonal) shapes and boundary conditions related to derivatives, which are directly incoroporated into the solution [23].

There are many other technical details to FE code, and writing an FE analysis program is not within the scope of this PhD. However, a ready-made FE MATLAB toolkit was used to solve several sets of 2D PDEs. This toolkit solves up to second-order (in time and space) coupled PDEs, with a number of dimensions N_{dim} =2 or 3. It requires that the equations can

be written in the form

$$\mathbf{m}\frac{\partial^2 \mathbf{u}}{\partial t^2} + \mathbf{s}\frac{\partial \mathbf{u}}{\partial t} - \nabla \cdot (\mathbf{c} \otimes \nabla \mathbf{u}) = \mathbf{f}, \tag{2.34}$$

where $\mathbf{m}$, $\mathbf{s}$, $\mathbf{f}$ can be any vector function of the local components of the solution vector, $\mathbf{u}$. All these are 'component vectors' with length equal to the number of components of the solution, $N_{comp} = 3$ in our case, (n, p and φ), not the number of dimensions – they are all scalar-valued functions in physical space. $\mathbf{c}$ is a 4-dimensional tensor function, and $\mathbf{c} \otimes \nabla \mathbf{u}$ represents a tensor operation that takes the matrix $\nabla \mathbf{u}$, of size ($N_{dim} \times N_{comp}$), and returns another matrix of the same size, linearly dependent on its values. $\mathbf{c}$ can therefore be thought of as an $N_{comp} \times N_{comp}$ matrix of $N_{dim} \times N_{dim}$ matrices [104]. In our 2D cases, there is no need for mixed derivatives, so no off-diagonal terms in the 2×2 matrices and the on-diagonal terms are identical within each matrix of these component matrices. In the Slotboom formulation, those on-diagonal values will be $D_n e^{\varphi}$, $D_p e^{-\varphi}$ and ε, as can be seen in equation 2.26.

A relevant feature of this toolkit is that nonlinear equations need not be computationally challenging for it, however it is not well-formulated to damp out instabilities, which often result from the coupled equations we are using, particularly when high potential differences exist. Another feature that affects its applicability is how the meshing tends to give long-range isotropy but does not allow for different dimensions to be resolved with different degrees of detail.

The subdomains in our 2D system are given by a Delaunay triangulation [104]. This is a triangular tiling whose points are nodes with the defining property that no node is inside the circumcircle of any other triangle. The circumcircle of a triangle is the circle that passes through all three points. The circular symmetry of this arrangement, along with mathematical errors that arise for very acute angled triangles here, means that the generation program has a preference for triangles that are close to being equilateral, as can be seen in figure 2.5. The values of the solution are calculated at the nodes of the triangle, but the $\mathbf{f}$ value that gives the right-hand side of equation 2.34 (in our case, $G-R$) is calculated at the centers of each triangle, with the solution values here interpolated from the value at the three corners. This interpolation can result in problems if the solution changes rapidly across one triangle. The triangulation itself gives overall isotropy (unlike in systems with rectangular subdomains where there are preferred directions), however it also means it is not possible to have coarser graining in one direction than in another to mitigate this problem when the solution changes more rapidly in one direction than the other.

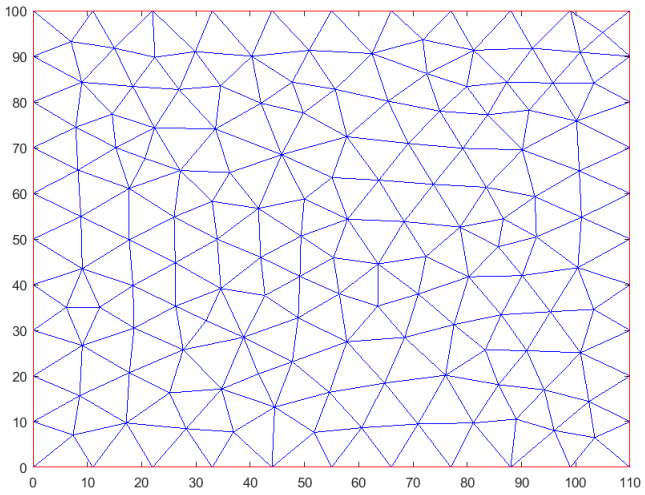

Fig. 2.5 An example of a rectangle that has been Delaunay triangulated by MATLAB.

2.4.2 Finite difference analysis

Finite difference analysis also involves representing the PDE on a grid but discretises the differential operators, so that the derivatives can be expressed in terms of nodal values of the variables. In this approach, using a rectangular or cuboid grid is easier than any irregular shape. This is not isotropic and imposes some directionality on the global problem but does make it easy to represent different dimensions with different degrees of finesse, by using different grid lengths δx, δy, etc.. We then express the derivatives using values on either side, for instance,

$$\left.\frac{\partial f}{\partial x}\right|_{x+\delta x/2} \approx \frac{f(x+\delta x)-f(x)}{\delta x}. \tag{2.35}$$

Other expressions for the derivative are possible, including higher-order corrections [91]. It is possible to evaluate the gradient on-point, using the two nodal points adjacent to the desired node, i.e.

$$\left.\frac{\partial f}{\partial x}\right|_{x} \approx \frac{f(x+\delta x)-f(x-\delta x)}{2\delta x}, \tag{2.36}$$

however this effective doubling of the value of δx is unncecessary for us, as we are usually interested in second order differential equations. Although the first-order derivatives are evaluated at the midpoints between cells, the second-order derivatives will be evaluated at the cell midpoints. In some cases, the whole system of equations can be written as a single matrix equation, in which case the time-independent solution can then be found by matrix division [161]. For time-dependent cases, the time-derivative is calculated and the solution is integrated forwards in time using a ready-made MATLAB script that chooses the timesteps

according to the 'stiffness' of the problem – how strongly nonlinear it is, and how errors will propagate. In our case, high degrees of stiffness results from the feedback between electric field and carrier concentration. This time integration method can also be used to solve time-independent problems, by integrating forwards an arbitrarily long time until the system reaches equilibrium. In many cases, these codes are much easier to write than FE code, and several have been made in the course of this PhD.

2.4.3 Scharfetter-Gummel discretisation

One problem with both approaches above is that a function must be calculated using interpolated values of the carrier concentrations. The most obvious assumption is that the concentration changes linearly between nodal values. However, if voltages change rapidly between cells, this can lead to instabilities. Qualitatively, this occurs when a subdomain with low carrier concentration has a large drift outflux into a subdomain with a high concentration. As only their average concentration is used, the outflux is not limited by the carrier concentration at the point of origin. Quantitatively, an instability may arise when the voltage difference between cells approaches $2k_BT/q$. The linear carrier concentration interpolation, however, is only valid in the zero-field or uniform carrier density limits, and a better interpolant is desired. A simple solution to this was proposed by Scharfetter and Gummel [138], who discretise the drift-diffusion equations in a different form. Their approximation was derived by assuming that both current and electric field (and consequently, mobilities) are constant between nodes, though discontinuous at the nodes. We can then solve equation (2.4) for $J_{n(p)}(M)$, the value between nodes N and $N+1$. In terms of the nodal values of $n(p)$, we then find

$$J_n(M) = qE(M)\mu_n(M)\left(\frac{n(N+1)}{1-\exp(-E(M)\Delta x/V_T)} + \frac{n(N)}{1-\exp(E(M)\Delta x/V_T)}\right) \quad (2.37)$$

$$J_p(M) = qE(M)\mu_p(M)\left(\frac{p(N)}{1-\exp(-E(M)\Delta x/V_T)} + \frac{p(N+1)}{1-\exp(E(M)\Delta x/V_T)}\right). \quad (2.38)$$

Although formally undefined when $E = 0$, equation 2.37 tends to the correct limit of $J_n = qD_n\left(n(N+1) - n(N)\right)/\Delta x$ after application of the Einstein relation. To give explicit solutions in this case, we may rewrite equations 2.37-2.38 using the Bernoulli function [33],

$\mathscr{B}(z)$:

$$\mathscr{B}(z) \equiv \begin{cases} \dfrac{z}{e^z - 1} & \text{for } z \neq 0 \\ 1 & \text{for } z = 0. \end{cases} \tag{2.39}$$

$$\Rightarrow \quad J_n(M) = qD(M)\frac{n_{N+1}\mathscr{B}(\varphi_{N+1} - \varphi_N) - n_N\mathscr{B}(\varphi_N - \varphi_{N+1})}{\Delta x} \tag{2.40}$$

$$J_p(M) = -qD(M)\frac{p_{N+1}\mathscr{B}(\varphi_N - \varphi_{N+1}) - p_N\mathscr{B}(\varphi_{N+1} - \varphi_N)}{\Delta x}. \tag{2.41}$$

Physically, this implies an exponential change in carrier density between nodes, and is a type of solving approach known as 'upwinding' because in the limit of large drift, the flux becomes primarily dependent on the carrier concentration in the upwind direction. While this approach is reliable when applied to grids in one, two or three dimensions, triangles that includes obtuse angles will result in spikes in the solution, and so applying this approach to triangular grids is complex [12].

2.5 Photon Recycling

Photon recycling occurs when optically generated charges recombine to generate another photon which is then also absorbed [39, 10]. We will investigate modelling this effect in microscopic detail elsewhere, but it is worth firstly outlining the physics of how this benefits the cell as a whole.

Thermodynamically, we may derive the counterintuitive conclusion that higher photoluminescence efficiency from the solar cell results in a higher efficiency. Qualitatively, this is because a cell's non-radiative recombination is not fundamentally necessary, but radiative recombination is thermodynamically unavoidable, so a lack of radiation arising from QE < 1 is a sign of unnecessary energy loss. We start by relating the outgoing light of an excited system with a potential difference of qV between energy levels to its radiation. This equation arises from the Planck distribution, modified because the entropy gained/lost by absorbing/emitting a photon to excite between levels with a different potential difference is $\frac{h\nu - qV}{T}$ rather than $\frac{h\nu}{T}$. This gives us

$$I_{out}(\nu)d\nu = \frac{8\pi n_s^2 \nu^2}{c^2\left(\exp\left(\frac{h\nu - qV}{k_b T_c}\right) - 1\right)}\alpha d\nu \tag{2.42}$$

as shown by Ross [133], for T_c = temperature of cell. We may safely make the Boltzmann approximation (neglect the -1) in this equation, as the wavelengths of interest are much

greater than the energy separation. The definition of η, the external photoluminescence quantum efficiency (PLQE), is

$$\int d\nu\, d\Omega_{out}\, \mathscr{T}_{out}\, I_{out} = \eta \int d\nu\, d\Omega_{in}\, \mathscr{T}_{in} I_{in}, \tag{2.43}$$

for $\mathscr{T}_{in}$ the transmission coefficient for incoming light and $\mathscr{T}_{out}$ that for outgoing light. This equation can be combined with equation 2.42 to obtain

$$\exp\left(\frac{qV}{k_b T_c}\right) \int \frac{8\pi n_s^2 \nu^2}{c^2} \frac{\alpha d\nu}{exp\left(\frac{h\nu}{k_b T_c}\right)} \int \mathscr{T}_{out} d\Omega_{in} = \eta \int I_{in} d\nu \int \mathscr{T}_{in} d\Omega_{out}. \tag{2.44}$$

The angular and intensity integrals are separate here. It may be demonstrated that the ratio of the angular integrals is the same as the ratio of étendues [126] of incoming and outgoing light. The étendue of light is defined by $d\varepsilon = n_s^2 \cos\theta\, d\Omega dA$ for dA an elemental area and θ the angle between the light and the normal to the surface. This is a quantity akin to entropy for an optical system [19]. After making this substitution and rearranging equation 2.44, this leaves us with

$$\exp\left(\frac{qV}{k_b T_c}\right) = \eta \frac{\int I_{in} d\nu}{\int \frac{8\pi n_s^2 \nu^2}{c^2 \exp\left(\frac{h\nu}{k_b T_c}\right)} \alpha d\nu} \frac{\varepsilon_{in}}{\varepsilon_{out}} \tag{2.45}$$

$$\Rightarrow V = \frac{k_b T_c}{q} \log\left(\eta \frac{Q_{in}}{Q_{out}} \frac{\varepsilon_{in}}{\varepsilon_{out}}\right), \tag{2.46}$$

for $\varepsilon_{in(out)}$ = étendue of incoming (outgoing) light, Q_{in} the total light that would be absorbed by the cell, if the solid angle of the sun was 4π, and Q_{out} the light emitted by the cell in thermal equilibrium. A solar cell with optimised carrier extraction therefore has a maximum driving potential of

$$V_{oc} = V = \frac{k_B T_c}{q} \log\left(\frac{\eta Q_{in} \varepsilon_{in}}{Q_{out} \varepsilon_{out}}\right) \Rightarrow V_{oc} = V_{ocMax} + \frac{k_B T_c}{q} \log(\eta). \tag{2.47}$$

We should emphasise that $\log(\eta)$ is a nonpositive quantity as $\eta \leq 1$.

The advantage of recycling can then be expressed in terms of an increased PLQE: a photon given many recycling events has several attempts to find the escape cone, resulting in a higher η, whereas other means of increasing access to the escape cone (e.g. reducing the refractive index difference) typically would also widen the etendue of the cell. Comparing a recycling system to a system where all emitted light is lost, we find that the resulting change in V_{oc} is given by $\Delta V_{oc} = -\frac{k_B T_c}{q} \log(p_e)$, for p_e the probability that light escapes [78]

It is worth noting that photon recycling is not an additional process to add to these device-level calculations, but is already included in the measured values of η. Indeed, if we express it as the escaping fraction of radiant recombination (internally R_{rad}, of which the photon recycled component p_r is recovered and the remainder, p_e, escapes), we find that

$$\eta = \frac{p_e R_{rad}}{(R_{nrad} + p_e R_{rad})} = \frac{(1 - p_r)QE}{1 - p_r QE}, \tag{2.48}$$

for R_{nrad} the nonradiative recombination and QE the internal quantum efficiency. This means that increasing the photon recycling probability of radiant light reduces the external efficiency and therefore V_{oc}. However this is a measure of light trapping inside the solar cell for a given QE. We instead wish to increase QE, which will increase the total amount of photon recycling that occurs because there are more photons to recycle. Light trapping will increase the current output (since it results in higher internal carrier densities) but has detrimental effects on the V_{oc}, whereas increasing the probability of light escape by, say, texturing the front surface of the cell [168], tends to be associated with higher internal light transport distances. In principle, reducing the angle of emission of photons to equal the angle of excitation produces significant overall efficiency benefits, however in practice, even small amounts of nonradiative recombination significantly reduce this benefit [102].

Chapter 3

Reduced Dimensionality in Drift-Diffusion Models of Back-Contact Solar Cells and Scanning Photocurrent Microscopy

3.1 Introduction

In thin-film solar cells, one type of carrier is typically extracted from the front surface through a transparent conducting electrode and the other through the back layer, via a reflective metal electrode. However, as transparent materials are always limited in conductivity, other cell designs are also used. One group of designs features both types of electrodes on the back side of the device: back contact solar cells [158]. The front of the solar cell can then be freely designed for optimum optical properties and the rear for electrical properties [176], [62]. Alternatively, the front transparent conductive layer can be replaced with a grid of opaque metal – provided the diffusion length of charges in the material is large and hence the grid can be coarse, the area overshadowed by the electrodes need not be large, and conduction to the high-conductivity grid can happen through the bulk [109], [52]. However these designs significantly complicate the modeling of carrier motion in cell operation; for unpatterned cells, a simple one-dimensional model of behavior perpendicular to the plane of the cell is sufficient, but with electrodes placed in patterns, lateral carrier motion must also be investigated. Typically the problems are appropriate for drift-diffusion modeling, a semi-classical macroscopic transport model based on the continuity equations and Poisson's equation [71]. Drift-diffusion models in two and sometimes three dimensions [27, 48, 155, 20, 105] are

well-known in papers devoted to modeling, but for computational ease or to give analytical solutions, it is generally preferred that the simulation be set up to require as few dimensions as possible. In this report, we will investigate conditions for reducing the dimensionality of the models. We will use device parameters in keeping with dopant-free methylammonium halide perovskite performance for example purposes. Perovskites were chosen as an example system of great interest due to achieving high power conversion efficiencies in a short space of time [117], however we do not attempt to model the specifics of these devices here.

We will first investigate uniform illumination, in which case the model is approximately two-dimensional, and find the conditions under which we may model this in one, lateral dimension. Having established this, we will then investigate how this applies to a scanning photocurrent microscope setup (also known as optical beam-induced current, or OBIC). In this system, a small laser spot excites a region of semiconductor and the current that reaches electrodes is monitored [57]. Here we see lateral transport of carriers under point illumination, but the symmetry-breaking effect of the localized illumination means the full solution is three-dimensional. We will show that in many experimental cases, this will give rise to a current that decays exponentially with distance from the patterned electrodes, and that this current is reached with a characteristic time-delay linear in distance.

Point illumination experiments on planar systems are used to investigate carrier dynamics in the active layer of solar cells or transistors, for instance carrier diffusion and recombination, in a wide variety of materials and systems [110, 123, 72, 135, 111, 157, 95]. There are also experimentally different setups that give rise to mathematically similar problems, such as electron beam-induced current measurements of solar cells [44]. These techniques are often used to study nanowires, where the analysis needs only one dimension [57]. In the planar systems considered here, the problem to be solved is more complex, yet in experimental papers on three-dimensional materials such as these, only one-dimensional, simplified versions of the drift-diffusion equations are solved. As shown numerically for a two-dimensional system by [57], we may then extract the diffusion length of carriers from this measurement - it is given by the lengthscale of the exponential decay of the current. This is in keeping with the monoexponential decays often encountered experimentally [110, 157, 95], however the conditions under which the approximation holds have not been investigated. Here, we will demonstrate the similarity of numerical and analytic solutions and therefore the applicability of the analytic solutions to a range of problems. We will also investigate what physical parameters can be extracted from these analytic solutions in different cases. We will further show that the delay between signal and measurement gives another avenue to investigate carrier behaviour and explain how these measurements can be combined.

3.2 Investigating the appropriateness of one-dimensional models for lateral diffusion

For many back-contact electrode systems, the electrodes are hundreds of microns in one lateral dimension but only microns in the other, and around a tenth of a micron in height. Under uniform illumination, there will be no variation over the largest dimension, except near the edges of the cell. We can therefore model only the cross-section of the device, as shown in Figure 3.1a. However the smaller dimensions must be treated more carefully, so we will set up a two-dimensional model and investigate when it can be contracted to one, lateral dimension.

The two-dimensional drift-diffusion simulations are loosely based on perovskite quasi-interdigitated solar cells as found in [70]. The geometry of the structure is either step-shaped, with one electrode raised, as in [70] and Figure 3.1b, or flat, with both electrodes level on the bottom, as in Figure 3.1c. In the step case, the anode runs along the entirety of the base but the cathode only runs along 90% of the raised step, to present a 'lip' of the insulator. The cathode is raised by 150 nm, out of a total height of 350 nm. The flat structure has electrodes along 90% of each half and an insulating patch in-between. The horizontal edges of the simulation are the middles of the electrodes – with uniform illumination, these will be symmetry lines of the system. At the insulating boundaries and the symmetry lines, zero perpendicular electric field and zero electron/hole current conditions are imposed. Within the active area, carriers are generated a rate that exponentially decays from the surface. They travel and recombine according to the steady state drift-diffusion equations as described in the supplementary material. Under the conditions used, recombination will primarily be Shockley-Read-Hall (SRH). The simulations do not include ions or dopants, and are performed with no effective applied field. The materials parameters can be found in table 3.1.

We assume that in two or three dimensions, the current flux into an electrode is proportional to the local concentration of one carrier type at the interface: $J = qv_s n_{interface}$, for q the carrier charge. It is assumed that blocking layers mean that each electrode selectively accepts only one carrier type. If surface recombination is included, it may be considered in the same way, with a smaller v_s for the majority carrier type. This physical extraction velocity v_s may tend to infinity and zero in the Ohmic and blocking cases respectively.

To vertically contract this and make a 1D system, the relationship between the electron or hole current into the electrode and the average carrier density above should be simple; to avoid detailed modeling, it should preferably be linear. Since with no carriers we have no

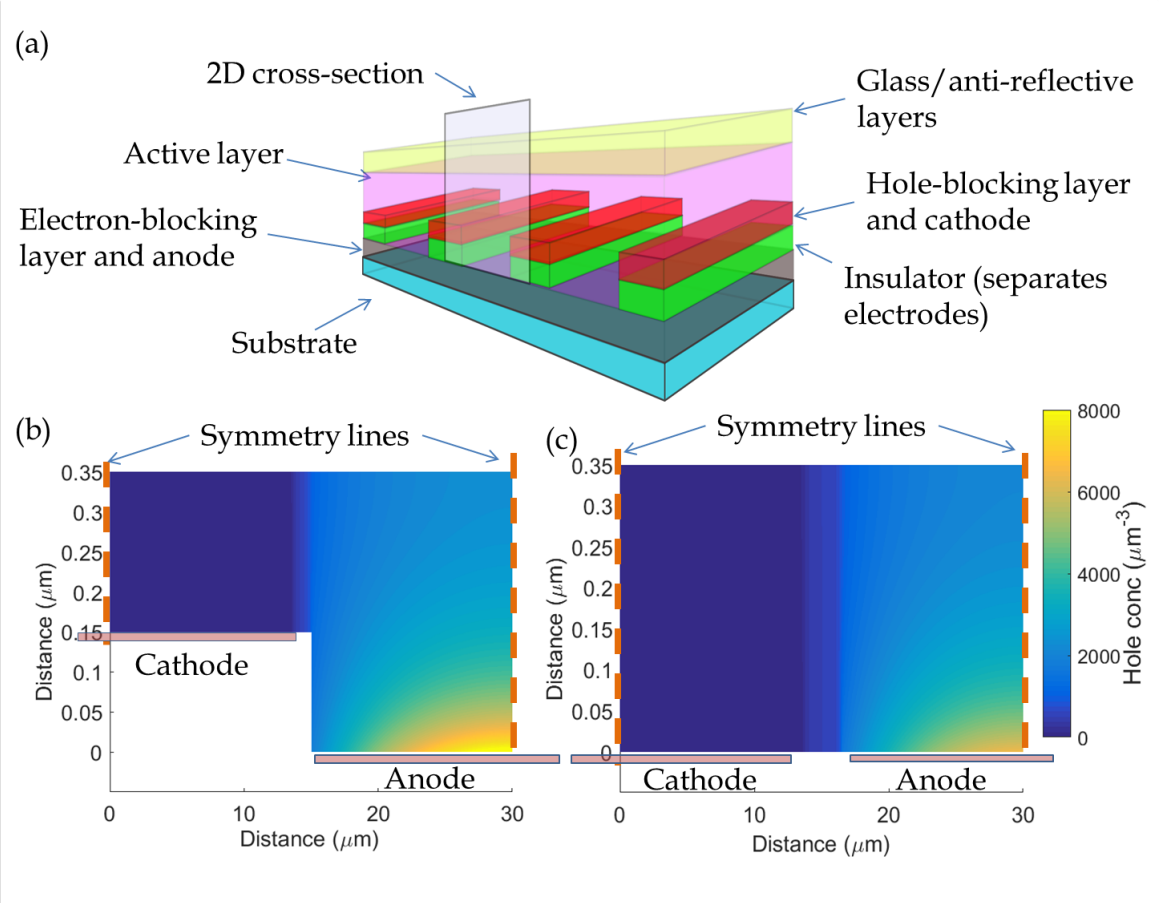

Fig. 3.1 Reducing back-contact solar cells to two dimensional objects. The lower images are different geometries for two-dimensional cross-sections of three-dimensional structures like (a), with (b) simply projected, leaving a step-shaped active layer, and (c) an alternative design with the anode/electron-blocking layer level with the cathode/hole-blocking layer. The symmetry lines represent the midpoints of the electrodes, about which there is reflective symmetry. Simulations conducted using the default parameters explained in the supplementary materials, designed to be realistic for perovskite systems.

current, the linear trend has zero offset:

$$J = qv_{1D}\overline{n}, \tag{3.1}$$

for $\overline{n}$ the vertically averaged carrier density and v_{1D} the effective extraction velocity. We therefore run the simulation with many values of v_s and plot the dependence of current extracted against the vertically averaged carrier concentration at that x-position for each simulation, and search for a linear trend.

Symbol	Description	Value	Source
h	Height	350 nm	Input
L	Pitch length	2 μm	Input
ε_r	Static dielectric constant	100	[93]
T	Temperature	293 K	Input
D	Electron and hole diffusion constant	1.5 cm^2/s	[37, 144]
τ_1	Trap fill time	0.1 μs	[144]
n_t	Trap density	1×10^8 cm^{-3}	Small number
k_2	Bimolecular decay rate	1×10^{-10} cm^3/s	[123]
v_s	Extraction velocity	1×10^7 cm/s	Large number
α	Absorption coefficient	1×10^{-7} m^{-1}	[123]
I_i	Incident radiation at absorbed wavelengths	1.7×10^{-21} m^{-2}/s	[116]

Table 3.1 The values used in all simulations unless otherwise specified, based around good methylammonium lead halide perovskite device performance.

Figure 3.2a shows the relationship between the current density flowing into a short stretch of an electrode and the vertically averaged electron concentration above it, for data taken from anodes below a step. We see that in systems with wider electrodes this zero-offset linear trend from equation 3.1 is usually shown to be a good assumption, although non-linearity is visible at either ends of the trend.

At the low-concentration end, this is due to a population of carriers held away from the electrodes. This arises due to attraction between the carriers, one type of which is blocked from the electrode below. The high concentrations of blocked carriers give rise to voltage extrema above the centerpoints of the electrodes that keep the accepted carriers away from the electrode (these can be seen in Figure 3.3a). This effect is therefore not seen in Figure 3.2b, where the lengthscale and carrier concentrations are too small for the total voltage difference over the system to be large compared to the thermal voltage, $V_T = k_B T/e$. We can show that these effects can be ascribed to electric field effects by removing them. By setting the charge of both electrons and holes to zero, we obtain a slight variation in the current-concentration graphs, plotted in Figure 3.3b and d. The limited differences indicates that charge has a relatively minor effect on the system but the lack of nonlinearity at the low-current density end suggests charges effects are responsible for slight pooling of charge there. Since this occurs at low carrier concentration, the net effects of this nonlinearity on the system are small. We see that at the high concentration end, there are still irregularities without an electric field due to factors affecting diffusion and recombination, although they are smaller than with the field effects.

In the high extraction velocity limit, there is a slight decrease in current extracted below the step of the electrode, as many of the electrons are initially generated above the step and

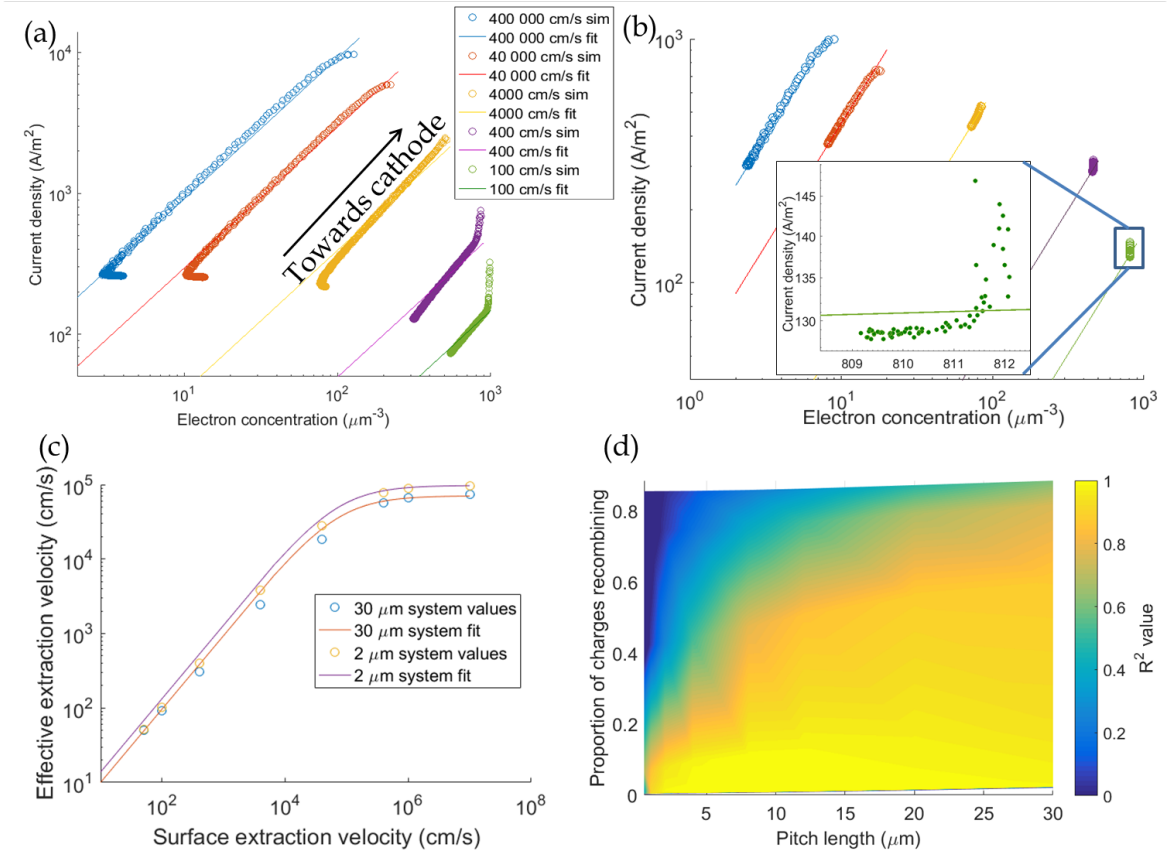

Fig. 3.2 (a, b): Relationship between current extracted and vertically averaged electron concentration for a variety of extraction velocities, for the lower electrode for (a) 30 µm simulation pitch length (b) a 2 μm pitch length. Inset magnifies the distribution in the 100 cm/s simulation. Arrow in (a) shows physical direction, from the midpoint of the anode to the part nearest the cathode. (c): relationship between extraction velocity at the electrode and effective one-dimensionally averaged extraction velocity (e.g. gradient of lines in (a)) for flat electrodes of different lengths. (d): Coefficient of determination, R^2, for the linear fits to density-concentration data as in (a) and (b). (All images): Both carrier types have a diffusion constant of 1.5 cm^2/s and distributions are from a step-electrode system, as in Figure 3.1b.

therefore have slightly further to travel to reach the electrode compared to those generated above it. However, when charge extraction is slower, charges mill around for longer so recombination is more important and the precise location of generation less important. In the low extraction velocity limit we see a strong increase in current from a small increase in concentration, arising near the step. This is because there are fewer holes here, and therefore proportionally less recombination. Charges therefore are more likely to diffuse out of the system, either vertically or horizontally. With much smaller systems, there is little variation in either the collected current or the vertically averaged carrier density, as seen in Figure 3.2b.

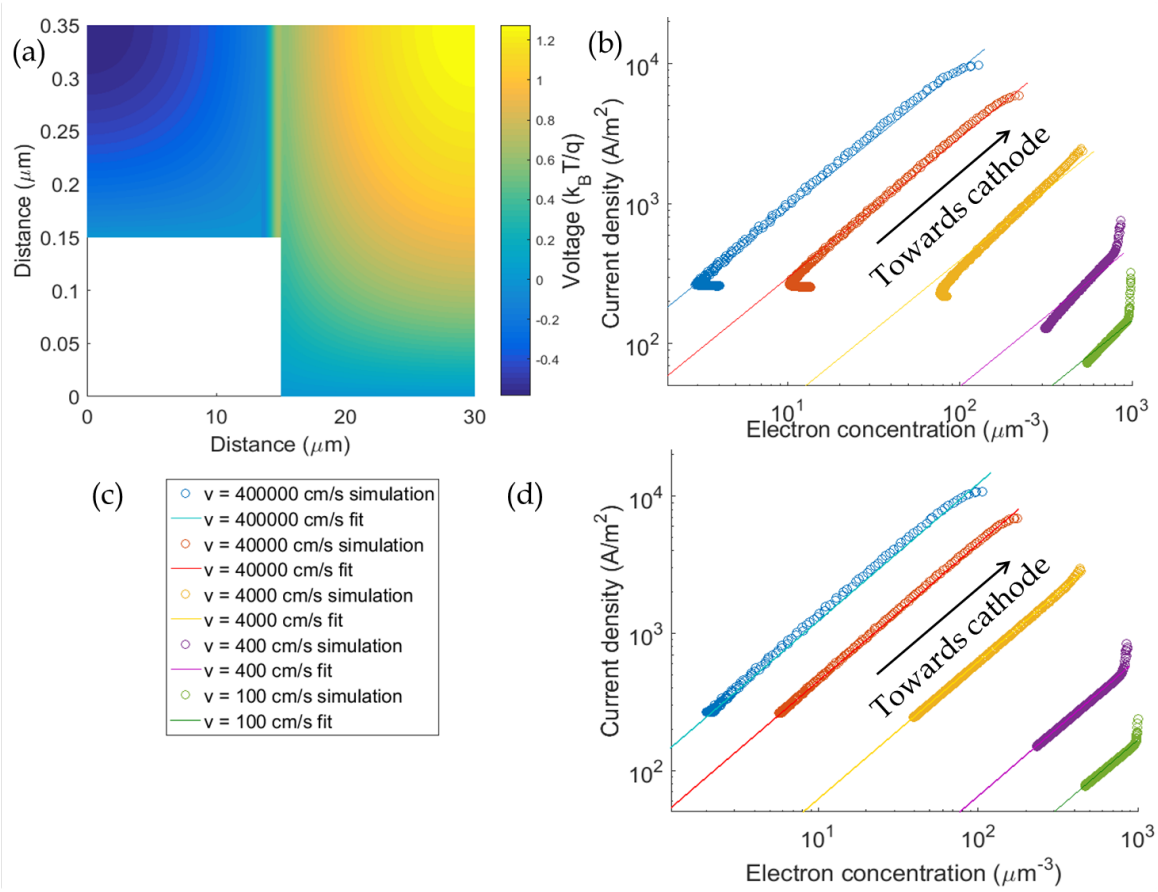

Fig. 3.3 (a): Example voltage distribution, in units of thermal voltage. (b-d): Relationship between current extracted and vertically averaged electron concentration in a 30 μm system, as in Figure 2a of the main document, here comparing the simulation run (b): normally and (d): with all electric field effects turned off. Arrows show physical direction, from the midpoint of the anode to the part nearest the cathode. (c): Legend for (b) and (d).

This is because the lateral diffusion and vertical diffusion are comparable to each other and to the carrier diffusion length, allowing homogenisation.

3.2.1 Expressions for the effective velocity

The trend lines of graphs like these give us the value of the effective extraction velocity, v_{1D}, from equation 3.1. Figure 3.2c shows how this varies with the actual extraction velocity. We see that in the slow-extraction limit, the effective extraction velocity equals the extraction velocity at the electrode. This is because the carrier concentration becomes fairly uniform, so $n_{interface} \approx \overline{n}$ and $v_{1D} \approx v_s$. In the high extraction velocity limit, the concentration at the electrode tends to 0 and the effective velocity tends to a diffusion-dominated value.

However we also need to consider the accuracy of the fit itself. To explore this systematically, we investigate what proportion of the variance of the data can be ascribed to the linear fit and what proportion needs a more complicated model. The R^2 value of a fit measures what fraction of the variability that fit explains. We see in Figure 3.2d that systems smaller than about 0.35 μm (the system height) have a poorer fit and a lower R^2 value, as do those with a lower extraction speed. The physical explanation for the latter is that it increases the impact of recombination on the system. Recombination competes with charge extraction in non-trivial ways, as it depends on the concentration of countercharges. We find that R^2 values are always greater than 0.95 for systems with more than half of the charge extracted, provided the system is at least three times wider than it is high. However, as shown in appendix 1 (chapter 7), if we are concerned with the proportional error in the fit rather than the R^2 value and explanatory power of the model, problems also emerge for long systems - in this case, large relative errors occur with a pitch length over 15 μm. This is mainly because in larger systems there are more charges near the edge of the electrodes, magnifying the effects of any nonlinearity.

The form of the effective extraction velocity can also be estimated. We require the current at the interface to equal the effective current out from the bulk: $j_n = v_{1D}\bar{n} = v_s n_s$. The carriers arrive at the interface largely by diffusion, and we can approximate this as $j_n = (\bar{n} - n_s)v_d$ for some diffusion speed v_d. Equating these and eliminating the carrier concentrations, we find the effective velocity is the harmonic mean of the extraction velocity and the diffusion speed:

$$v_{1D} = \frac{v_s v_d}{v_s + v_d}. \tag{3.2}$$

We see in Figure 3.2c that equation 3.2 fits well, with R^2 values consistently above 0.99 if v_d is fitted to the system. We expect the value of this diffusion speed to change upon changing the diffusion constant, so to investigate this we plot the behaviour of the system when one carrier (holes in this case) has its diffusion constant changed. Results are plotted in Figure 3.4a, for high extraction velocity (v_s=1000 000 cm/s), where we expect $v_{1D} = v_s$. Figure 3.4b then plots the effective velocity as a function of diffusion constant for many such experiments with different electrode lengths. We see the relationship is fairly linear at first, although falls off, particularly for larger systems.

This trend may be compared with one-dimensional expectations. In the low extraction velocity regime, we expect the relationship $v_{1D} = v_s$, and can see the relationship holds well in Figure 3.2c for $v_s \ll v_d$. In the high extraction velocity regime, with no recombination, no electric fields and with a simple exponential Lambert-Beer law generation function, we expect $D\nabla^2 n = -A\exp(\alpha z)$, for α the absorption constant, A the density of photons absorbed

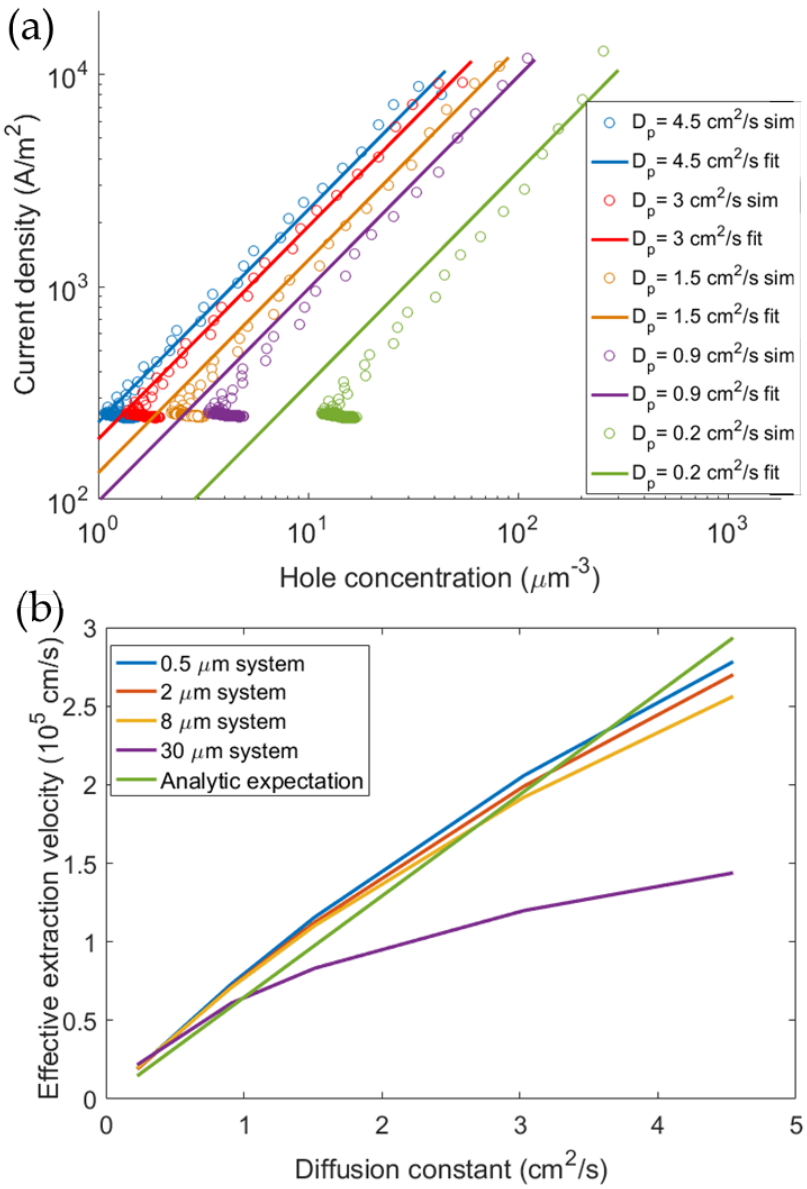

Fig. 3.4 (a): The relationship between mean hole concentration and hole current density when the diffusion constant of the holes is varied but that of electrons left constant at 1.5 cm^2/s, for a 30 μm system. There are no other differences between electrons and holes in this system. Data from simulations in flat systems with a surface extraction velocity of 10 000 cm/s. (b): how the effective velocity depends on the diffusion constant in simulations of different lateral width. Simulations as in (a).

at the bottom of the device and z the vertical height, with maximum h. We have the boundary conditions $n(0) = 0$, due to fast recombination at the interface, and $\partial n/\partial x(h) = 0$ since

there is no extraction at the surface. This has solution

$$\begin{aligned} n(z) &= \frac{A}{D\alpha}\left(\frac{1-\exp(\alpha z)}{\alpha} + z\exp(\alpha h)\right) \\ \Rightarrow v_d &= \frac{D\nabla n|_{x=0}}{\overline{n}} = \frac{D(\exp(\alpha h)-1)h}{\frac{h}{\alpha} - \frac{e^{\alpha h}}{\alpha^2} + \frac{1}{\alpha^2} + \frac{h^2}{2}e^{\alpha h}}. \end{aligned} \tag{3.3}$$

This has a limit of $3D/h$ as $\alpha \to 0$ (i.e. under vertically uniform illumination), and is $2.3D/h$ for the values in our simulation.

As can be seen in Figure 3.4b, at high extraction speeds and low diffusion constants this matches with detailed, two-dimensional simulations including electric fields and recombination, particularly for smaller systems, but begins to break down in larger systems when electron and hole diffusion constants are very different. For wider systems (i.e. width approaching 100 times the height), the carrier buildup is substantial, resulting in electrostatic potentials that are comparable to the thermal voltage. There are also higher levels of recombination so we expect to see the failure of equation 3.3. However for systems narrower than this but wider than the system height, the analytic expressions obtained by combining equations (3.2) and (3.3) provide a good description of the system.

To show where and why these analytic expressions fail, we investigate the effects of varying both the diffusion constant of the holes and the electrons, whereas previously electrons always have a diffusion constant of 1.5 cm^2/s. In Figure 3.5a and b we see that the nonlinearity in the long system becomes significant around the $D_n = D_p$ point, where the analytic hole and electron extraction velocities are equal, and is minor for holes in all simulation lengths before that. In Figure 3.5c, we see that the electrons are usually unaffected by changing the diffusion constant of the holes, except again in the case of very wide systems, where a more complex model is needed for unequal diffusion constants. The electrons in the 30 μm system deviate from the analytic electron trend below the crossover point, which shows that it is the imbalance of the two diffusion constants that creates the problem, not that one is too high. In combination with the other two graphs, we see that in larger systems, both carriers have their effective extraction velocity limited by the smaller of the two diffusion constants.

3.2.2 Recombination

In order to one-dimensionalise the system, we also need to be able to calculate the actual recombination from the vertically averaged n and p values. In the limit of one carrier type being very scarce (say, n), the SRH recombination equation reduces to $R = n/\tau_1$, in which

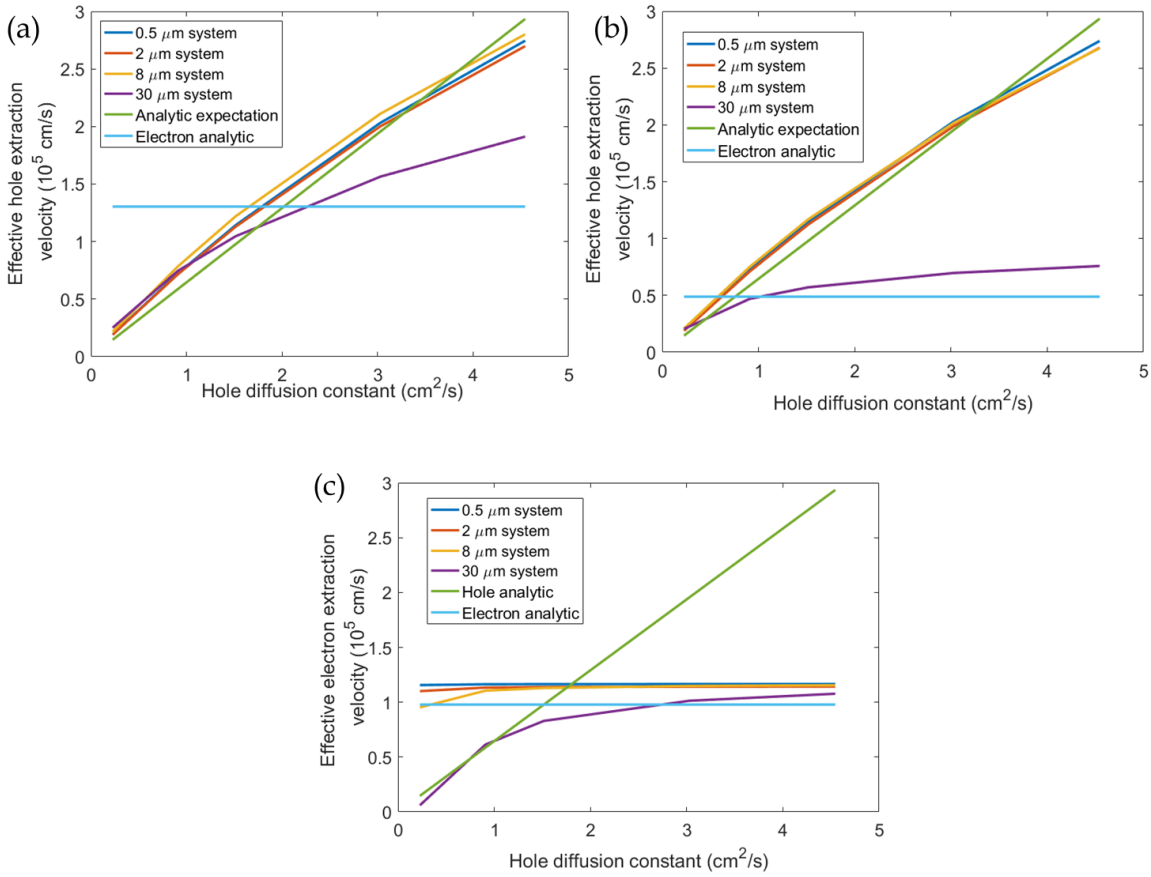

Fig. 3.5 (a, b): Relationship between effective extraction velocity and the diffusion constants of the holes, as in Figure 3b, here with two different values of electron diffusion constant (a): $D_n = 0.76$ cm^2/s, (b): $D_n = 2$ cm^2/s. The horizontal light blue lines indicate the analytically expected extraction velocity of the electrons in the same system, showing the crossover. (c): Relationship between the effective extraction velocity of the electrons and the diffusion constant of the holes, for an electron diffusion constant of $D_n = 1.5$ cm^2/s, as in Figure 3b. The horizontal light blue line is now the analytic expectation for the electron behaviour plotted, the green illustrates the crossover. (All images): Data from simulations in flat systems with a surface extraction velocity of 10 000 cm/s.

case using the vertically averaged value of n will work exactly. The situation is nontrivial if both species are common enough that there is a significant component of bimolecular recombination, or if both species have similar concentrations, so that the SRH recombination is limited by both species. In these cases, the applicability of the one-dimensionalised model depends on how the density of carriers changes thoughout the film.

Figure 3.6a shows the relationship between electron concentration and recombination when vertically averaged over the anode of a flat system, in the limit of fast charge extraction. We see that in systems with wide pitch distances, recombination matches the simple limit,

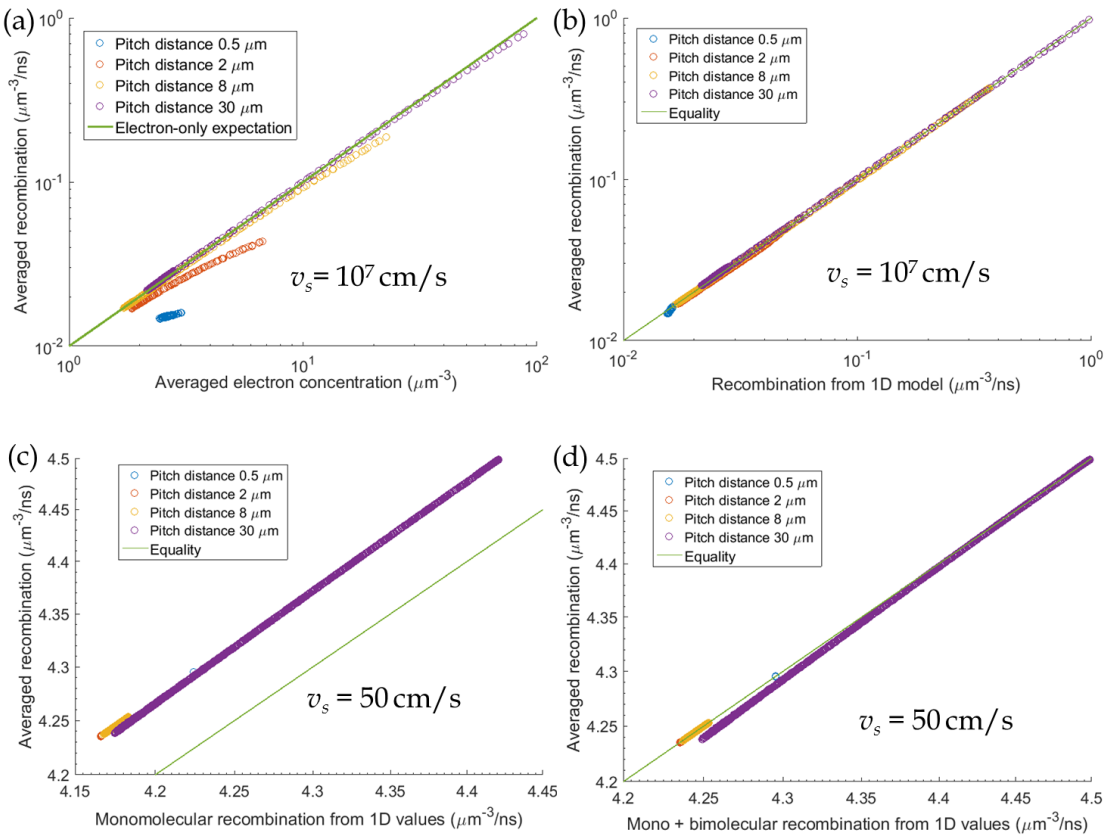

Fig. 3.6 (a): Relationship between the vertically averaged minority carrier (electron) concentration and the vertically average recombination in a flat system with extraction velocity 10 000 000 cm/s at both electrodes and no surface recombination. The data is taken over the electron-accepting anode. This is compared to the simplest, electron-only model. (b): Relationship between the one-dimensional monomolecular recombination that would be expected, given both the vertically averaged electron and hole concentrations, and the total recombination calculated in the full two-dimensional model. Data taken from the same simulations as in (a), but across the whole simulation. (c,d): The same as (b), but with extraction velocity 50 cm/s at both electrodes. (d) includes both monomolecular and bimolecular terms in the one-dimensional recombination calculation.

n/τ_1. This is not the case in smaller systems, where there is clear deviation from this line, which is due to both carrier types having similar concentrations. This means we cannot prove that averaged values of carrier concentrations will give us the correct amount of recombination. However, in Figure 3.6b we compare the actual averaged recombination with the recombination calculated from averaged values, including data from across the device. We see that the recombination is satisfactorily described by the full, one-dimensionalised relationship for all electrode widths. This is because bimolecular recombination is minor

in all cases, and the absolute variation in carrier concentration over the height of the cell is small for the minority carrier.

In the limit of slow charge extraction, charge accumulates and bimolecular recombination becomes relevant. Figure 3.6c shows that the monomolecular-only model fails to describe the system. In this case, the accuracy of the one-dimensionalisation is highly conditional on the precise nature of carrier distributions, however we see in Figure 3.6d that it is still typically very accurate, if less accurate than the case with only monomolecular recombination in Figure 3.6b. This is because in this limit, we see very little variation in carrier concentration with height. If bimolecular recombination is dominant at low particle concentrations, modeling it may be more problematic.

For situations like ours, recombination may therefore be easily and accurately modelled using only averaged n and p values. Generation is not dependent on carrier concentration, so while it may need a two-dimensional calculation to establish what value should be used, it is not problematic to use a one-dimensional value for it in calculations. This means that if the electrode extraction current is amenable to one-dimensionalisation, so is the whole system.

3.3 Application to scanning photocurrent microscopy

In scanning photocurrent microscopy, we scan a narrowly focused laser beam over the sample, as illustrated in Figure 3.7a. We may either scan between electrodes, on top of one electrode, or beyond the active area, next to sets of electrodes. We now apply the analysis above to reduce the dimensionality this problem. Under uniform illumination, an infinite back-contact solar cell usually has reflective symmetry about the center of each electrode, however this is broken by localised illumination, necessitating more complex models. The illumination itself has rotational symmetry, but the electrodes occur in laterally symmetric strips; the combination gives us only one line of reflective symmetry through the centre of the illumination.

Experiments usually involve illuminating a film either away from the electrodes (case one, as in [95, 123]), or are on top of one extended electrode (case two, as in [73, 110]) in which case we will soon extract all of one carrier type and measure only the spread and surface recombination of the remaining carrier. The two cases are illustrated in Figure 3.7a. In both case one and two, we will see that the general coupled drift-diffusion equations can be simplified into one equation in two dimensions. We begin with the standard three-dimensional

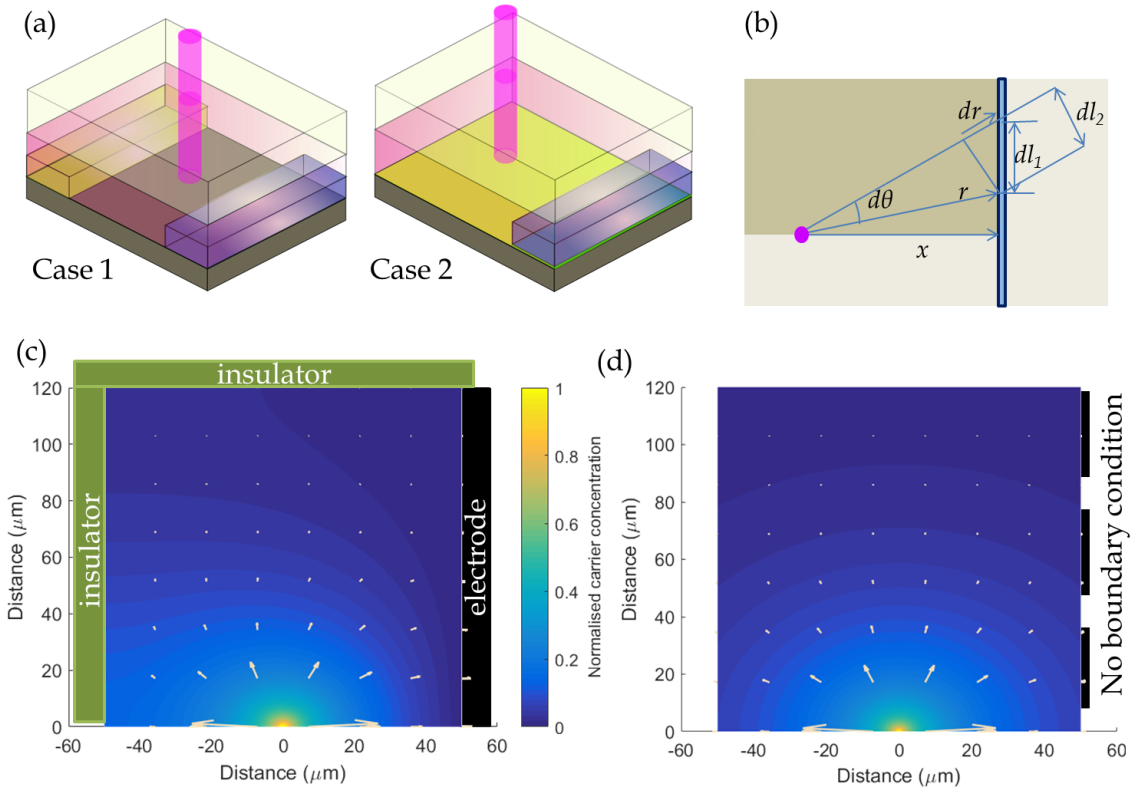

Fig. 3.7 (a): Diagram of point-illumination of back-contact system with two electrodes. In case one, illumination is between electrodes. In case two, one electrode is extended over the whole surface. (b): Top-down view of (a), with one electrode neglected and lengths labelled. Simulated area is shaded darker brown. (c): Numerical solution to the point-excitation problem in 2 dimensions. The solution has a 0-concentration condition imposed at $x = 70$ and zero-flux, reflective boundary conditions at other borders. Excitation is at the origin, where concentration is normalised to one. Arrows indicate current flow. (d): Analytical, Bessel function solution to the point-excitation problem in two dimensions, with no boundary conditions imposed at any border. Note that it matches the y = 0 reflective boundary by symmetry. Excitation is at the origin. Integration to find current performed along the dotted line, representing the electrode. Scale is as in (c), values are normalised to one at half a micron away from the origin and saturated within. (c,d): White arrows indicate direction and magnitude of carrier diffusion.

steady state drift-diffusion equations:

$$-\nabla\cdot\begin{pmatrix} D_n\nabla n+\mu_n n\mathbf{E} \\ D_p\nabla p-\mu_p p\mathbf{E} \\ -\varepsilon\mathbf{E}\end{pmatrix}=\begin{pmatrix} G-R \\ G-R \\ q(p-n)\end{pmatrix}, \tag{3.4}$$

[11] where $D_{n\,(p)}$ are the electron (hole) diffusion constants, $\mathbf{E}$ is the electric field, G is the generation function and R is recombination. By applying the findings from earlier in the paper, we may two-dimensionalise these three-dimensional equations. The vertical boundary conditions may be replaced by an extraction term subtracted from the right hand side of the first two lines, representing either the effects of electrodes or surface recombination.

In the second case, illuminating over an extended electrode, we have only one carrier in most of the film and may neglect the other. There may be some recombination before all of one carrier is extracted, meaning that the effective generation function for the remaining carriers is smaller than the actual generation function, however there are no other effects at distances larger than both the beam width and film thickness. In this case we can approximate the carrier generation function to a point source with modified magnitude. We find that the image charge from the electrode cancels out the in-plane space-charge effects of the remaining carrier. The perpendicular electric field may influence the effective extraction velocity but does not influence the horizontal behaviour of the system, therefore for our case of no perpendicular electric field, we can neglect the effects of charge in two dimensions.

This also means that we also need only keep track of one carrier type. As established previously, in most cases we may approximate extraction of carriers from the bottom electrode (or surface recombination there, which appears identical) by an effective bulk extraction, and if recombination is monomolecular, away from the generation region we have the following steady-state equation:

$$D\nabla^2 n - vn = 0 \tag{3.5}$$

for D the remaining carrier diffusion constant and v the effective surface extraction (or surface recombination) velocity divided by the film height.

A similar situation arises if we have strong enough doping and weak enough illumination that the optically generated carriers are much rarer than the majority dopants, such as in the scanning photocurrent experiments on a transistor performed by Ubrig et al. [157]. Here, the concentration of the majority carrier is largely unchanged by illumination, and only the minority carriers need be tracked.

If we return to case one, a film with no electrode underneath, we may derive a similar equation. In systems like this, both electrons and holes are mobile but have different diffusion constants. Here, we must consider the phenomenon of ambipolar diffusion, where the electrons and holes diffuse together, which occurs when there is no selective extraction or injection of one carrier [113, 140]. The electrostatic attraction between the electrons and holes ensures that the faster species is pulled back and the slower is pulled forwards. This attractive effect will force the distributions of the carriers to be (almost) identical, with a diffusion constant somewhere in between that of electrons and holes. Since their populations

behave the same, in our undoped case, $n = p$, the electric fields are screened and there is no long-range net electric field generated by the charges [140]. This means that the last line of equation (3.4) is not needed, and the first two lines are identical.

The value of the ambipolar diffusion constant is (from [113])

$$D_a = \frac{2D_n D_p (n+p)}{D_n n + D_p p}, \tag{3.6}$$

however if excitation levels are higher than doping levels (as might be expected for perovskites) then ambipolarity means $n = p$ and so $D_a = 2D_n D_n/(D_n + D_p)$. Assuming we have only monomolecular recombination, which may include both a bulk and an interface component, we can make this the v term in equation (3.5). The overall behaviour in these two cases can be modelled in the same way.

If our situation is circularly symmetric, equation 3.5 becomes

$$\frac{D}{r}\partial_r (r\partial_r n) - vn = 0 \tag{3.7}$$

$$\Rightarrow r^2\partial_r^2 n + r\partial_r n - \frac{v}{D}r^2 n = 0 \tag{3.8}$$

If we define the inverse of the diffusion length as $a \equiv \sqrt{v/D}$, then we recognise this equation as the zeroth-order modified Bessel's equation with solution

$$n(r) = AK_0(ar) + BI_0(ar), \tag{3.9}$$

an arbitrary sum of the zeroth-order I and K modified Bessel functions. No I_0 term is allowed on an infinite plane since it will diverge at large distances. The divergence of K_0 at 0 is permissible since we assumed a point generation function, an approximation that is only valid outside the real generation width. A mathematical complication emerges because charges are usually collected by a linear electrode, so we need to integrate this n along a line to compare this fit to measured currents. Also, the electrode absorbs carriers, and may therefore perturb the carrier density, breaking the circular symmetry of the solution. There are two ways to approximate this interaction: either the electrode extraction rate is fast and no carriers are present for $x > x_0$, or it is slow and does not significantly perturb the carrier level. If the extraction is fast, we should impose a boundary condition which breaks the cylindrical symmetry of the Bessel function solution, whereas we can ignore it for slow extraction.

However by comparing the normalised Bessel function solution with the numerical solution (as seen individually in Figures 3.7c and d, and compared numerically in Figure 3.8a), we observe that the 0 carrier condition makes little difference to the solution except

close to the electrode and therefore the numerical value of $J(r)$ in the bulk can be estimated accurately from the analytical solution. The symmetry plane at the x-axis corresponds to a true 0-derivative (Neumann) boundary condition, which the Bessel function solution respects. We impose similar conditions on the numerical model at the arbitrarily placed upper and left limits (labelled as 'insulators' in Figure 3.7c), however these are far from the excitation and only locally affect results, as seen in Figure 3.8a. The impact of the $n = 0$ (Dirichlet) boundary condition on the right is also local, and the Bessel function solution is accurate a short distance away. Furthermore, we see in Figure 3.8b that, in terms of the net current into the electrode, the impact of this difference is negligible. In the case of moderate recombination (v=1 μs^{-1} so $a = 0.026\ \mu m^{-1}$), the curves are hard to distinguish, with minor differences in the limit of small surface recombination ($v = 0.1\ \mu s^{-1}$ so $a = 0.082\ \mu m^{-1}$), such as might arise in a 300 nm high film with a recombination velocity of 3 cm/s).

Due to the similarity of the results from the two solutions and the tractability of the analytic, boundaryless approximation, we will derive analytic expressions for the current in both the fast and slow extraction cases. In the fast extraction case, the total current can be found by simply taking the line integral of the current density along the electrode. In the slow-extraction regime, the current extracted is proportional to the unperturbed carrier density over the electrode. These two models result in different relationships between current and concentration but it will be shown that after being normalised, they produce identical current trends.

In the slow-extraction limit, we are interested in the integral of the carrier distribution over a line, (see geometry labels in Figure 3.7b) with elemental length $dl_1 = \sqrt{dr^2 + (rd\theta)^2}$. As we are constrained to $r\cos\theta = x$,

$$dl_1 = \sqrt{dr^2 + \left(\frac{xdr}{\sqrt{r^2 - x^2}}\right)^2} = \frac{rdr}{\sqrt{r^2 - x^2}}. \tag{3.10}$$

We can then calculate the current,

$$I_1 \propto \int_x^\infty K_0(ar)\,\frac{rdr}{\sqrt{r^2 - x^2}}.$$

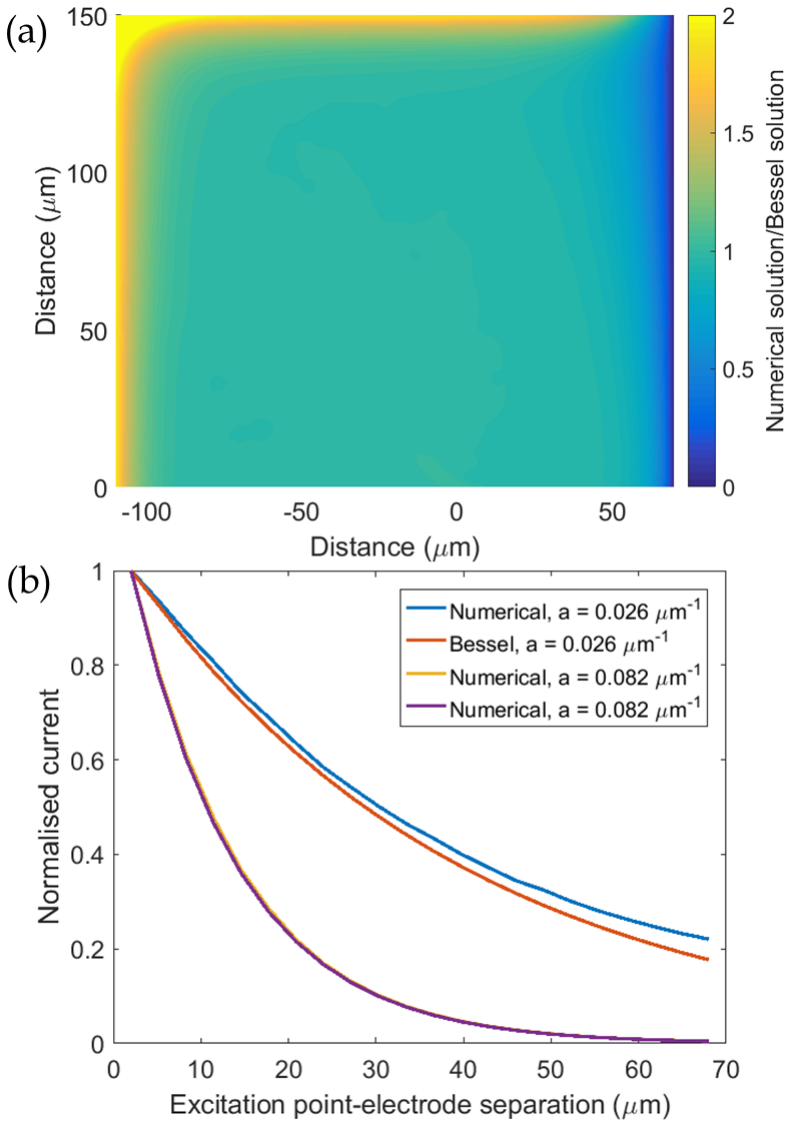

Fig. 3.8 (a): Ratio of the numerical solution to the point excitation problem and the analytic, Bessel function solution. The numerical solution has a 0-concentration condition imposed at x = 70 and a zero-flux, reflective boundary conditions at other borders. The analytical solution has no boundary conditions imposed, but matches the y = 0 reflective boundary by symmetry. Excitation is at the origin. (b): Graph of the total currents going into the electrodes in the numerical and Bessel function solutions as the excitation point is moved away from the electrode. Results are for a=0.026 μm^{-1}, corresponding to bulk monomolecular recombination in our simulation, or $a = 0.082$ μ m^{-1}, corresponding to a very low surface recombination velocity or very tall film (3 cm/s for a 300 nm film). The simulation is conducted in a 100 μm wide, 120 μm long box.

This is integrably singular at $r = x$. Substituting $u = ax$, $y = r/x$, then $w = \sqrt{y^2 - 1}$, we obtain

$$I_1 \propto \int_1^\infty K_0(uy)\, xy \frac{dy}{\sqrt{y^2-1}} \tag{3.11}$$

$$= x \int_0^\infty K_0\left(u\sqrt{w^2+1}\right) dw. \tag{3.12}$$

From page 685 of [56] we may compare this with known integral

$$\int_0^\infty K_\nu\left(m\sqrt{x^2+z^2}\right)\frac{x^{2\mu+1}y}{\sqrt{\left(x^2+z^2\right)^\nu}}dx \tag{3.13}$$

$$=\frac{2^\mu\Gamma(\mu+1)}{m^{\mu+1}z^{\nu-\mu-1}}K_{\nu-\mu-1}(mz). \tag{3.14}$$

Taking $\nu=0, z=1, \mu=-\frac{1}{2}$, we find

$$I_1 \propto \frac{2^{-0.5}\Gamma(0.5)}{u^{0.5}1^{-0.5}}K_{-\frac{1}{2}}(u).$$

Since $\Gamma(0.5)=\sqrt{\pi}$ and $K_{-\frac{1}{2}}(b)=K_{\frac{1}{2}}(b)=\sqrt{\frac{\pi}{2b}}e^{-b}$ (from pages 255 and 444 of [1]),

$$I_1 \propto x\frac{\pi e^{-u}}{2u}=\frac{\pi}{2a}e^{-ax}. \tag{3.15}$$

The end result is we expect to see an exponential decay with length a^{-1}, the diffusion length.

Turning to the fast extraction model, we instead use an estimate of the total current from the current contributions we will demonstrate that we obtain the same current decay pattern, in agreement with numerical integration observed by [57]. However this result may also be proven analytically. As shown in Figure 3.8, the total current as calculated in this way is largely unchanged whether we use the Bessel function solution or the numerical solution. The current is integrated over only the component of the line element orthogonal to the direction of the current, $dl_2 = r\,d\theta$, and $J \propto -\frac{dn}{dr}=\frac{-dK_0(ar)}{dr}=aK_1(ar)$, so this estimate of the current $I_2 \propto \int_x^\infty K_1(ar)\left(\frac{xdr}{\sqrt{r^2-x^2}}\right)$. Substituting for $t=\left(\frac{r}{x}\right)^2$ and $u=ax$, we obtain

$$I_2 \propto \int_1^\infty K_1\left(u\sqrt{t}\right)\left(\frac{dt}{2\sqrt{t}\sqrt{t-1}}\right). \tag{3.16}$$

This may be compared with the known integral

$$\int_1^\infty K_\nu\left(a\sqrt{x}\right)\frac{dx}{\sqrt{x}\sqrt{x-1}}=\left(K_{\nu/2}\left(\frac{a}{2}\right)\right)^2, \tag{3.17}$$

from page 683 of [56]. With $\nu = 1$, using $K_{\frac{1}{2}}(b) = \sqrt{\frac{\pi}{2b}}e^{-b}$ as above, we find

$$I_2 \propto \frac{1}{2}\left(\sqrt{\frac{\pi}{2\alpha}}e^{-\frac{a}{2}}\right)^2 = \frac{\pi}{4a}e^{-ax}, \tag{3.18}$$

and so, comparing with equation (3.15), we see that we obtain an exponential decay with the same exponent.

The prefactor is different in I_1 and I_2 (the extraction velocity in the first case and the diffusion constant divided by the diffusion length in the second) however as this is ignored in the normalised result we have a convenient and robust method of analysing the ratio v/D, irrespective of the physical origin of v. Separating these values may often be accomplished in these models by considering the time delay between excitation and receiving the current.

These results means that in many cylindrically excited situations, we can establish the effective one-dimensional extraction velocity and then current behaviour can be determined analytically. In combination with the findings in the first section, it may be possible to model this extraction using entirely analytical expressions with a high degree of accuracy. Another practical result of this is that, when interpreting current measurements from scanning photocurrent spectroscopy on thin films, we expect the current decay to be monoexponential outside a small radius where generation or second order recombination terms are relevant, and for this result to be independent of the extraction velocity of the electrodes. Interestingly, this solution is identical to the solution of the one-dimensional boundary-free reading of equation (3.5):

$$D\frac{d^2n}{dx^2} - vn = 0 \tag{3.19}$$

$$\Rightarrow \quad n(x) \propto \exp(-ax) \tag{3.20}$$

$$\Rightarrow \quad I_{1D} = qD\frac{dn}{dx} \propto \exp(-ax)\,. \tag{3.21}$$

3.4 Time-dependence of current onset

The above provides us with a solid way of establishing a combined measurement of D and v, but does not disentangle them. However as well as the equilibrium current measurement, scanning current microscopy can investigate the time delay between excitation and current onset, which provides more information about the system. In order to understand how to interpret this delay, we will explore the time-dependent counterpart of equation 3.5.

In the non-steady state case, following the same assumptions, the carrier concentration is governed by the equation

$$\frac{\partial n}{\partial t} = G - R + D\nabla^2 n \,. \tag{3.22}$$

We note that without the generation (G) or recombination/carrier extraction (R) terms and ignoring boundary conditions, this is the diffusion equation in 2D [131], with solution

$$n_0(r,t) = A/(4\pi Dt)\exp(-r^2/(4Dt))\,.$$

This describes a decaying pattern propagating to reach a position r with characteristic timescale $\tau = r^2/4D$. We can then introduce the $R = vn$ term and can write the new solution as proportional to the old, so that $n = n_0(r,t)\chi_R(t)$

$$\Rightarrow \frac{\partial n_0\chi_R}{\partial t} = -vn_0\chi_R + \chi_R D_n \nabla^2 n_0 \tag{3.23}$$

$$= n_0\frac{\partial \chi_R}{\partial t} + \chi_R\frac{\partial n_0}{\partial t}. \tag{3.24}$$

We cancel the last terms on the end of each line, from the definition of n_0 and so find that $\chi_R(r) \propto \exp(-vt)$. This is then the effective Green's function for the source term, G, so if $G = G_0\delta(r)$ after being turned on at time 0 then

$$n = \int_0^t dt' \frac{G_0}{4\pi Dt'}\exp\left(\frac{-r^2}{4Dt'} - vt'\right). \tag{3.25}$$

We note that the linearity of this model means that in a steady state, the effects of reducing G will have the same time-dependence as increasing it. This means that if we continuously excite the system, then stop exciting it, the equilibration time for the excitation onset and cessation are identical. However there are two problems with implementing the solution via integration this way: firstly, the integral in 3.25 is not analytically solvable nor well-behaved numerically; secondly it does not take account of boundary conditions. So, while this can give us some insight into the initial behaviour of the problem, a more useful expression may be obtained by numerical calculation. The solution of equation 3.22 is computed in MATLAB, with a zero-concentration boundary condition imposed at $x = 0$ and zero derivative boundary conditions at all other boundaries ($x = -100$ μm, $y = 0$ or 100 μm). The current density going into the electrode is integrated over the electrode, as in the fast extraction case above. Figure 3.9a shows the time taken for the current to reach 50% of the equilibrium value as a function of distance from the source, and is roughly linear. We also plot the time taken for currents to reach a small value, corresponding to extracting 2% of the charges excited per

unit time. We see that the time for the measured current to reach this value is approximately quadratic, as expected for a diffusing travelling wave to reach a particular position. However, at this time the current itself is rather low, so these values are difficult to measure. The larger fractions, such as the 50% as plotted, is easier to measure but still will suffer from noise in the data. The measure of time most easily and accurately experimentally accessible is the mean time lag that will be detected by a lock-in amplifier, t_{eq}.

We assume that the optical excitation is chopped with a square-wave form. The lock-in amplifier takes a signal proportional to the resulting measured current, modulates it with a function at the chopping frequency and time-averages the response by passing it through a low-pass filter. By also calculating the results with a delayed modulating signal, we obtain both the absolute magnitude of the signal response (as used above), and also a phase delay [92]. This phase delay corresponds to a characteristic equilibration time, t_{eq}. The precise nature of this relation will depend on the modulating function, as discussed in an appendix (chapter 8). Provided the modulation period $2T_P$ is far longer than any characteristic equilibration time, then for any arbitrary time T such that $T_P \gg T \gg t_{eq}$, the value of t_{eq} can be calculated, where we define

$$t_{eq}(x) = T - \frac{\int_0^T I(x,t)dt}{I(x,T)}, \tag{3.26}$$

for I the total current measured at the electrode (we will use the value of I_2 to calculate this numerically). A derivation of this relation and how it can be calculated from the phase delay is given in the appendix, chapter 8.

If the boundary conditions are irrelevant, given the linearity of the problem in G, there are only two relevant constants, D and v. This means we can nondimensionalise (x,t) to $(r\sqrt{v/D}, vt)$. The boundary conditions are still imposed in terms of absolute distance rather than nondimensionalised distance but the effects of this should be minor when the excitation is away from them. We therefore expect to see the dimensionless equilibration time to be a function $vt_{eq} = g(x\sqrt{v/D})$. Figure 3.9 shows that plotting t_{eq}, as calculated from the numerical solutions, against x gives a linear relationship, suggesting $t_{eq} = A(x\sqrt{1/Dv}) + B$ for some A and B. To establish what these are, $t_{eq}(x)$ is calculated for a variety of D and v and the relationship is plotted in figure 3.9b. We find that the end result is well-fitted by a linear relationship with gradient 0.428 ± 0.013.

Conveniently, only the intercept of the linear fit is affected by the common offset errors in x (due to misaligning with the electrode edge) or t_{eq} (from lag in the measurement apparatus) and the intercept is not needed to extract performance metrics. The gradient of the distance-

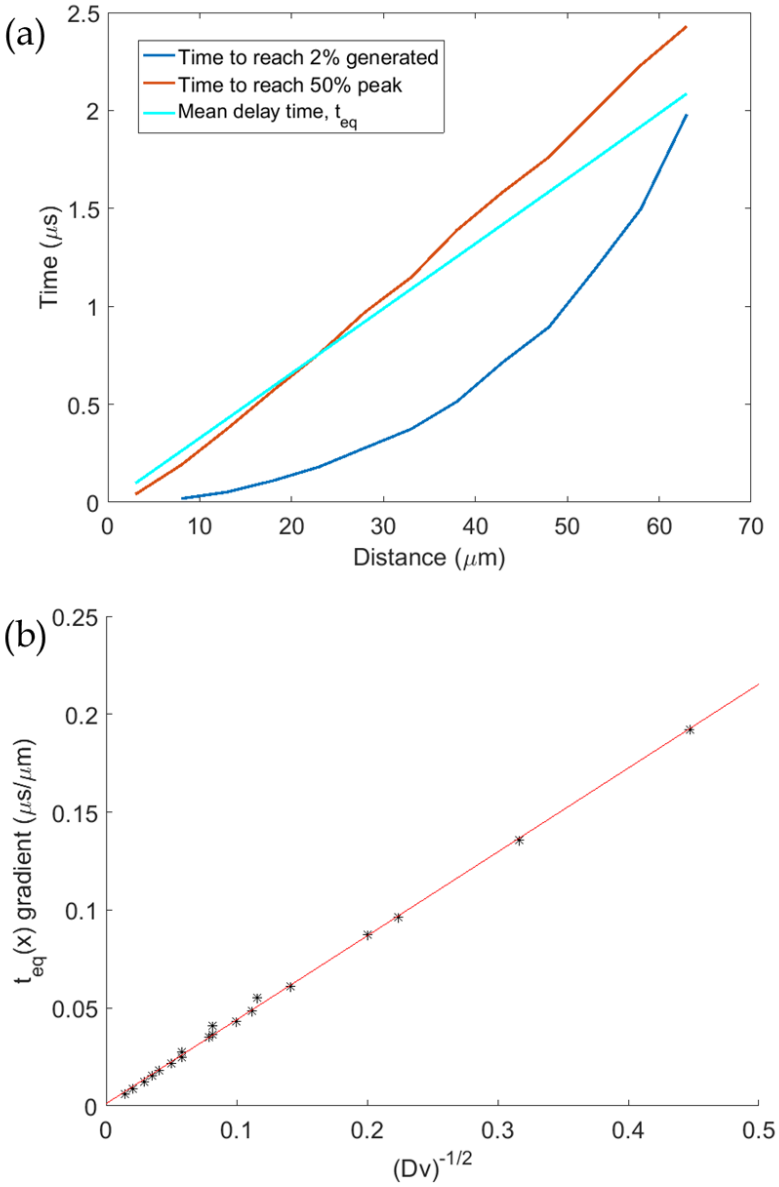

Fig. 3.9 (a): Comparison of the time taken for the current output to reach 50% of the final value, a fixed value equal to 0.2% of the total rate of carrier generation, or t_{eq}, as a function of the distance between excitation point and electrode in the single-variable simulation. Data is from a simulation with $D = 1.5$ cm^2/s, $v = 1$ μs^{-1} (b): The spatial gradient of the equilibration time, dt_{eq}/dx, is plotted as a function of $1\sqrt{Dv}$ for a variety of D and v. As shown in (a), the gradient of t_{eq} is constant for a given set of parameters.

time plot is expected to be $0.43/\sqrt{Dv}$. Between this and the exponential current-time decay proportional to $\sqrt{v/D}$, it is easy to determine both D and v separately.

3.5 Conclusions

In situations featuring large degrees of lateral diffusion, reduced-dimensional modelling or simple analytical expressions will suffice to describe the behaviour of back-contact solar cells or optically excited thin films with laterally displaced electrodes if certain conditions are met. The main conditions are that the system length is long compared to the system width and that fewer than half of the generated charges recombine. In this case it is usually appropriate to neglect the vertical distribution, with an extraction term replacing the vertical surface boundary conditions. If the electrodes extract carriers slowly, this extraction velocity divided by the height is the extraction term. In the fast extraction situation, a more complicated expression for the effective extraction velocity is needed, and it is invalid for very large systems with unequal diffusion constants. Calculating monomolecular recombination levels from one-dimensional and two-dimensional carrier concentrations produces almost identical results in the situations studied here.

This dimension reduction treatment may be implemented on lateral problems exhibiting either one degree of translational symmetry, or on a mixed translational-rotational symmetry problem such as the point illumination of a system with an extended electrode. In the later case, several different commonly-encountered photocurrent microscopy measurements will result in the current recorded exponentially decaying with distance. The exponent factor is the square root of an extraction or recombination rate divided by a diffusion constant, $\sqrt{v/D}$. The time taken for this equilibrium current to be reached will increase linearly with distance, with the gradient being $0.43/\sqrt{Dv}$. Between these two measurements, v and D can therefore be extracted. In photocurrent microscopy measurements, the current equilibrium time can be calculated from the phase delay with a lock-in amplifier. Depending on the placement of the electrodes, the diffusion constant may be that of the electrons, that of the holes, or one in between. If the excitation takes place over one selective electrode, the diffusion constant and extraction rate correspond to the carrier type not extracted. If the excitation takes place in a bulk film, the diffusion constant corresponds to the ambipolar diffusion, a combination of the two diffusion constants, and the decay rate is the recombination rate.

Chapter 4

Modelling the effects of photon recycling on lateral carrier transport in back-contact solar cells

4.1 Introduction

Photon recycling is when a solar cell absorbs a photon to generate free charges, then the free charges recombine to generate another photon which the solar cell also absorbs [39, 10]. This effect is responsible for the high efficiency of gallium arsenide (GaAs) solar cells [164, 106], which are currently the most efficient single-junction solar cells, with power conversion rates of 28.8% under standard conditions [168]. Under some circumstances, idealised GaAs cells could exhibit efficiencies approaching 40% [102]. The advantage of recapturing electron-hole pairs that have recombined is intuitive, and results in lower effective recombination rates than might be expected, however there are effects beyond simply changing the apparent material parameters. These are, firstly, to increase the external photoluminescence (PL) by giving light more chances to be emitted in the escape cone [106, 149], and secondly to redistribute electrons and holes throughout the solar cell.

The first of these factors will be important to consider in the context of the optics and thermodynamics of the whole system, however the second will manifest itself directly in measurements of diffusion within the system. There are several different models of the impact of light-based transport on the effective diffusion of carriers in solar cells, with different regimes of applicability.

The first model, due to Dumke [39], posits only one carrier of interest radiatively recombining with a reservoir of countercharges with a monomolecular rate constant. By

considering a Taylor expansion of a one-dimensional carrier density change, he calculates a light flux that results in a contribution to the effective particle diffusion constant:

$$D_{optic} = \frac{1}{3\tau_R} \int \frac{P(E)}{(\alpha(E))^2} \, dE, \tag{4.1}$$

for τ_R the radiative recombination rate, $P(E)$ the normalised emission spectrum, the energy, E and α the absorption coefficient at that energy, to be capped at the reciprocal of the sample dimensions due to the derivation involving a Taylor expansion and integration of length to infinity. This contribution can simply be added to the diffusion constant of the whole system, so this model will be referred to as the 'assisted diffusion model'. Badescu and Landsberg [9] derive the same result, with a variable numerical prefactor in the case of systems with one finite dimension.

Later models allowed for light generated by bimolecular recombination processes. These include one-dimensional numerical solutions to the drift-diffusion equations with a numerical photon recycling term included [122, 40, 10], and also an analytical 1D drift-diffusion model [99]. All of these models assume the direct propagation of light from point of origin to point of absorption, although a few allow for reflections from the top and bottom surfaces. Because light is assumed to travel unscattered in lines, they will be referred to as 'directional radiation models' in this paper. However, Yablonovitch argues [167] that imperfections or roughness in the film will result in randomisation of the direction light is travelling in upon a few reflections. With films a few hundred nanometers and internal emission at wavelengths that can travel microns, this is an important effect. For systems with more than one dimension, it is not clear that any of the direct light-propagation techniques of the one-dimensional approaches can be easily generalised to include scattering.

An alternative approach to modelling light propagation involves photon diffusion, a model previously applied in highly-scattering media like biological tissue [38], atmospheres [21] and astronomy [107], and follows logically from assumptions of the photon gas model in solar cells, which is often used in thermodynamic assessments of solar cells [139, 127, 101] but not in nanoscopically detailed models. This model assumes photons have their direction of travel frequently randomised, and so make a random walk, or diffuse.

The nature of the photon diffusion constant is agreed to be of the form

$$D_{ph} = \frac{c_m}{3((1-g)\alpha_s + b\alpha)} \tag{4.2}$$

where c_m is the speed of light in the medium, α_s the inverse scattering length, b a constant and g the average value of the cosine of the angle between the incoming and scattered light

(the medium is assumed to be isotropic). This makes $(1-g)\alpha_s$ the inverse of the light randomisation distance, the lengthscale over which the light 'forgets which way it was going'. If the scattered direction is independent of the incoming direction, g is zero.

The specific value of b is highly debated [38]. Simplistically, the denominator of equation (4.2) is the average distance light travels each step, so $b = 1$. However, different in-depth derivations disagree, with some questioning whether D_{ph} should be dependent on the absorption constant at all (i.e. $b = 0$) [51, 41]. Since absorption is not a redistributive effect, how rapidly it happens should not affect the random walk up until that point: does the total length of the random walk affect the diffusion constant? More recently, theorists have argued that it does, but suggest that a universally applicable expression is not possible. Simulations and analytical results in different circumstances suggest values should fall between $b = 0.1 - 0.5$, with the most common values in the range around $b = 1/3$ to $1/5$ [55, 4, 42], with the understanding that different situations will require different values of b. For instance, if one wishes to model the propagation of wavefronts, a value of $b = 1/3$ is required to make the wavefront propagate at the correct speed [42], whereas for time-independent results, matching correct results depends on the degree of scattering anisotropy [4]. The models are explicitly developed on the assumption that scattering is dominant, and also should not be used for time-dependent scattering if fewer than 10 scattering events are likely to have happened [171], as directional propagation or 'ballistic transport' is significant.

All of the derivations of photon diffusion are for systems where light is not generated in the scattering/absorbing layer; in the event that light is absorbed and then re-emitted at the same wavelength, it is effectively just scattered. However if there is a wavelength shift in the absorbed light, or low emission efficiency, more care is needed.

Here, we will compare the three approaches to modelling the behaviour of the system: assisted carrier diffusion, coherent, directional radiation and photon diffusion. We will apply these to a one-dimensional system with radial symmetry to model the spread of charge from a point illumination. The results of this simulation can be compared with an experiment on a photon recycling perovskite solar cell [123]. This experiment involves the focused illumination of a perovskite thin film deposited on glass and monitoring the current extracted from electrodes away from the illumination point as the illumination point moves. This perovskite system was investigated because of the curiously long-ranged current extraction, indicative of photon recycling, however the process is not well-understood in perovskites. This work continues previous research demonstrating the presence of photon recycling in perovskites and develops more involved numerical frameworks for investigating it.

In order to properly model the outcoupling of light and the manner of propagation of coherent modes, we will first construct an optical model of the thin film/substrate system.

How light is outcoupled is important in all models, and if the light is assumed to scatter rarely, the modal nature of the light propagation will also be important. We will then develop mathematically the three models of photon recycling and incorporate them into drift-diffusion models of the perovskite film.

4.2 Experimental investigation

As reported elsewhere [123], back-contact methyl ammonium lead iodide perovskite solar cells were fabricated by Luis Pazos-Outón to study the behaviour of a photon-recycling system. Electrodes were fabricated by photolithographically etching 8 μm-wide connected fingers in an ITO layer on a glass substrate. Electron or hole selective layers of TiO_2 or PEDOT were then deposited on alternating electrodes by electrodeposition, and a strip without any electrodes on it runs along the edge of the system.

A 1:3 molar ratio of $PbAc_2$ and CH_3NH_3I was prepared in N,N-dimethylformamide solvent and films were made by spincoating this solution onto the etched ITO glass slides.

Combined photocurrent (PC) and photoluminescence (PL) measurements were taken by Monika Szumilo using a *WITec alpha300 S* scanning near-field optical microscope. This uses a 405 nm laser with a full-width half maximum of 3 μm to excite the sample at a point. The intensity of the laser is of the order 10μW, although the precise energy incoupled from the laser is hard to establish, as it depends on the focus and on reflection from the sample. The fraction of internal light we expect to be absorbed in one pass is 0.66, using the absorption constants discussed below. The full-width half-maximum of the laser peak is 3 μm, so we will model the incoming light distribution as a Gaussian with a decay period of half of this. Measurements of the photocurrent are made as the excitation point moves away from the electrodes into the film. We expect the PL to depend on the square of the carrier density, n, although at longer wavelengths PL can travel several μm from its source. However around the emission peak (760-780 nm) the PL should travel less than a μm. This means that we expect $n \propto \sqrt{PL}$. Since PC $\propto \int n\,dl$ over the electrode at position x, we expect PC $\approx \int_{-\infty}^{\infty} \sqrt{PL}\,dl$. To allow the integration to infinity, we fit a biexponential distribution to the PL and integrate that analytically.

A wide range of diffusion constants are reported in the literature, ranging from < 0.1 cm^2/s [137, 150] to > 2.5 cm^2/s [37, 144] depending on processing conditions and estimate techniques. As we will be investigating a trend that might be explicable with unusually long diffusion, we will chose a high estimate of the diffusion constant, $D = 1.5$ cm^2/s, even though the single-crystal manufacturing methods normally required to obtain such high values were not used.

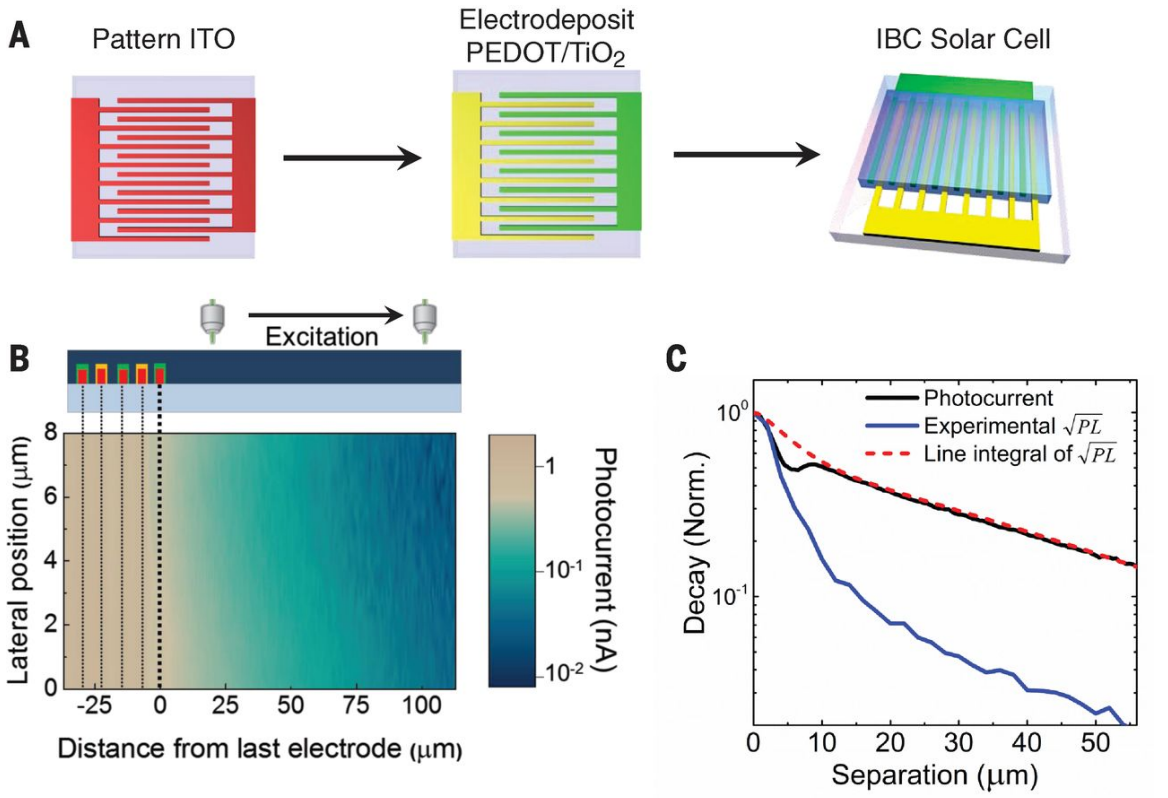

Fig. 4.1 (A): Fabrication of the IBC device. First, (left) pattern a flat sheet of ITO, then (middle) electrodeposit TiO2 on half of the "fingers" and PEDOT on the other half, and then (right) spin-coat the photoactive perovskite layer. (B): Photocurrent map at the edge of the active area of an IBC perovskite device. The lateral position is along the electrode direction. We observed photocurrent several tens of micrometers beyond the last electrode (x-axis position 0 μm, bold dashed line). (C) Comparison between normalized spatial decay of the photocurrent and square root of PL between 760-780 nm. This component of the PL should correlate to the square of the carrier density there, hence the finding that $\sqrt{PL}$ integrated over a line is approximately equal to the photocurrent. These results suggest that photon densities, which propagate over large distances through the material assisted by photon recycling, can be extracted as photocurrent. Image taken from [123].

Photothermal deflection spectroscopy (PDS) measurements were also made by Mojtaba Abdi-Jalebi to give the absorption of the system over wavelengths of interest. The PL spectrum and absorption spectrum can be directly calculated from each other via the Van Roosbroeck-Shockley relation [160].

Time-dependent PL measurements by Johannes Richter tracked the changes in carrier population over time, and were used to fit the recombination constants, $A = 10^6$ s^{-1} and $B_{ext} = 10^{-16}$ m^{3}s^{-1}. It is known that these values differ widely between samples and preparation techniques.

4.3 Computational investigations

4.3.1 Optical modelling

Optical modelling methods

We must first consider the means by which light travels in this film; in the one-dimensional bulk cases above, few reflections were expected and incoherence could usually be assumed, however if significant lateral transport is expected in a thin film, the nature of the travelling modes of light may play an influence.

To assess the effects of interference on outcoupling, we construct a cylindrical two-dimensional wave interference model based on the work of Benisty [13], where the electric field excited by a dipole in a thin film is propagated using a transfer matrix approach [108, 76]. This involves the forwards and backwards-going electric field wave amplitudes ($E_{i\uparrow}, E_{i\downarrow}$) at either side of a thin film layer i through a phase matrix, $\mathbf{U_i}$. At the interface, the field amplitudes are related via the polarisation-dependent refractive matrix, $\mathbf{W_{i-1,i}}$. These are typically expressed in terms of incident angle, θ, however to include the potential treatment of evanescent waves with imaginary propagating angle, we express the matrices in terms of radial and vertical wavevector, k_r and k_z, which must add in quadrature to $k = 2\pi n_i/\lambda$ in each layer, for λ the free-space wavelength. k_r is conserved between layers but may exceed k in some layers. We then express Fresnel's equations in terms of these variables. It is worth noting that there is some controversy over the solution of Fresnel's equations, with Maezawa and others [100, 166] suggesting that the form found in many textbooks [15, 49] are not appropriate for use with absorbing media, where they will give a discontinuity in energy flow (or Poynting) vector at the interface. However, the standard coefficients used with the full expression for the Poynting vector for plane waves that allows for interference between incident and reflected waves [166, 32] overcomes this problem, and the Poynting vector, $\mathbf{S}$ is conserved in our model, except where energy is introduced at the source layer.

Reinterpreting the standard Fresnel results [15, 49] in terms of wavevectors gives the reflection and transmission components for TE polarised and TM polarised light in nonabsorbing media as

$$r_{1,2}^{TM} = \frac{k_{z2}n_1^2 - k_{z1}n_2^2}{k_{z2}n_1^2 + k_{z1}n_2^2},\ t_{1,2}^{TM} = \frac{2k_{z1}n_2n_1}{k_{z2}n_1^2 + k_{z1}n_2^2},\ r_{1,2}^{TE} = \frac{k_{z1} - k_{z2}}{k_{z1} + k_{z2}},\ t_{1,2}^{TE} = \frac{2k_{z1}}{k_{z1} + k_{z2}}, \qquad (4.3)$$

We may then define the phase and refractive matrices as [108, 13]

$$\mathbf{U_i} = \begin{pmatrix} \exp(-ik_{zi}L_i) & 0 \\ 0 & \exp(ik_{zi}L_i) \end{pmatrix}, \mathbf{W_{i-1,i}} = \frac{1}{t_{i-1,i}} \begin{pmatrix} 1 & -r_{i,i-1} \\ r_{i-1,i} & t_{i,i-1}t_{i-1,i} - r_{i,i-1}r_{i-1,i} \end{pmatrix}, \tag{4.4}$$

for L_i the thickness of the ith layer. Field intensities after passing through several layers are then given by

$$\begin{pmatrix} E_{i\uparrow} \\ E_{i\downarrow} \end{pmatrix} = \mathbf{W_{i,i+1}U_{i+1}W_{i+1,i+2}U_{i+2}...W_{j-1,j}} \begin{pmatrix} E'_{j\uparrow} \\ E'_{j\downarrow} \end{pmatrix} \equiv \mathbf{S_{i,j}} \begin{pmatrix} E'_{j\uparrow} \\ E'_{j\downarrow} \end{pmatrix}, \tag{4.5}$$

where the prime represents taking the values immediately after the interface. The $\mathbf{S_{i,j}}$ matrix gives us the overall reflection and transmission from the stack; by comparison with refractive matrix in equation (4.4), we see that the (1,1) element of $\mathbf{S_{i,j}}$ is $1/t_{i,j}$ and the (2,1) element is $r_{i,j}/t_{i,j}$. To add the effects of an infinitesimally thick dipole layer at position s, we introduce a discontinuity in the electric fields on either side of the layer. We define

$$\begin{pmatrix} A_\uparrow \\ A_\downarrow \end{pmatrix} = \begin{pmatrix} E'_{s\uparrow} \\ E'_{s\downarrow} \end{pmatrix} - \begin{pmatrix} E_{s\uparrow} \\ E_{s\downarrow} \end{pmatrix}, \tag{4.6}$$

for the polarisation and dipole-orientation dependent $A_{\downarrow,\uparrow}$, with values as shown in table 4.1. This represents the different components of the spherical waves excited by the dipole - in principle, the range of k_z should extend to infinity, although no power is radiated by most of these modes. As in previous work [47, 115, 75], the refractive index of the active layer is assumed to be purely real in calculating the values of A to give real angles of emission. If no light is externally incident, we can express the light exiting the cell from the right and left side using the matrices

$$\begin{pmatrix} E'_{s\uparrow} \\ E'_{s\downarrow} \end{pmatrix} = \mathbf{S_{s,e}} \begin{pmatrix} E'_{e\uparrow} \\ 0 \end{pmatrix} \equiv \mathbf{b} \begin{pmatrix} E'_{e\uparrow} \\ 0 \end{pmatrix}, \begin{pmatrix} E_{s\uparrow} \\ E_{s\downarrow} \end{pmatrix} = (\mathbf{S_{0,s}})^{-1} \begin{pmatrix} 0 \\ E_{0\uparrow} \end{pmatrix} \equiv \mathbf{a} \begin{pmatrix} 0 \\ E_{0\uparrow} \end{pmatrix}. \tag{4.7}$$

By comparison with the single-interface refractive matrix (see equation (4.4), [108]), we can consider the reflection and transmission from all layers after the source are $r_b = b_{2,1}/b_{1,1}, t_b = 1/b_{1,1}$ as normal. However, on the left side of the source, the 'forwards' direction is reversed, so $r_a = a_{1,2}/a_{2,2}, t_a = 1/a_{2,2}$.

	Mode	
Dipole	TE	TM
Horizontal	$A^{(h),s}_{\downarrow,\uparrow} = \pm\sqrt{\frac{3}{16\pi}}$	$A^{(h),p}_{\downarrow,\uparrow} = \pm\sqrt{\frac{3}{16\pi}}\cos\theta_1 = \pm\sqrt{\frac{3}{16\pi}}\frac{k_{z,1}}{k_1}$
Vertical	$A^{(v),p}_{\downarrow,\uparrow} = 0$	$A^{(v),p}_{\downarrow,\uparrow} = \sqrt{\frac{3}{8\pi}}\sin\theta_1 = \sqrt{\frac{3}{8\pi}}\frac{k_\parallel}{k_1}$

Table 4.1 Normalised source terms for different polarisations and orientations of dipoles. Reproduced from [13].

Since there is no externally incident light, $E'_{s\downarrow} = E'_{s\uparrow} r_b$ and $E_{s\uparrow} = E_{s\downarrow} r_a$. Combining these with equation (4.6), we obtain the relations

$$\begin{pmatrix} E_{s\uparrow} \\ E_{s\downarrow} \end{pmatrix} = \frac{A_\downarrow - r_b A_\uparrow}{r_a r_b - 1}\begin{pmatrix} r_a \\ 1 \end{pmatrix}, \quad \begin{pmatrix} E'_{s\uparrow} \\ E'_{s\downarrow} \end{pmatrix} = \frac{r_a A_\downarrow - A_\uparrow}{r_a r_b - 1}\begin{pmatrix} 1 \\ r_b \end{pmatrix} \tag{4.8}$$

$$\Rightarrow E_0 = \frac{A_\downarrow - r_b A_\uparrow}{r_a r_b - 1} t_a,\ E_e = \frac{r_a A_\downarrow - A_\uparrow}{r_a r_b - 1} t_b. \tag{4.9}$$

Note that the lack of t in (4.8) means that it is appropriate for use even when no E-field escapes the device. In the event that no light is transmitted beyond a certain layer, the calculation of the **a** and **b** matrices may be truncated at this point. Singularities in the **W** matrix arising from $t = 0$ will cancel and be irrelevant when finding the reflections.

If there is power exiting from either side, we can calculate the outflux of power,

$$P_{out} = \int d\Omega \mathbf{S_{out}} = \int d\Omega\, |E_{out}|^2 \frac{n k_{ze}^2}{n_s k_{zs}^2} = \int_0^{k_c} \frac{2\pi k_r dk_r}{\sqrt{k^2 - k_r^2}} |E_{out}|^2 \frac{n k_{ze}^2}{n_s k_{zs}^2}, \tag{4.10}$$

where k_c is the highest value of k_r that gives a purely real (external) k_{ze}, equal to k if $n = 1$. Assuming the perovskite is isotropic, we can decompose randomly oriented dipoles to have equal components in the three principle axes, the horizontal two being identical for our purposes. This results in twice as much power radiated by horizontal dipoles as by vertical. Different dipole orientations and polarisation modes behave independently, and the total energy radiated through top and bottom interfaces should be calculated independently and summed. We input the film thickness of 100 nm for the perovskite, measured by

Mojtaba Abdi-Jalebi using a Vecco Dektak profilometer, and the ellipsometrically determined, wavelength-dependent refractive index from literature values [96]. We can then calculate power emitted and the intensity at which light travels internally for a range of wavelengths and then integrate over the PL spectrum of the perovskite. Internal power emission must be calculated using the full Poynting vector that allows interference between forwards and backwards propagating terms [24]. For the different polarisations, this is:

$$\mathbf{S}^{TE} \propto \Re\left(\hat{\mathbf{r}}|E_{\uparrow}+E_{\downarrow}|^2 n\sin\theta + \hat{\mathbf{z}}(E_{\uparrow}^{*}+E_{\downarrow}^{*})(E_{\uparrow}-E_{\downarrow})n\cos\theta\right) \tag{4.11}$$

$$\mathbf{S}^{TM} \propto \Re\left(\hat{\mathbf{r}}|E_{\uparrow}+E_{\downarrow}|^2 n(\sin\theta)^{*} + \hat{\mathbf{z}}(E_{\uparrow}+E_{\downarrow})(E_{\uparrow}^{*}-E_{\downarrow}^{*})n(\cos\theta)^{*}\right). \tag{4.12}$$

Using these expressions, we can find the principle travelling modes as the θ values that make the largest contributions to the $\hat{\mathbf{r}}$-directional power flow.

Optical modelling results

We then apply this model to our experimental situation, a MAPbI perovskite layer on glass, with air on either side. Figure 4.2a shows the change in extracted power upon changes in thickness of the glass layer. Although our method does not formally impose incoherence resulting from the thickness and width variability in the glass layer, the effect of varying the thickness results in smaller proportional changes in power emissions at larger heights, finally settling on variations of less than 1% of the total value when the thickness of the glass is comparable to 1 mm, as small proportional changes in height make little difference to the result. In order to numerically resolve the separate oscillations and therefore correctly average over them, it is best practice to limit the glass thickness to 10 000 nm in other simulations.

In Figure 4.2b the power extracted from the top and bottom of the system is plotted when the height of the source layer is moved through the active layer. The emission efficiency varies by around 10% when the position of the emitter changes. These interference effects are clearly measureable, but not particularly large. It is interesting that there is destructive interference that peaks close to the middle of the device, reducing the outcoupling of light and meaning that the vertically averaged light extraction efficiency is the same as the extraction efficiency from the average vertical position (i.e. the light out from the middle). However, in order to simplify later one-dimensional models, we will neglect this difference and assume the source is always central, at 50 nm.

In order to calculate the total proportion of light that leaves the system, the power extraction was calculated as a function of wavelength in Figure 4.2c. Integrating this wavelength dependence over the emission spectrum of the perovskite, we calculate 5.0%

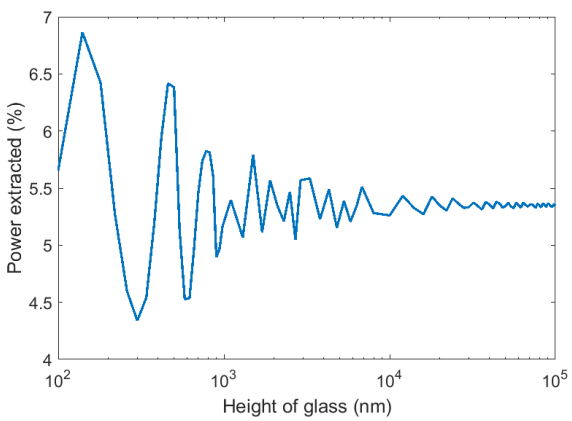

(a)

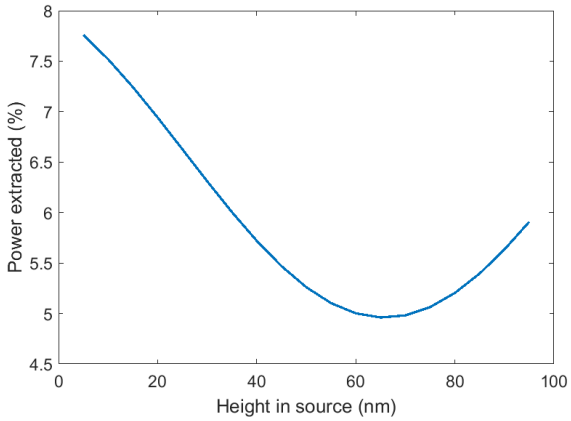

(b)

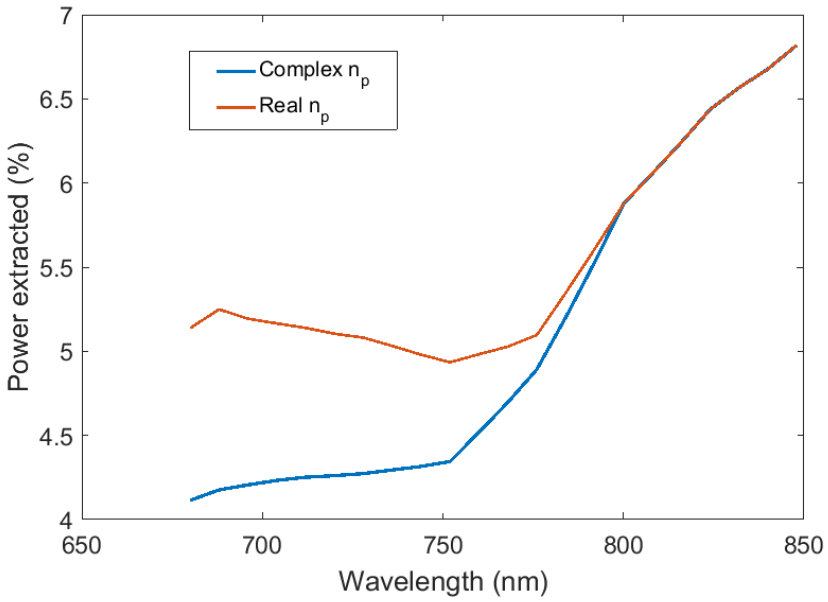

(c)

Fig. 4.2 Optical power emission from the perovskite layer of our air/perovskite/glass/air slab. (a): Varying the thickness of the glass layer and plotting the emission of 785 nm light from the center of the source (50 nm into the 100 nm source). (b): Moving the position of the source dipole layer through the 100 nm perovskite layer for 785 nm light and 100 000 nm thick glass. (c): Varying the wavelength for emission from the center of the perovskite with either real or complex refractive index (other figures feature only complex n_p). Glass thickness is 1000 nm.

power emission if the perovskite layer's self-absorption is considered. If the refractive index is purely real the emission slightly increases to 5.3%.

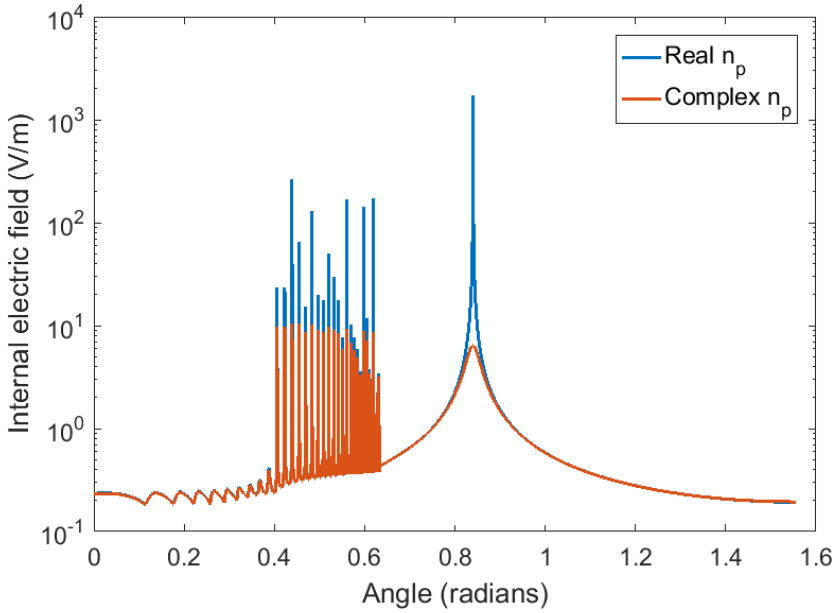

(a)

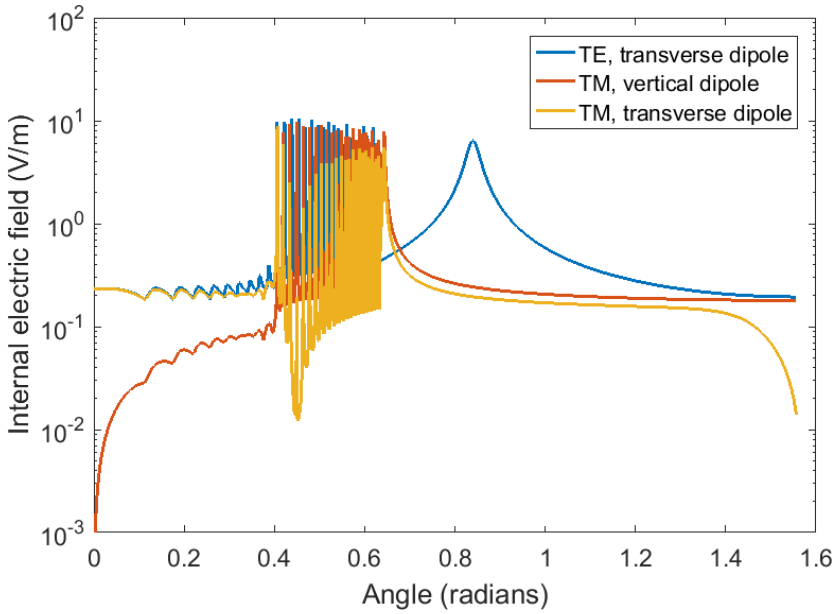

(b)

Fig. 4.3 Internal electric field strength from dipoles in the center of the perovskite layer at a wavelength of 785 nm. Glass thickness is 10 000 nm. (a): Comparing perovskites with only real refractive index with complex refractive index, for TE radiation from a transverse dipole. (b): Comparing fields resulting from different polarisations and orientations of dipoles. No TE radiation can emerge from vertical dipoles.

The interference conditions mean that most of the nonemitted power is concentrated into modes inside the perovskite. If the radiation wavelength is not absorbed at all, this can result in an infinitely strong electric field intensity at the mode peak, where resonance happens. Figure 4.3a compares the electric field resulting from emission inside absorbing and nonabsorbing perovskite layers. Absorption reduces the peak height, though does not significantly change the peak location. Figure 4.3b compares the field when considering different polarisations. In terms of power flow, the factor of interest is the solid-angle-weighted Poynting vector. In Figure 4.4a, we find the sum of radially-directed power flow emitted up to different angles, calculated by taking the radial Poynting vector at the source using equations 4.11 and 4.12 and integrating over solid angles up to a limiting angle. The rate of increase in this is the power radiated at that angle. The step shape in the dominant TE curve shows that most of the radial power is radiated in a small range of angles. The largest increase in the power flow occurs at in the TE spectrum an angle of 0.8 radians and corresponds to the majority of the total radially-directed power. As this represents the most significant mode, we will assume that all power generated at this wavelength is transported at this angle. The specific angle will be the modal angle of the mode, θ_m, defined by $\int_0^{\theta_m} \mathbf{S}_r d\Omega = \frac{1}{2}\int_0^{\pi} \mathbf{S}_r d\Omega$. We will therefore model the fraction of coherently propagating light as having this angle. For a point-source with complex refractive index, we should include the imaginary component of k_r given by this angle.

To check the code's results we may also compare it with results from the open-source Moosh project [32], designed to model the properties of thin film stacks under external illumination. The source-free stack transmission and absorption terms are identical, as expected. We also check the self-consistency of our code, requiring that in the case of neglegibly small refractive index mismatch, all light leaves the cell and energy is conserved. The Moosh code also allows us to calculate travelling waves resulting from external illumination, which we expect to be similar to those arising from internal illumination. These are compared in Figure 4.5, showing high similarity. The means of determining the precise angle differs between the measurements - the Moosh code calculates only the dominant mode, whereas our treatment considers all transport and looks for the median power emission angle. This means we cannot confidently assign the whole of the difference to an internal/external illumination divide, but a large difference would be cause for concern.

4.3.2 Directional radiation model

We can now apply this finding to the original problem of photon recycling in a laterally extended solar cell. We will start off with the equations for isotropic bulk transport and then include photonic behaviour in order to model a point-illuminated sample.

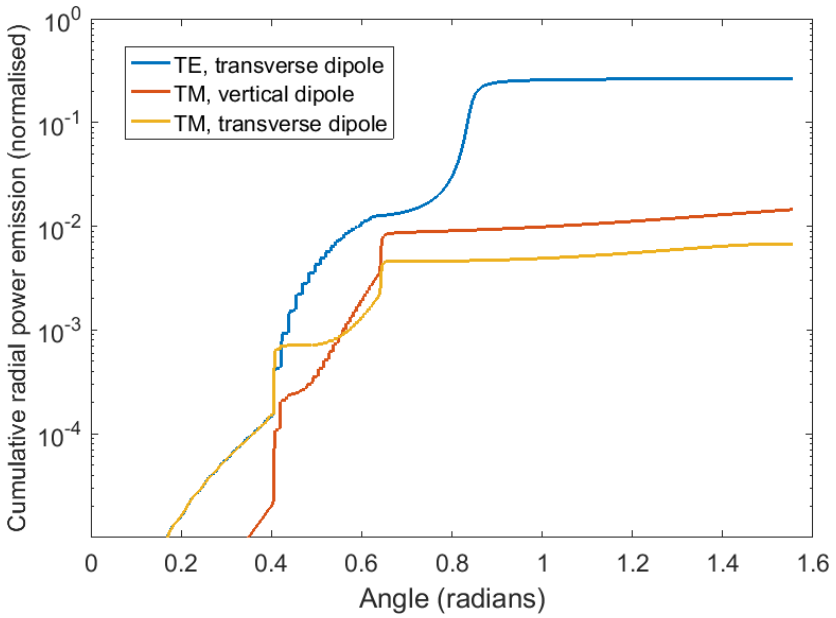

(a)

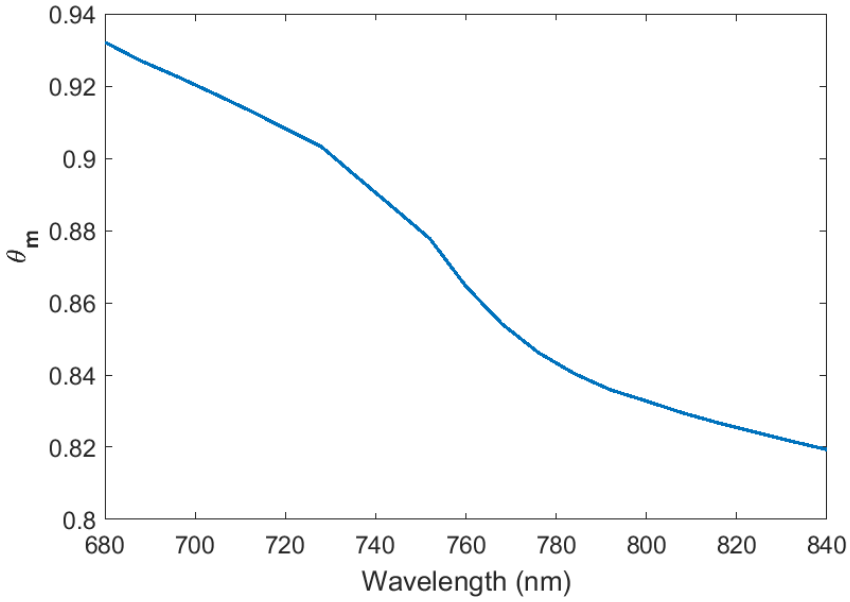

(b)

Fig. 4.4 (a): Solid-angle integral of the radially-directed Poynting vector as a function of angle. (b): the modal angle of radial power radiation as a function of the wavelength at which it is emitted. All simulations for dipoles in the center of the perovskite layer at a wavelength of 785 nm. Glass thickness is 10 000 nm.

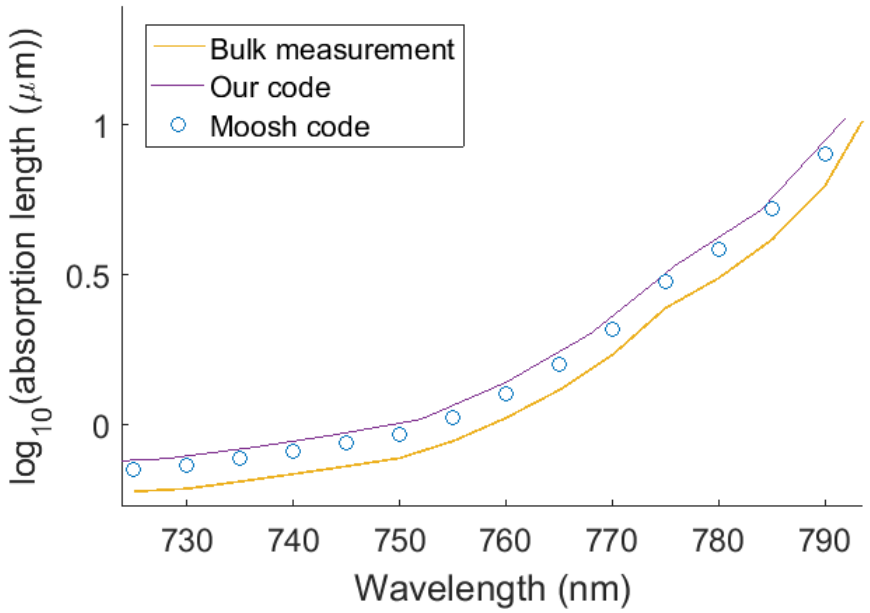

Fig. 4.5 Comparison of the simulated absorption length of modes travelling in an air/perovskite/glass stack using either our code with internally generated light, Moosh code for externally incident light or the ellipsometrically measured absorption spectrum of the bulk perovskite.

If we expect the light of the system not to be scattered frequently, then we should use a directional radiation model for the photon recycling generation term. We will express it in cylindrical co-ordinates, so the photon recycling generation rate, G_{ph}, at a point $\mathbf{r} = (r, \phi = 0, z)$, is given by integrating the light received from all other points, (r', ϕ', z'). The light which reaches $\mathbf{r}$ is given by the decaying spherical wave intensity as a function of the distance between the emission and absorption of light, $\rho = \sqrt{r'^2 + r^2 - 2r'r\cos\phi' + (z-z')^2}$. The intensity of the wave reaching $\mathbf{r}$ is multiplied by how strongly light is generated at $\mathbf{r}'$. Based on [84, 40] therefore we have

$$G_{ph}(\mathbf{r}, n, p) = \int_{E=0}^{\infty} \alpha(E) P(E) \int_{z'=0}^{L} \int_{\phi'=0}^{2\pi} \int_{r'=0}^{\infty} B \cdot \left(n(r', \phi', z')\, p(r', \phi', z') - n_i^2 \right) \frac{\exp\left(-\alpha(E)\rho\right)}{4\pi\rho^2} r' dr' dz' d\phi' dE, \quad (4.13)$$

where B is the bimolecular recombination coefficient (assumed to be responsible for all the PL) and L the height of the active layer. This model is constructed assuming that the photoluminescence spectrum will be constant over the system, which is usually a good

assumption for low carrier concentrations, although fails for systems when band-filling becomes relevant.

In a point-illuminated thin film, we may assume diffusion quickly equalises the vertical distribution of carriers. We may therefore make equation (4.13) two-dimensional, neglecting any z-dependence as the film height is small compared to the lateral dimensions. The reflections from the upper and lower surfaces will result in coherent, modal transport in the emitted light, so we use the modal values of α (the inverse of the absorption length, as plotted in Figure 4.5) and replace the z integral over a spherical wave with a cylindrical wave. To account for non-reflected light, we multiply the generation term by P_s, the probability that re-emitted radiation will remain in the system. In a simplified, non-modal model, this would be the probability of light being emitted into the escape cone. We can now apply this model to our point-illuminated film. Assuming cylindrical symmetry about the excitation point at the origin, we can also perform the ϕ' integral and E integral separately before carrier concentrations are known, leaving a purely radial carrier-dependent model. The resulting internal generation term can then be expressed as

$$G_{ph}(r,n,p) = \int_0^\infty dr'\, G_{phR}(r,r') P_s B \left(n(r')\, p(r') - n_i^2\right) , \tag{4.14}$$

where we have defined the function

$$G_{phR}(r,r') = \int_0^\infty dE\, \alpha(E) P(E) \int_0^{2\pi} d\phi' \frac{r' \exp\left(-\alpha(E)\sqrt{r'^2 + r^2 - 2r'r\cos\phi'}\right)}{2\pi\sqrt{r'^2 + r^2 - 2r'r\cos\phi'}}. \tag{4.15}$$

We wish to study how this equation should be applied to the point-illumination of a perovskite thin film, where we must also allow the carriers to diffuse laterally. In principle the electrons and holes should be treated separately and the electric field distribution should also be calculated, however if there is no nearby carrier extraction at an electrode or applied electric field, we expect the space-charge electric field to bind together the populations of the two carriers [140]. The electrostatic attraction between the electrons and holes ensures that the faster species is pulled back and the slower is pulled forwards. This attractive effect will force the distributions of the carriers to be (almost) identical, with a diffusion constant somewhere in between that of electrons and holes. As the distributions are almost identical, there is no net space charge so the macroscopically observed electric field is neglegible. As a result, in our experiment we expect to see ambipolar diffusion [113], where there is only one relevant diffusion constant, and no electric field. This means we can reduce the drift-diffusion

equations to one diffusion equation

$$\frac{dn(r)}{dt} = G(n,r) - R(n) + D_a \nabla^2 n(r), \tag{4.16}$$

where $G(n,r)$ is the total generation, $R(n)$ the recombination and D_a the ambipolar diffusion constant. We apply both monomolecular and bimolecular recombination, $R = An + Bn^2$, with $A = 1$ /μm and $B = 10^{-16}$ m^{3}s^{-1}, as mentioned in the experimental section above. The spectroscopic recombination constants measure the change in carrier number, so only count radiative recombination that does not result in subsequent charge generation, therefore the externally observed $B_{ext} = B(1 - P_s)$. Using the light escape probability $(1 - P_s)$ =5% and the measured $B_{ext} = 10^{-16}$ m^{3}s^{-1} we obtain $B = 2 \times 10^{-15}$ m^{3}s^{-1}. We may compare this model to the non-recycling model, where we use $B_{ext} = B$ but do not add G_{ph} to G.

A program was written to evaluate equation (4.15) numerically to construct a source term matrix, then apply equation (4.14) in addition to a central Gaussian source term (the external illumination) to solve this rotationally symmetric diffusion equation. We impose reflective boundary conditions (zero current) on both the outer ($r = 600$ μm) and inner ($r = 0$ μm) surfaces. The program then solves this partial differential equation to find the steady-state carrier density. We can derive the PL from this (proportional to the square of the carrier concentration) and the current - this is given by the line integral of the carrier concentration over the electrode at position x away from the origin. Numerically, we implement this as

$$I(x) \propto \int_x^\infty n(x) dl \approx \sum_{r_i \geq x} n(r_i) \left(\sqrt{r_{i+1}^2 - x^2} - \sqrt{r_i^2 - x^2} \right), \tag{4.17}$$

where r_i is the radial value of the ith lattice site. This model ignores the effects that the electrodes have on the carrier distribution. The effects of truncating and discretising the mesh, however, can be investigated as we expect the non-recycling version of the model to give a zeroth-order modified Bessel function of the second kind, $K_0(\sqrt{A/D_a}\,x)$, provided that generation and bimolecular recombination terms can both be neglected as detailed in the previous chapter.

The results of these calculations give the plots in Figure 4.6a. We can compare these results to the experimental PC and PL, as seen in Figures 4.6b and c. When comparing to the PL, we choose the component of light emitted between 760-780 nm, the emission peak of the PL. It is strongly absorbed, so cannot travel far within the film and therefore indicates the locally generated PL, whereas much redder PL can travel long distances before being scattered out of the film. We take PC data from at least 10 μm away from the electrode so that any affects arising from the electrode itself and any non-Gaussian aspect of the illumination

can be neglected. The PL was measured away from the electrodes, so data is used from 4 μm away from the origin.

Unfortunately, while Figure 4.6c shows fair correspondence between the recycling model and the data, 4.6b shows only order-of-magnitude agreement. While both show that including photon recycling makes the model closer to the data, and the long-term current trend in Figure 4.6c is fairly accurate, the results do not confirm the validity of this particular model. This could be due to a miscalculation in any of the input values, or a breakdown of the assumptions of the model. We will therefore compare this to other models.

4.3.3 Assisted diffusion model

An alternative, simpler version of this model, due to Dumke [39], is augmenting the carrier diffusion parameter. This model assumes no scattering, so in our two-dimensional assisted diffusion model we should also use the modally-adjusted α term to implement equation (4.1). We also require a constant value of τ_R, which is unfortunate as in the true situation we expect the radiative recombination to be second order in the carrier concentration and therefore variable, with $\tau_R = (k_2 n)^{-1}$ in the symmetric carrier behaviour case. However if we use the monomolecular decay rate instead, we can evaluate equation (4.1) to give

$$D_{optic} = \frac{k_1}{3} \int \frac{P(E) P_s}{(\alpha(E) \sin \theta_m)^2} \, dE \,, \tag{4.18}$$

where we have corrected the bulk value of α to $\alpha(E) \sin \theta_m$ to account for coherent propagation and the value of $P(E)$ to account for light escaping the system. This gives $D_{optic} = 11$ cm^2/s for the values in our simulation, much larger than the non-optical diffusion constant (1.5 cm^2/s) and therefore dominating diffusion.

This can then be added to the diffusion constant in the diffusion equation (4.16) which is then solved as in the non-recycling case (using the uncorrected external value of k_2). From the numerical solution, we can calculate the predicted PL and PC as depicted in Figure 4.7. We see that, for a non-fitted model, these both match fairly well to the data.

4.3.4 Photon diffusion model

If we assume frequent scattering, we should not apply coherence conditions for internal light transport, so the modal analysis in section 4.3.1 does not necessarily apply. However, if the scattering is weak, a similar outcoupling probability will be obtained, so we will continue to use $P_s = 0.95$.

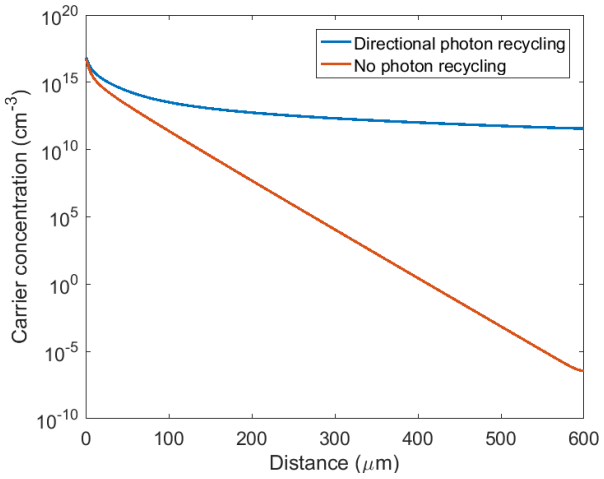

(a)

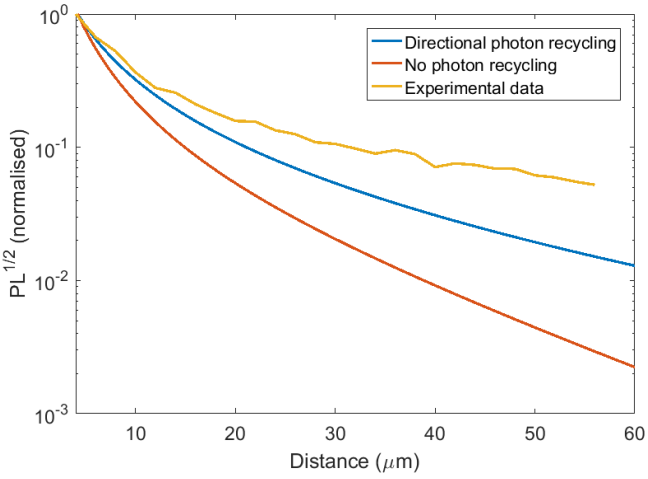

(b)

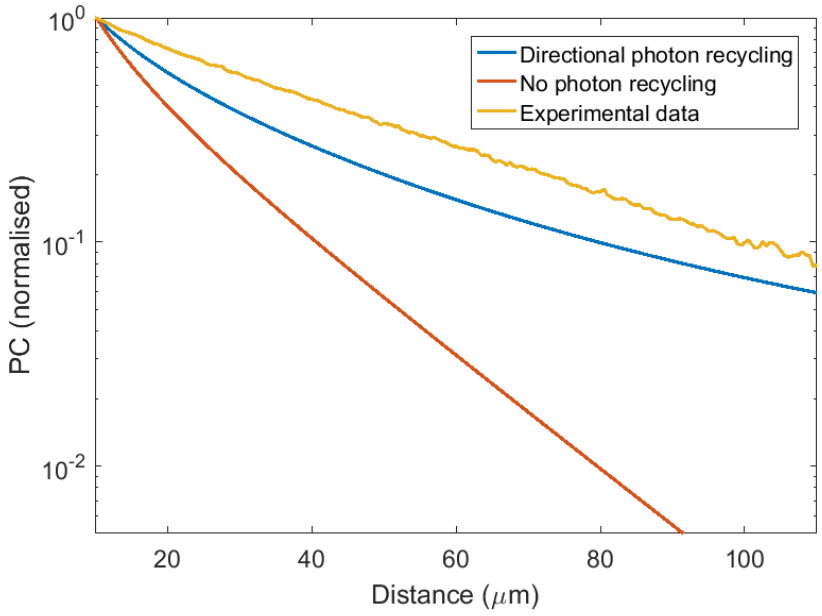

(c)

Fig. 4.6 Results of solving the diffusion equation including either directional radiation or no photon recycling. (a): the carrier concetrations. (b): the square root of the local photoluminescence, compared to the experimentally measured photoluminescence between 760-780 nm emerging from the film. Values are normalised at 4 μm. (c): The resulting photocurrents, compared to the measured photocurrent, all normalised at 10 μm.

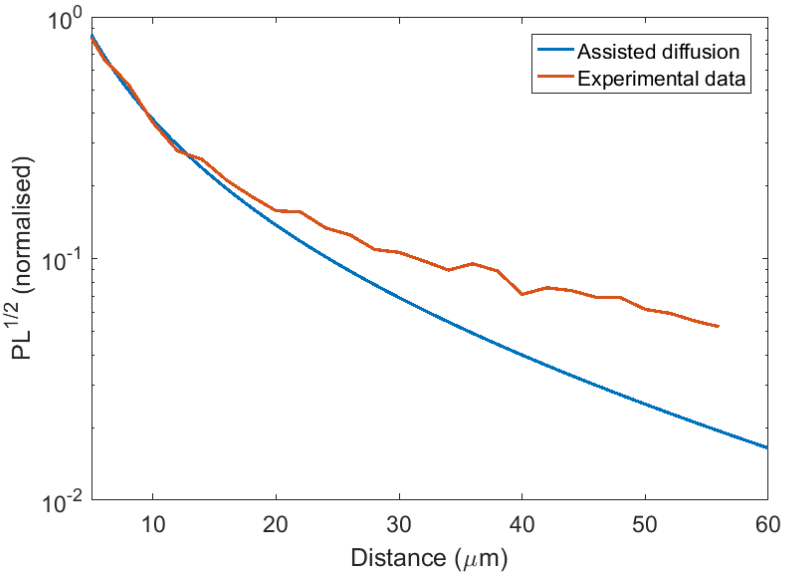

(a)

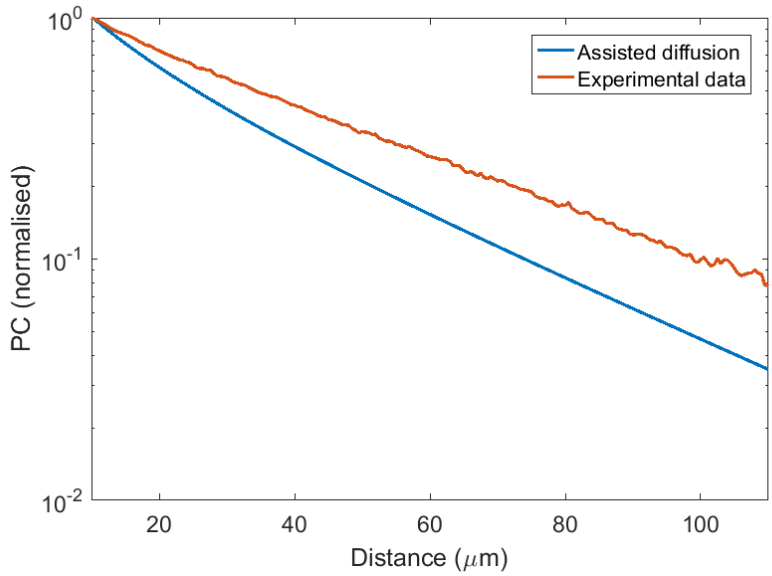

(b)

Fig. 4.7 Results of solving the diffusion equation with photon-assisted diffusion. (a): The calculated photocurrent, compared to the measured photocurrent, normalised at 10 μm. (b): the square root of the locally generated photoluminescence, compared to the experimentally measured photoluminescence between 760-780 nm emerging from the film. Values are normalised at 10 μm.

As described in section 4.1, we also cannot assign an uncontroversial value to the b constant in equation (4.2), however we can compare this model to the previous in the limit of no scattering, $\alpha_s \to 0$

$$\left\langle \Delta x_{light}^2 \right\rangle = 2N_{dim} D_{ph} \tau_{ph} = 2N_{dim} \cdot \frac{c}{3n_s b\alpha} \cdot \frac{n_s}{c\alpha} = \frac{2N_{dim}}{3b\alpha^2}, \tag{4.19}$$

where $\left\langle \Delta x_{light}^2 \right\rangle$ is the expectation value for the square of the light's displacement, N_{dim} the number of dimensions and τ_{ph} the time between emission and absorption of the photon. The expected squared light travel distance in the directional radiation model is independent of dimensionality of the system and given by

$$\left\langle \Delta x_{light}^2 \right\rangle = \frac{\int_0^\infty r^2 e^{-\alpha x} dr}{\int_0^\infty e^{-\alpha x} dr} = \frac{2}{\alpha^2}. \tag{4.20}$$

Equating equations (4.19) and (4.20) is not possible without stating the number of dimensions; we have a two-dimensional system, but are interested only in the radial motion, so if the step size is small compared to the radial co-ordinate we approximate this to the one-dimensional case. This matches for $b = \frac{1}{3}$, which is the value recommended by Durian [42] and in the range of values found by Aronson and Corngold [4].

However we also need to estimate reasonable values of α_s. If we assume that the irregularities on the upper surface of the film are possible causes of scattering, and that the noncoherently propagating light travels at the same angle to the surface as the coherently propagating light, then $\theta_m \approx 0.8$ radians, as shown in Figure 4.4b. In a noncoherent model of photons bouncing between the two interfaces, this would correspond to photons travelling around twice the height of the film between each contact with the upper surface, which would also be a reasonable value to assume if the light were emitted with no special angle. With $L = 100$ nm, this gives $\alpha_s \approx 5000\,000$ m^{-1}. If we also set $g = 0$ we have the maximum scattering situation. If scattering is rarer (or g larger) we can express $\alpha_s = \frac{s}{2L}$ for the scattering strength s. This gives us our wavelength-dependent diffusion constant,

$$D_\lambda = \frac{c}{n_s \left(3\frac{s}{2L} + \alpha_\lambda\right)}, \tag{4.21}$$

where α_λ is the absorption constant at that wavelength. Note that the assumption $\alpha_s > \alpha$ does not hold for most wavelengths if $s < 0.2$ for the values in our simulation. However, if light is absorbed and then emitted at the same wavelength and from the same location, it is effectively scattered, so the validity of this equation may be broader than what is trivially expected from a non-luminescent film.

With these relations and estimates established, we can set up the system of equations and solve them computationally. We wish to model the carrier distribution and light distribution at different wavelengths. It is necessary to divide the PL spectrum into wavelength bands, each of which is separately emitted, diffuse, and are absorbed by the perovskite, with the absorption constant assumed to be constant over the band. This produces a multicomponent set of interacting diffusion equations as follows:

$$\frac{\partial n}{\partial t} = G_{ext} + D_a \nabla^2 n + \frac{c}{\Re(n_s)} \sum_{\lambda} \alpha_\lambda \gamma_\lambda - k_1 n - k_2 n^2 \tag{4.22}$$

$$\frac{\partial \gamma_\lambda}{\partial t} = D_\lambda \nabla^2 \gamma_\lambda - \frac{c}{\Re(n_s)} \alpha_\lambda \gamma_\lambda + k_2 n^2 P_\lambda P_s \tag{4.23}$$

where γ_λ, D_λ and P_λ are the photon concentration and PL emission probability for each wavelength band and G_{ext} is the external generation. The ∇^2 terms in both equations arise from diffusion and the $\frac{c}{\Re(n_s)}$ terms show the production of carriers from the absorption of photons. This term converts the distance travelled by the photon to a time, and the minor change in the real part of the refractive index over this wavelength range is ignored for simplicity. The bimolecular recombination term, $k_2 n^2$, generates a photon, which has P_s chance of remaining in the active layer and P_λ probability of being in a particular bandwidth.

In one dimension this equation is numerically solvable in a matter of minutes by MATLAB routine, even with tens of wavelength bands. The results included in this publication used 40 bands for photons, as well as one for carriers, over a 400 μm radial grid with zero-flux conditions at the outside for all variables.

The resulting carrier distribution is plotted in Figure 4.8a for a range of s. The procedure for calculating the PL and PC from the carrier distribution is as described in the previous section.

In Figure 4.8b we compare the model's predicted PL to the measured PL data and find that the accuracy is fair at small distances for $s < 0.2$. In Figure 4.8c, we compare the PCs, we see a similar reasonable agreement for low scattering, $s < 0.02$.

4.4 Discussion

The root mean squared errors of the different models predictions is found in table 4.2.

Overall, the low-s photon diffusion models perform the best, although we should bear in mind that it has one tuning parameter, whereas the other models do not. Although we can state that $s < 0.02$, from a single experiment it is not possible to pick out a particular value below that. It may be noted from Figure 4.8 that the behaviour of the system is not very

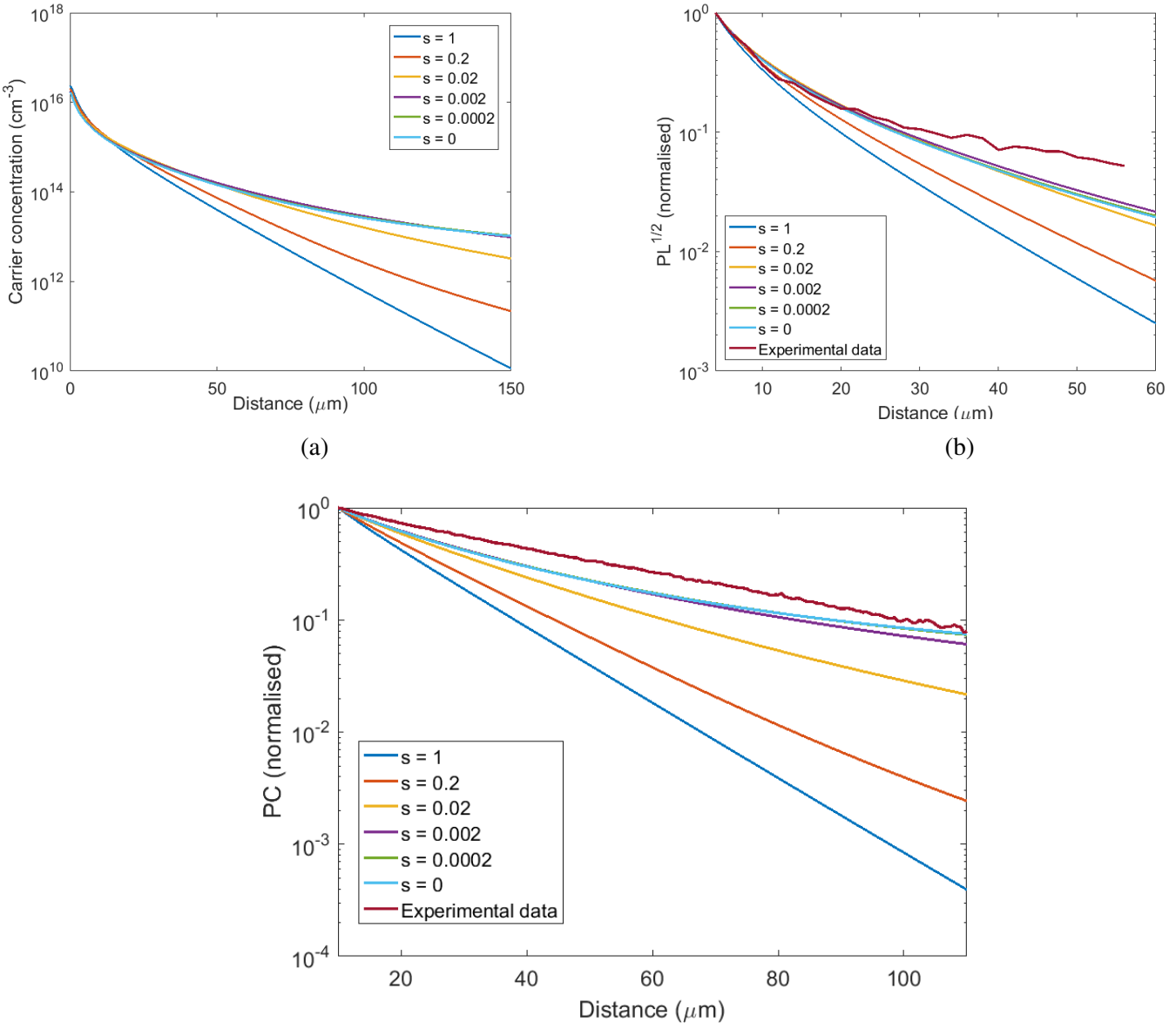

(a) (b)

(c)

Fig. 4.8 Results of solving the diffusion equation including photon diffusion. (a): the carrier concetrations, plotted for a range of scattering strengths, including applying the diffusion equation with scattering turned to zero. (b): the square root of the locally generated photoluminescence, compared to the experimentally measured photoluminescence between 760-780 nm emerging from the film. Values are normalised at 4 μm. (c): The calculated photocurrents, compared to the measured photocurrent, all normalised at 10 μm.

Table 4.2 The root mean squared error of the different models as compared to the experimental results for PL and PC. The models are: no recycling, directional photon recycling, assisted diffusion, and then five photon diffusion models with different s values.

	None	Direct	Ass. dif.	$s = 1$	$s = 0.2$	$s = 0.02$	$s =$ 2e-3	$s =$ 2e-4	$s = 0$
PL	0.168	0.105	0.093	0.155	0.128	0.084	0.0732	0.079	0.080
PC	0.214	0.103	0.111	0.220	0.192	0.127	0.081	0.080	0.081

sensitive to variation in s below this limit, and that the variation is non-monotonic. This is reasonable, as slightly increased confinement of bluer light near the origin may increase the generation of redder light, which can then travel further. However the measurement errors in the values put into the simulation and the small differences between the results in table 4.2 mean that it would be unwise to claim $s \approx 0.002$ with any degree of precision. It is worth noting, though, that this corresponds to $1/\mu_s \approx 100\ \mu$m, which is consistent with random lasing results showing the lengthscale of the lasing quasi-modes (originating from scattering) is > 100 μm [35].

Looking at Figures 4.6, 4.7 and 4.8, the PL estimates all significantly deviate from the measured values at large distances. This is where the model becomes most sensitive to light with very low absorption rates The lineshapes of the PC are also significantly different from experiment in all three cases. It is clear from the large-distance behaviour that some aspect of the problem that is not well-captured by any of these models, but that they give a fair indication of the effects of photon recycling. The large distance behaviour is also strongly dependent on the exact absorption of the low-absorption tail of the PL, which is hard to measure, so we intrinsically expect a high degree of error here.

Unfortunately, the most accurate model is one which has a weak theoretical justification. The derivation of the photon diffusion model assumes that scattering is stronger than absorption, which does not hold here. Our justification for still using this model is that absorption and re-emission events may be modelled as scattering in some cases, however since re-emission occurs with low probability outside the first few microns, this is not entirely convincing. It is likely that a subtly different approximation should be used in this case, taking account of the directional tendency of generation. A physically reasonable suggestion might be to include a directional term depending on the spatial change in emitted light level, like the assisted diffusion term to account for this. Further work needs to be done to derive approximations for lightly-scattered light, and to gather data in a variety of recycling systems to compare to the computational findings.

4.5 Conclusion

Photon recycling in a MAPbI perovskite back-contact solar cell has been investigated experimentally and the values obtained have been compared to a range of different simulation approaches. A means of accounting for the photonic nature of coherent propagation is developed, and as the emitted light is found to primarily occupy one photonic mode, the absorption constant is adjusted to match the behaviour of this mode. The directional propagation model, the one expected to work for a non-scattering sample, is developed for two dimensions and solved numerically, however this is not found to match the experimental values particularly well. The simplified version of this model, the assisted diffusion model, is also order-of-magnitude correct but not phenomenally accurate. The best match to data is given by the photon diffusion model for low scattering values, although this is problematic because in the low-scattering limit, the photon diffusion approximation is not formally valid. Further investigation, both mathematical and experimental, is needed to clarify this.

Chapter 5

Predicting the impact of cell structure on the efficiency of back-contact perovskite solar cells

5.1 Introduction

Back-contact solar cells offer the opportunity for optimised optical properties by moving all electrically conductive parts to the back of the cell [103]. This technology has been responsible for silicon solar cells breaking the 25% PCE limit, and interdigitated solar cells currently represent the most efficient silicon technology [58]. However it also introduces the need for fine-scale control of the electrodes on the back, and can increase production price. We need to prevent shorting between anode and cathode, however we expect that small electrode separation is needed for optimal device performance. There are several proposed techniques to achieve this control, all with different payoffs between fine-scale control and manufacturing cost [36]. Also, in terms of optimising device performance, we greatly increase the number of free variables that need to be investigated, hence a need for rapid screening of different architectures and outlining of where we expect performance maxima to occur, such as through drift-diffusion modelling. While there has been extensive work into optimising the layout of silicon back-contact cells [87, 80, 97] as well as some work on GaAs devices [83], there has yet to be any work theoretically examining perovskite back-contact devices.

These computational investigations tend to happen on mature systems, where the basic device architecture and desired constituent materials are already known, and we are merely interested in adjusting the widths of certain regions. However with perovskites, we are still

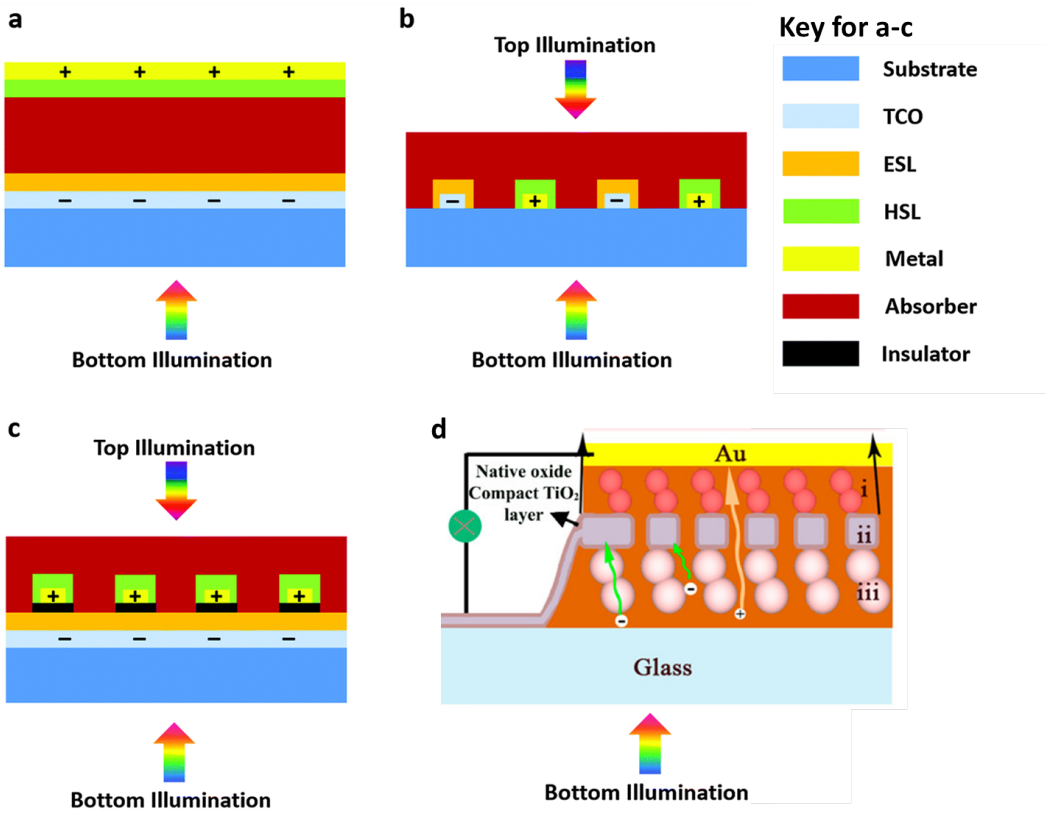

Fig. 5.1 2D cross-sections of the different cell designs investigated. a: vertical cell. b: interdigitated back contact cell. c: quasi-interdigitated back contact cell. d: porous mid-electrode cell. This has two different porous mesostructured scaffolds (i and iii) separated by a porous mesostructured electrode (ii). a-c reproduced from [70], d reproduced from [64].

very much at the formative stage, and there remains a wide phase-space of designs and materials to try out. In this chapter, we will begin to outline the trade-offs of the design phase-space as we computationally investigate the effects of different geometries and system sizes on perovskite device performance using the 2D drift-diffusion model. We will attempt to keep the model general, and make as few assumptions about the non-perovskite layers as possible. We will also outline computational means to incorporate photon recycling into the 2D models needed to investigate these back-contact devices.

At the time of writing, there have been three different methods of fabricating perovskite cells described as 'back-contact'. These are the 'interdigitated' geometry of Pazos *et al.* [123], the 'quasi-interdigitated' geometry of Jumabekov *et al.* [70] and the 'porous mid-electrode' cells of Hu *et al.* [64]. Schematics of how the devices are physically configured can be found in Figure 5.1. Here we will assess the potential of these designs.

Interdigitated back-contact solar cells (IBSCs) have a series of alternating electrode fingers extending from either side. In the case of Pazos *et al.*, the indium tin oxide (ITO) fingers are formed by photolithography, followed by electrodeposition of different transporting layers on alternate fingers [123]. In the case of quasi-interdigitated solar cells (QISCs), one electrode and transporting layer is put down globally, then an insulating layer, electrode and transporting layer are deposited on top. These upper three layers are selectively etched to reveal regions of the original electrode. This removes the between-electrode gap seen in IBCs, decreasing the inter-electrode separation. It is worth remarking that if these cells have either well-spaced electrodes or transparent electrodes, then the cells are suitable for bifacial designs, where light can be incident from both sides of the cell. This can be a cheap way to achieve many of the same advantages as concentrator solar cells using simple white paint, while also allowing the cell to radiate more infrared light, thus remaining cool [65, 60].

In the porous mid-electrode solar cells (PMESCs), there is something of a philosophical question as to whether they count as back-contact, as one electrode occurs midway through the perovskite layer, however there is little absorption below this electrode. The implementation relies on the active layer having mesoporous layers to support the middle electrode. To construct these cells, the first mesoporous layer (TiO_2) is deposited, followed by a porous electrode layer (Ti, with native oxide on the surface). Then a second mesoporous layer (ZrO_2) is laid on top, and the active layer can be infilled. A planar back-contact electrode is then evaporated onto the back of this. The titanium oxide facilitates transport of the electrons to the Ti electrode, whereas the ZrO_2 layer is simply a spacer layer. There is no dedicated hole-transporting material.

5.2 Thermodynamic models

Without modelling precise carrier distributions, we can estimate maximum cell performances through thermodynamic limits. This then gives us a point of comparison for the different cell designs. Previous work [78] has established a theoretical limit to the efficiency of perovskite solar cells, including the effects of photon recycling, however in that work, absorption coefficients were calculated from photoluminescence using a simplified van Roosbroeck-Shockley relation, in a manner that neglects non-optical interconversion between energy states. The full thermodynamic expression requires conditions on energy level occupancy [14], which we do not expect to hold when the optically excited states can decay to a lower energy state [66], hence the simple version of the relationship is not found to be valid [2]. Instead, we will repeat the calculation using the absorption from

ellipsometry data by Löper *et al.* [96]. This compares more favourably with absorption data from photothermal deflection spectroscopy [123] than the convered PL data does.

At open-circuit voltage, the cell's behaviour is controlled by the balance between incoming light and outgoing light. As described in chapter 2, we expect

$$V_{oc} = \frac{k_B T_c}{q} \log\left(\frac{\eta Q_{in} \varepsilon_{in}}{Q_{out} \varepsilon_{out}}\right). \tag{5.1}$$

Assuming there is no solar concentration or back-illumination on the system, the étendue of the sun at normal incidence is $\varepsilon_{in} = A\Omega_{sun} = A\pi \sin^2(\theta_s)$ for $\theta_s = 0.266°$, the half-angle of the sun [17]. The étendue of the hemisphere that the system re-emits into is

$$\varepsilon_{out} = 2\pi A \int_0^{\pi} \sin\theta \cos\theta \, d\theta = \pi A.$$

This gives a V_{oc} loss of $\frac{k_B T_c}{q} \log\left(\frac{\varepsilon_{in}}{\varepsilon_{out}}\right) = -0.27$ V. The balance of light in and out is given by the absorption characteristics of the cell whose total absorption fraction will be called σ, resulting in the light absorbed being given by $Q_{in} = \int d\lambda \sigma(\lambda) I_s(\lambda)$, where $I_s(\lambda)$ is the incident sunlight. This is balanced by Q_{out} in thermal equilibrium, where I_s is replaced by the black-body spectrum, we assume at ambient temperature (297 K).

If reflection from the smooth front surface is minimised and there is perfect reflection from the back surface, a distance H away, $\sigma = \int_0^{2H} e^{-\alpha x} dx = 1 - e^{-2\alpha H}$. For illustrative purposes, we can use a height of 300 nm. If the input light distribution, Q_{in}, is the black-body radiation at the sun's temperature of 6000 K, we get a V_{oc} contribution of 1.56 V, approximately the bandgap of the MAPbI, as expected for a sharp absorption onset. This V_{oc} is then 1.29 V after étendue loss. If we instead use the nonscattered (direct) incident light spectrum under AM 1.5 illumination [116] (which gives $G_t = Q_{in}\varepsilon_{in}$ photons, which we normalise per unit area), we obtain $V_{oc} = 1.17$ V, due to factors like atmospheric absorption. We also expect a loss of $(k_B T_c/q) \log \eta$. Experimentally, peak $\eta \sim 30\%$ [34], giving a V_{oc} loss of around 0.03 V. However in practice, this efficiency will depend on the concentration of carriers, which depends on the cell volume. If the carriers efficiently diffuse, at steady state open-circuit voltage we have

$$\frac{G_t}{H} - k_1 n - k_2 n^2 = 0 \Rightarrow n = \frac{-k_1 + \sqrt{k_1^2 + 4k_2 G_t/H}}{2k_2}. \tag{5.2}$$

If all bimolecular recombination is radiative, we have internal quantum efficiency

$$\mathrm{QE} = \frac{k_2 n}{k_2 n + k_1}, \tag{5.3}$$

then we must consider the probability for light to escape a thin film. If we use a noninterfering model, this is approximately $P_{esc} = 1/2n_2$ [167], although for smooth films of width comparable to the light wavelength, the height-dependent coherent transmission matrix formalism gives more precise results. In either case, nonescaping light can be reabsorbed and re-emitted with probability QE again, and by summing the geometric series, we obtain

$$\eta = \frac{\mathrm{QE}\, P_{esc}}{1 - \mathrm{QE}(1 - P_{esc})}. \tag{5.4}$$

We can also estimate $J_{sc} = qG_t$, as most carriers generated will be extracted when drifting with the internal field. Although detailed equations will be required to discover the fill factor, we can set this to one and construct a crude estimate of PCE by simply multiplying V_{oc} and J_{sc}. The results of this calculation are shown in figure 5.2. Both PCE and J_{sc} show a strong improvement with added height because of the increase in absorption. In practice, the fill factor is strongly determined by the diffusion behaviour and even at short circuit, some carriers recombine, so neither will necessarily monotonically increase with height.

5.3 Comparison of device geometries

To get more precise, 2D descriptions of the impact of cell geometries on efficiency, several different geometries were used to build meshes for the MATLAB 2D finite-element drift-diffusion equations solver, as described in chapter 2. For simplicity of comparison, all cells were assumed to have the same TiO_2 electron acceptor and spiro-OMeTAD hole acceptor contacts, which determine the boundary conditions imposed at the electrodes. Fundamental parameters used in this simulation are shown in Table 5.1. We are using the macroscopically measured value of bimolecular recombination, which includes photon recycling effects, so we will not add photon recycling effects on to this model – this means we do not presently have to worry about the means by which it operates. We will confine ourselves at present to studying a small system, with 1 μm pitch distance in cases where pitch distance is a relevant consideration, limiting the potential impact of long-range photon transport.

It is necessary to input some optical parameters into the simulation to determine the behaviour of light in the system. However this study does not attempt to model the specific nature of the antireflective layer or reflection from the backing layers, so we will incorporate

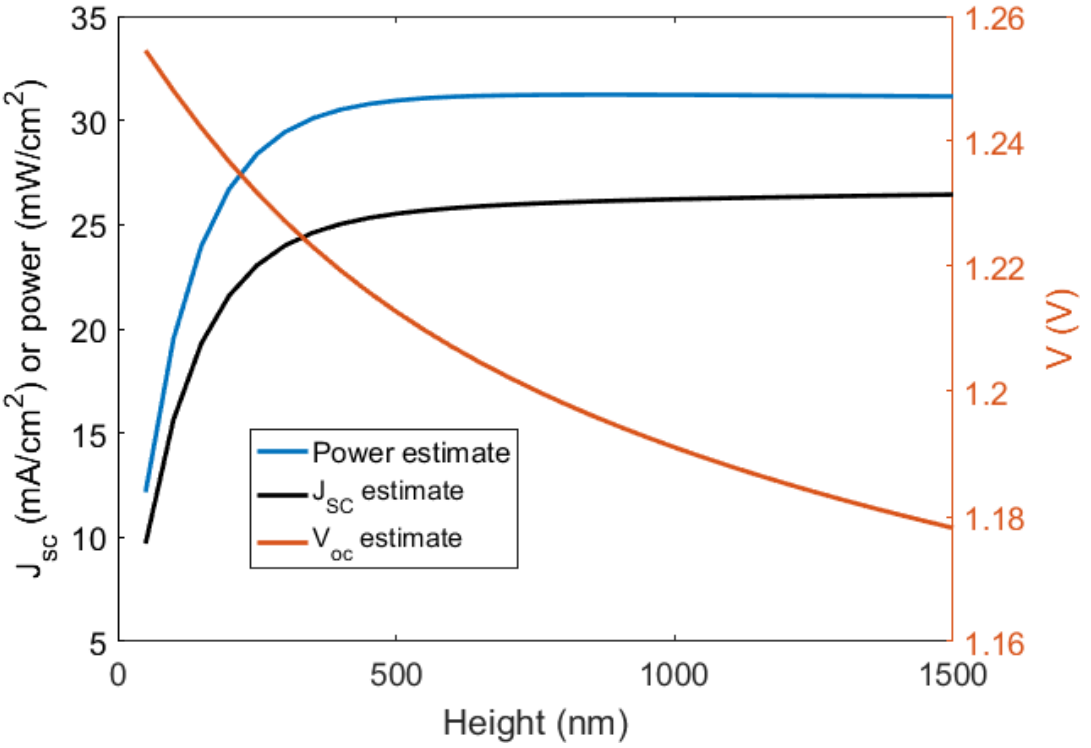

Fig. 5.2 The variation of power output and current (left scale) and voltage (right scale) with height of the active perovskite layer predicted from thermodynamic simulations.

a nonscattering front interface with a reflective back contact and assume no interference between the incoming and outgoing waves, giving us a double Lambert-Beer law,

$$G(z) = \int d\lambda\, \alpha \left(e^{-\alpha(H-z)} + e^{-\alpha(H+z)} \right) P_{AM1.5}\,, \tag{5.5}$$

where $P_{AM1.5} d\lambda$ is the AM1.5 power intensity at wavelength λ.

With these device parameters, we can use the 2D simulation to establish the performance characteristics of the structures.

We begin with modelling a vertical cell, where electrons and holes are extracted from the front or back, in keeping with most research cell designs. This serves to check that the two-dimensional code does not introduce any spurious features and gives a point of comparison. The data produced shows that lateral variation (i.e. noise) is very minor when the program behaves physically, which includes all the power-generating voltage range. It is worth noting that in cases where the model breaks down due to excessively large applied voltages, the spuriously large values are not laterally consistent, and that these large errors are more likely to appear with finer meshes. While we generally expect finer meshes to exhibit

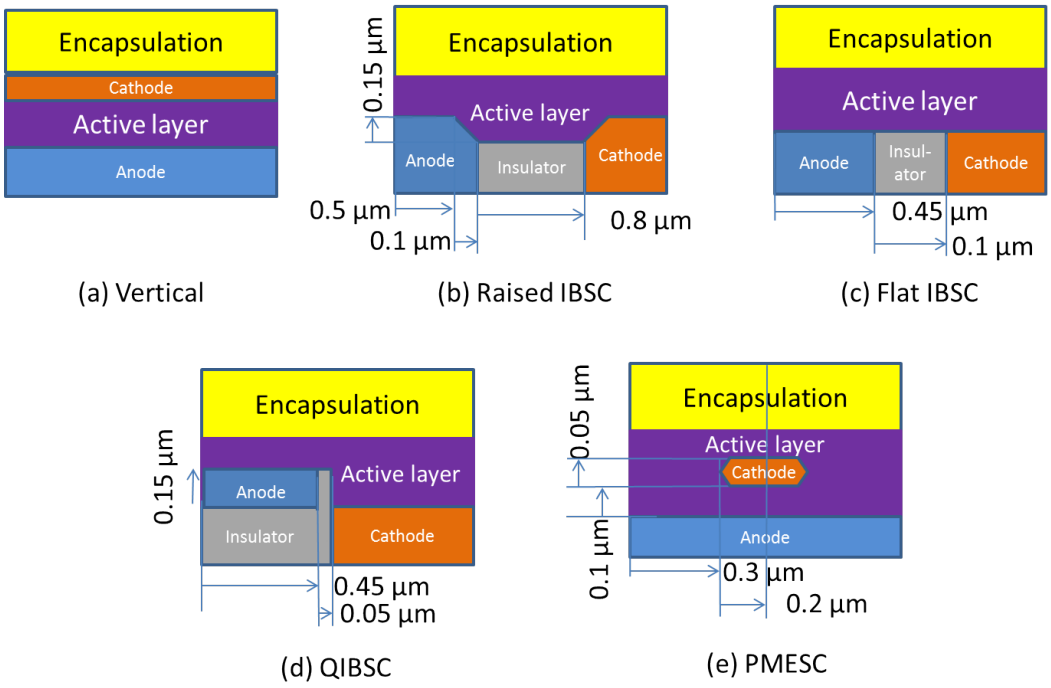

Fig. 5.3 2D cross-sections of repeat units of the different cell geometries used in the simulations. Diagrams not to scale, real distances indicated for initial simulations with 1 μm total pitch distance. The height of the active layer is initially varied, but vertically labelled distances are unchanged. Later, the width of the cell is changed, and horizontal lengths will change to keep in proportion. Thin electron- or hole-transporting layers are assumed present in between the active layer and the electrodes.

Symbol	Description	Value	Source
H	Height	350 nm	Input
L	Pitch length	1 μm	Input
m_e	Relative electron mass	0.12	[22]
m_h	Relative hole mass	0.15	[22]
n_i	Intrinsic carrier concentrations	3×10^4 cm^{-3}	[118]
n_{Ti}	Electron density at TiO_2	4.8×10^{14} cm^{-3}	[118]
p_{sp}	Hole density at Spiro-OMeTAD	1.0×10^{12} cm^{-3}	[118]
ε_r	Static dielectric constant in the perovskite	25.7	[22]
T	Temperature	293 K	
D_n	Electron diffusion constant	0.63 cm^2/s	[37]
D_p	Hole diffusion constant	2.65 cm^2/s	[37]
τ_e	Trap fill time for electrons	0.056 μs	[66], TRPL
τ_h	Trap fill time for holes	0.22 μs	[66], TRPL
n_t	Trap density	3.3×10^{10} cm^{-3}	[144]
k_2	Bimolecular decay rate	8.0×10^{-10} cm^3/s	[66], TRPL

Table 5.1 The values used in all simulations unless otherwise specified. These represent good but achievable device parameters. In the case of [66], two measurement techniques were used to measure the values referenced – we have used the values obtained by time resolved photoluminescence (TRPL).

higher accuracy, they have more degrees of freedom, meaning more opportunity for errors and spurious oscillations to grow. This means smaller meshes may increase the instability of the numerical solution [3].

Fortunately these breakdowns do not occur under operational voltages so we use our 2D model to calculate the parts of the JV curve that determine performance values. The 2D representations of the different geometries are shown in Figure 5.3. We will use the same equations for all devices, although in practice manufacturing requirements mean that not all devices can be made with the same selective layers and the optics and bulk characteristics may significantly vary depending on deposition. Examples of device recombination and current flows are shown in Figure 5.4 for when the devices are held at 1V (near the maximum power point).

In figure 5.5 we see some performance metrics for the different cells. The effects of switching the position of the electrode and cathode in vertical, QIBSC and PMESC cells was also investigated, but the differences in performance were small and so only the versions depicted in figure 5.3 are presented for clarity.

Figure 5.5a shows the J_{sc} of the different geometries as the height of the perovskite layer is changed. There are several noticeable features. Firstly, for all curves the general curve shape is consistent with the thermodynamic model above. This shows that, for relevant

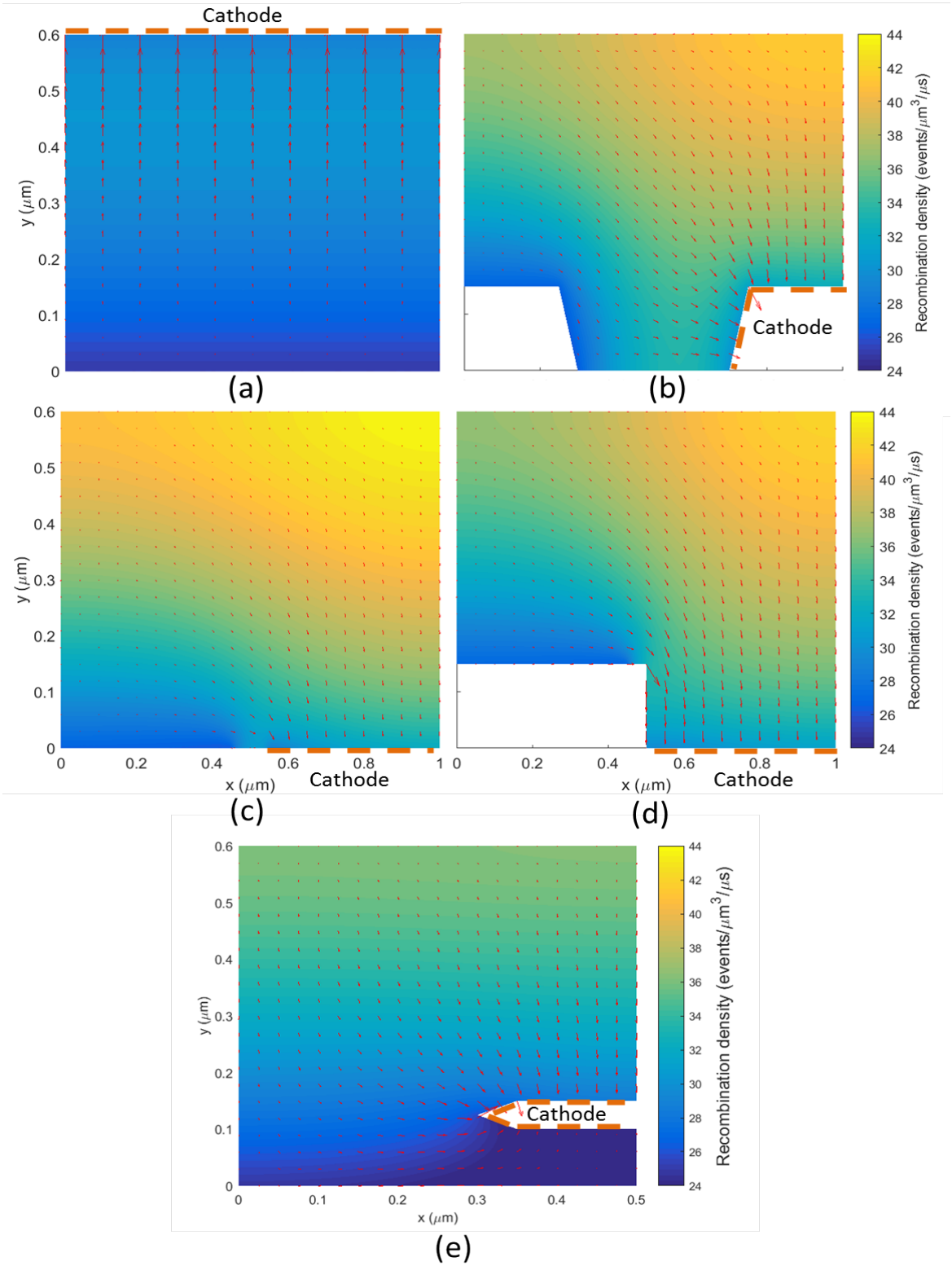

Fig. 5.4 Recombination density through simulated devices held at 1V applied bias. Arrows indicate the direction of the electron current, with length proportional to current density. Boundary with cathode is marked in orange. a: Vertical device. b: Raised IBSC. c: Flat IBSC. d: QIBSC. e: PMESC. Note that this graph has a different x-scale to the others.

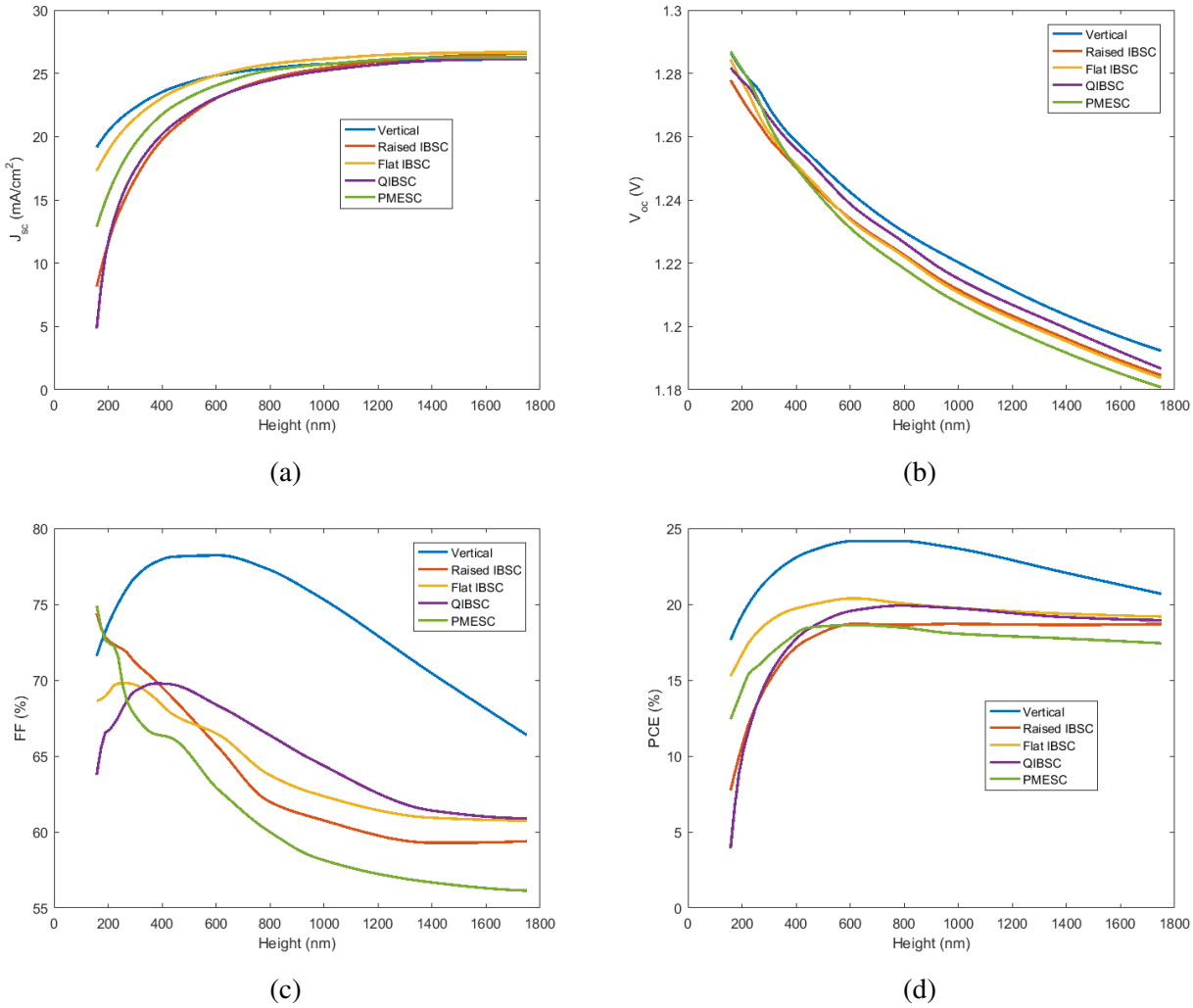

Fig. 5.5 Performance metrics for different geometries of 1 μm long cells as the height of the active layer is changed. a: J_{sc}. b: V_{oc}. c: FF. d: PCE.

cell heights, the total absorption is more important than recombination, hence a monotonic increase in current with increasing height. This also explains the reduced starting point of the raised IBSC and QIBSC – these cells have large raised electrodes that reduce the volume of the active layer, although this matters less as the active layer becomes higher. Secondly, the vertical device is initially better, due to very short extraction lengths and a guiding electric field, whereas the other electrodes require a degree of diffusion of carriers generated above the electrodes, where there is a relatively uniform electric field.

We see in figure 5.5b that the V_{oc} values change only weakly with cell height and even more weakly with cell geometry. Comparing these results with figure 5.2, we see the values were well-predicted by thermodynamic considerations. However we also see that, in

taller cells, the vertical devices have a slightly higher V_{oc} than the other designs, because electrons generated near the upper surface are created next to one electrode and therefore the concentration of carriers next to that electrode is higher than the bulk value. In back-contact devices at $V > V_{bi}$, most carriers will be generated away from both electrodes and will need to diffuse before they are extracted, resulting in lower carrier concentrations at both electrodes. The PMESC device has a crossover region between the two electrodes that receives little light and is hard to diffuse into. In deep devices, there will therefore be some charge injection at voltages over V_{bi}, reducing the V_{oc}.

Figure 5.5c shows that the fill factor gives the most significant variation between cell designs, and is also where we see behaviour that was not intimated by the thermodynamic model. The shapes of the curves show markedly different and nontrivial interplays between drift, diffusion and recombination in each geometry, typically resulting in the peak FF around 500 nm. Figure 5.5d shows the product of all these factors, and the clear winner is the vertical device, at a height between 600-700 nm. However these devices will in practice have some self-shadowing from the electrodes, which was not accounted for in the model – in the case of the vertical device, this could easily account for a 10% decrease in cell performance. The PMESC will have this problem to a much lesser degree, and will also have noticeably different internal transport properties than its competitors, as with the current means of manufacturing it relies on the bulk having mesostructured frameworks. PMESC also has both electrodes close together, meaning that there is little electric field in the bulk of the device and most separation happens by diffusion. The raised IBSC performs poorly, due to its large lower area where no carriers are extracted, meaning that more recombination can occur. This feature could become an advantage if there were high interface recombination at electrodes (but not at the insulator), however we already have developed perovskite processing techniques to reduce interface recombination to very low levels [18], hence it has not been included in the model. Following on from these results, we will consider only the most efficient design, the flat IBSC.

5.3.1 Changing the pitch distance

Increasing the pitch distance will lead to more opportunities for recombination before extraction. However it will also be easier, quicker and cheaper to manufacture, as well as reducing the electric field that must be diffused against when $V > V_{bi}$. The pitches chosen above were similar to those easily manufactured according to the various methods - while PBESC is easily adjustible, the other techniques are less so.

The JV curves of simulated cells of different lengths can be found in figure 5.6. We see that although J_{sc} monotonically decreases with cell width, the overall performance is fairly

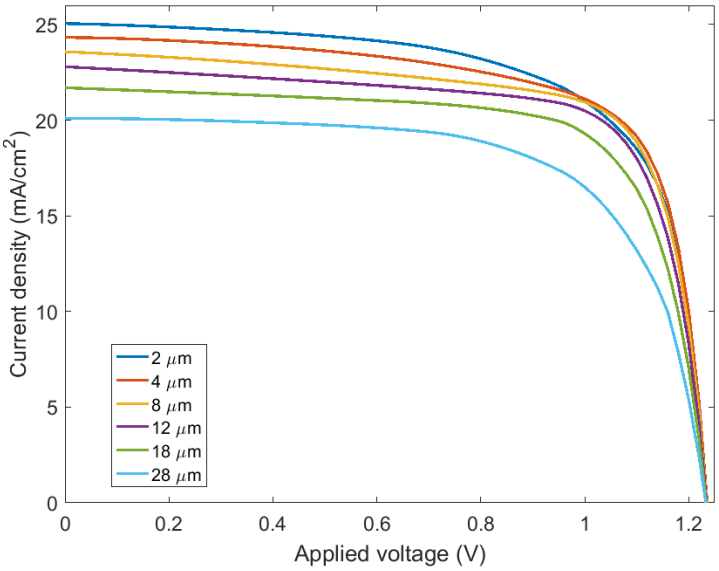

(a)

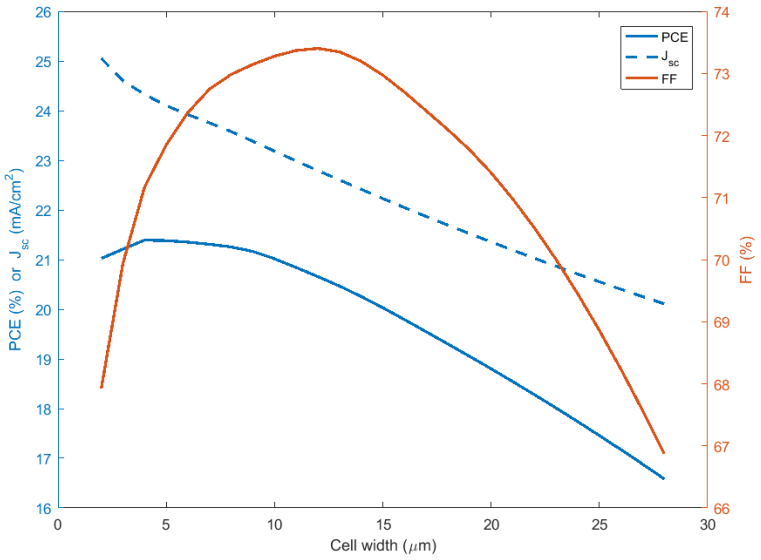

(b)

Fig. 5.6 a: JV curves of 600 nm high flat IBSC cells with different pitch distances. b: The J_{sc}, PCE and FF of these cells as a function of pitch distance. PCE and J_{sc} on the left scale, FF on the right.

level for devices less than 5 μm wide due to the slight decrease in the fill factor. V_{oc} changes by much less than 1% across all pitch distances. The maximum device efficiency is 21.4%, which occurs for a 4 μm pitch length device.

5.4 Including photon recycling

As discussed in the previous chapter, there is some question over the correct way to incorporate photon recycling effects into this model. These concerns are exacerbated for general cases where we attempt to make predictions that do not depend on the precise nature of the surrounding layers. However, a large proportion of the photons emitted will be absorbed over a short distance, before many bounces have occurred. These photons can presumably be modelled with the non-local direct radiation approach based on spherical (not cylindrical) waves, as has been done in previous one-dimensional models [40, 10, 165]. There have also been attempts to incorporate the full Maxwell equations into multidimensional drift-diffusion models [45], or to proceed through a ray-tracing model [121], both of which require a fairly large degree of computational resources to solve the problem on dense grids. Our model is somewhat similar to the last of these, although adjusted for both computational efficiency and for application to the situation of repeating geometry that we face.

For this simulation, we are in the regime where the small distances between electrodes are relevant, and are only interested in the absorption location modulo the pitch length. Light that travels distances longer than the pitch length will have a relatively even distribution across the cell irrespective of the model we use to determine its final location, and so our results should not be sensitive model errors in this regime. Provided our pitch length and height are comparable, so scattering or reflection is rare compared to light travelling over whole symmetry units, we do not need to worry about how scattering or photonic transport happens.

We will therefore model the recycling generation function using previously mentioned direct transport generation function [84, 40], as in chapter 4, here written in our laterally symmetric situation in terms of in-plane radial separation distance r', in-plane angle ϕ' and out-of-plane distance z' with total distance ρ. This gives us a generation function contribution of

$$G_{ph}(\mathbf{r},n,p) = \int_{E=0}^{\infty} \alpha(E)P(E) \int_{\theta'=0}^{\pi} \int_{\phi'=0}^{2\pi} \int_{r'=0}^{\infty} B \cdot \left(n(r',\phi')\, p(r',\phi') - n_i^2\right) \frac{\exp\left(-\alpha(E)\rho\right)}{4\pi\rho^2} r' dr' dz' d\phi' dE. \quad (5.6)$$

Once again, we will separate out the part that depends on the separating distance, G_{phR} and the part based on the carrier concentrations at the source, (r',ϕ')

$$G_{ph}(\mathbf{r},n,p) = \int_0^{\infty} r' dr' d\phi'\, G_{phR}(r,r') B \left(n(r',\phi')\, p(r',\phi') - n_i^2\right). \quad (5.7)$$

G_{phR} is only a function of the in-plane separation between between the source and absorbing volume, which we will denote R. However the total separation, ρ, also depends on z. We therefore find G_{phR} by integrating over the line perpendicular to the plane, with length variable $z' = \sqrt{\rho^2 - R^2} \Rightarrow dz' = \rho/\sqrt{\rho^2 - R^2} d\rho$. We wish to evaluate this numerically on a mesh, so if the in-plane area of the source mesh is A_s, we can calculate the local contribution

$$G_{phR,local}(R) = \int dE\, P\alpha A_s 2 \int_R^\infty \frac{e^{-\alpha\rho}}{4\pi\rho\sqrt{\rho^2 - R^2}} d\rho. \tag{5.8}$$

Substituting $u = \rho/R$,

$$G_{phR,local}(R) = A_s \int dE\, P \frac{\alpha}{2\pi R} \int_1^\infty \frac{e^{-\alpha u R}}{u\sqrt{u^2 - 1}} du. \tag{5.9}$$

This integral is not analytically solvable, but the u-singularity at the origin is well-behaved and so we can numerically solve this to find the additional photon recycling generation function on our Delaunay-triangulated grid. The one exception to this is that we will need to find the self-absorption of a grid section, in which case we encounter the $R = 0$ singularity. This singularity is also radially integrable, and so disappears if we take account of the variation across the face of the grid triangle, but it is hard to rigorously integrate this self-absorption term over the face of our arbitrarily shaped triangular prism. We will instead approximate the integral using the absorption of light from the center of a cylinder with the same area, of radius $r_c = \sqrt{A_s/\pi}$. This is

$$G_{phR,local}(0) = A_s \int dE\, P\alpha \int_0^{r_c} dR \int_1^\infty \frac{e^{-\alpha u R}}{u\sqrt{u^2 - 1}} du \tag{5.10}$$

$$= A_s \int dE\, P \int_1^\infty \frac{(1 - e^{-\alpha u r_c})}{u^2\sqrt{u^2 - 1}} du. \tag{5.11}$$

In practice, equations 5.9 and 5.11 are computationally costly to calculate, so instead of calculating the value returned between every pair of lattice points (and reflections of lattice points, and reflections of reflections of lattice points) we will tabulate values across the necessary range of distances and interpolate between these results. Any electrode projection into the active area is assumed to have the same absorption constant as the active area, but light absorbed in this area does not result in charge generation. We will assume a loss of 10% from light incident on the upper surface and allow the rest to be reflected, but will assume perfect reflection from the rear and the two sides (the sides do not represent true reflections, but symmetry points of the system). We will calculate the contributions arising from any two such reflections and add them to the direct radiation contribution, then assume

that, of the light neither escaping nor absorbed so far, a fraction $P_{esc} = 10\%$ is lost and the rest is distributed equally over the active area. In order to implement this over a mesh with different area triangles while conserving carrier number, this last, spatially uniform generation contribution is weighted by the area of the source, A_i and the sinks, A_j. This results in a generation contribution of

$$G_{global,i} = \frac{A_i m_i}{\sum_j A_j}, \text{ where } m_i = 1 - P_{esc} - P_{noBounce} - \sum_j G_{phR,local}(|\mathbf{r}_j - \mathbf{r}_i|)\frac{A_j}{A_i}. \quad (5.12)$$

The sum over j includes both the mesh point j and reflections of the mesh point. $P_{noBounce}$ is the proportion of light that was incident on the top surface and did not rebound, calculated as

$$P_{noBounce} = \sum_{\text{top reflection j}} P_{esc} G_{phR,local}(|\mathbf{r}_j - \mathbf{r}_i|)\frac{A_j}{A_i}. \quad (5.13)$$

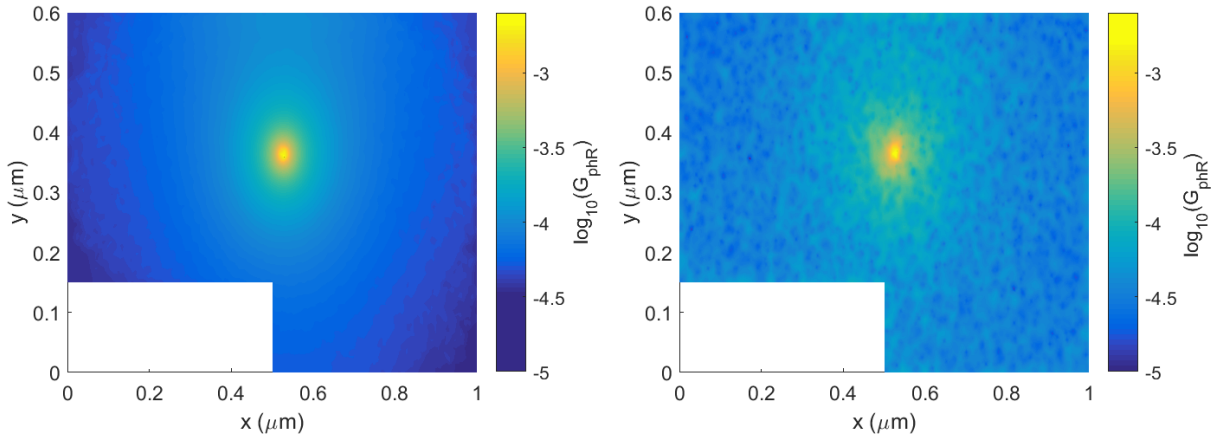

(a) (b)

Fig. 5.7 Example matrix entries from concentration-invariant G_{phR} from the center of a QIBSC. a: G_{phR} contribution throughout the cell arising from luminescent recombination occurring at the center. b: G_{phR} contribution at the center from luminescent recombination elsewhere in the cell. The contribution from each mesh region scales with the area of the region, hence the 'mottling' effect.

$G_{phR} = G_{global,i} + G_{phR,local}$ can be stored as a matrix to be multiplied by a matrix of the local luminescent recombination rates to give the additional generation contribution from photon recycling, as shown in figure 5.7b. The resulting computation can easily be performed on a desktop computer, however the difficulty of storing the large matrix G_{phRsum} limits the resolution and therefore accuracy of the simulation. To reduce the feedback, the photon recycling term is treated as a perturbation of the non-recycling solution, as done in

1D by Balenzategui and Martí [10]. The solution is calculated without it, then the additional G contribution is calculated and the problem is solved again, and the process is iterated to converge from below. For cases where the internal luminescence is calculated from experimental data, we should correct the second order recombination coefficient to represent the internal value rather than the externally measured value.

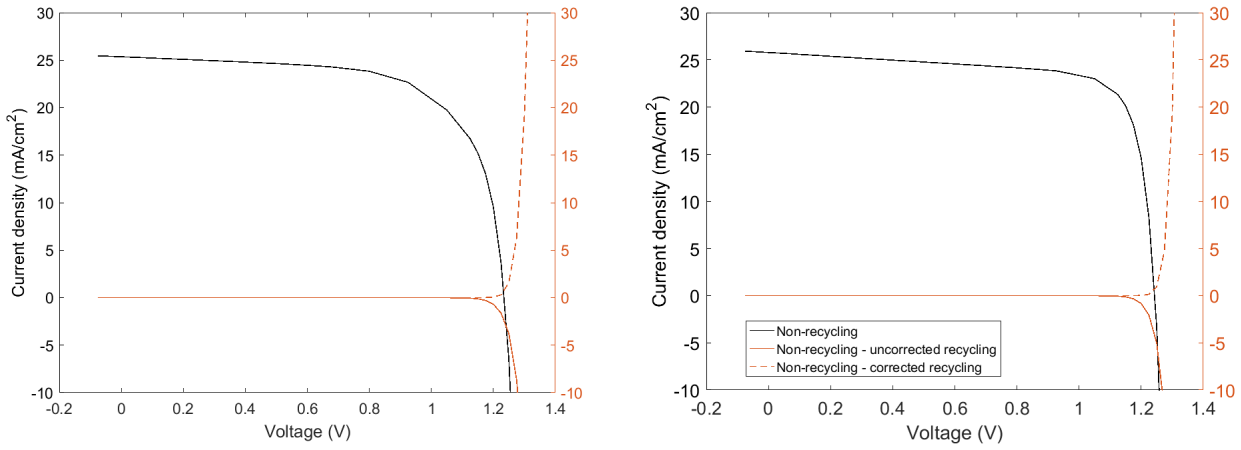

(a) (b)

Fig. 5.8 JV curves of perovskite cells from 1000 nm wide, 600 nm high 2D simulations, and the changes to these curves when photon recycling effects are included. Corrected recycling (dashed) is when the bimolecular recombination rate is increased to account for recycled light. a: Flat IBSC geometry. b: Vertical cell geometry.

The results of these simulations can be found in figure 5.8. The subfigures show that the changes to the JV curve are very small when energy is produced, with significant differences only appearing around V_{oc}. Photon recycling in general does not affect J_{sc}, where almost all carriers are extracted, and in this case also does not influence the maximum power point either. Therefore useful device performance is not affected here. This is consistent with experimental assessment of the importance of photon recycling under one-sun illumination [46]. The adjusted value of V_{oc} is given by the crossover point of the red and black lines. The dashed line describes the effects if we increase the internal radiative recombination constant to match the externally measured decay rate of uniformly distributed carriers. As carriers are not uniformly distributed during operation, but concentrated in the more-emitting upper region, this correction is subtly simplistic and produces a slightly poorer V_{oc} than having no photon recycling. If we do not correct the B coefficient, then we see a significant increase in V_{oc}, but more importantly than moving carriers around, we have effectively reduced B. These findings are seen in both the flat IBSCs and the vertical designs.

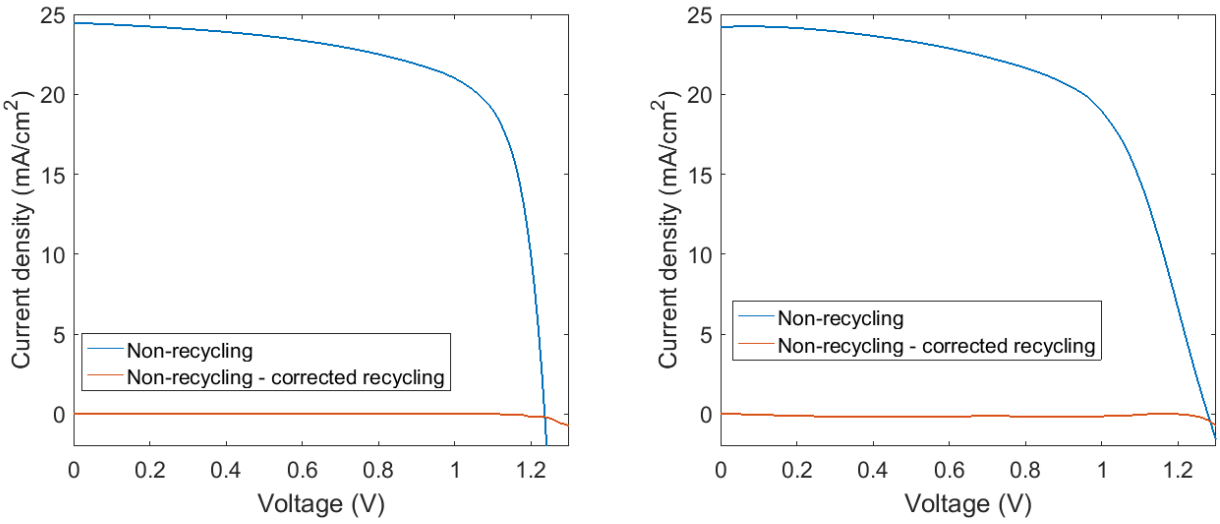

Fig. 5.9 JV curves of perovskite cells from 4000 nm wide, 600 nm high Flat IBSC 2D simulations, and the changes to these curves when photon recycling effects are included. a: Using the materials parameters as in table 5.1. b: Multiplying the trap fill times by 200 and dividing the diffusion constants by 50.

In Figure 5.9 we see the similar curves for longer (4 μm pitch length) systems, the optimised size found above. The lack of variation below V_{oc} is replicated for standard device parameters, although some small variation can be seen when monomolecular recombination strength is reduced but diffusion constant is increased. Changing only one of these parameters by around this much is insufficient to produce visible variation at lower voltages, and even with both changed the variation is minor. This indicates that the short-ranged transport effects of photon recycling will always be minor for perovskite device operation.

5.5 Discussion

The efficiency of back-contact solar cells is, considering only internal geometry, significantly poorer than that of the vertical devices for all geometries that are investigated here. The vertical cell clearly suffers a larger fill factor penalty than the other designs with increasing height, as the height also increases the electrode separation distance, however J_{sc} changes are small by the time this is significant. We expect there to be a significant optical benefit to back-contact devices, which may make the devices perform comparably, however the designs simulated here do not suggest that we can easily anticipate the same degree of performance improvement seen in silicon solar cells. This may be explained as follows:

firstly, silicon has much lower recombination rates [86] and higher mobility than perovskites ($\sim$ 1000 cm^2/Vs [26]), enabling long-ranged charge transport. Secondly, as it only absorbs via an indirect bandgap, it has a lower absorption constant than perovskites, hence a thicker active layer is required to absorb the incident light. This necessitates long vertical diffusion distances, whereas horizontal diffusion can be arbitrarily short. In perovskites, optimal cell height is typically less than a micron. The optimal active layer heights found in this study could be further decreased through the use of a textured front surface, whereby perpendicular incident light is refracted to travel at large angles and therefore has a longer travel length than the film height.

Interestingly, the operational efficiency of back-contact cells are not substantially affected by changing the pitch distance provided it does not exceed 10 μm. This is convenient for many forms of manufacturing like lithography, and only slightly above the lengthscales that can be achieved using screen printing and offset printing [25]. However the many-microns pitch distances that are used for silicon back-contact cells will not be applicable for MAPbI. The most efficient back-contact cell discovered through our process was a 0.6 by 4 μm flat IBSC, achieving an efficiency of 21.4%, whereas the vertical cell design peaked at 24.2%. This means that an optical improvement of more than 13% would be required to incentivise a switch to back-contact cells. This figure would decrease if the recombination rates were to decrease or the mobilities increased, however the impression we are left with is that progress in efficiency will come more from changing the nature of the active layer rather than changing its shape.

The 2D photon recycling model shows that we can safely ignore the operational effects of optical transport in a uniformly excited system. Although there is some redistributive effect from the photon recycling, the level of recombination is fairly uniform in our case and the changes to the system are only noticeable when bimolecular recombination is very high and very variable.

5.6 Conclusions

We have developed a technique for incorporating photon recycling into back-contact cell designs and shown that, for cells under uniform illumination it is not necessary to explicitly include this for MAPbI perovskite cells. A model that has the correct effective bulk recombination will give accurate predictions of the JV curves. This increases our confidence in previous drift-diffusion equations on perovskites, and shows we can focus our attention on accurate modelling of trap state behaviour.

The relative advantages of vertical and several back-contact cells have been investigated and it is shown that in terms of internal carrier behaviour, vertical devices out-perform all back-contact designs. The most efficient back-contact cell discovered through our process was a 0.6 by 4 μm flat IBSC, achieving an efficiency of 21.4% compared to 24.2% for an optimised vertical cell. The QIBSC also showed some promise. Any optical improvement of the back-contact design would have to exceed this internal-transport penalty before switching designs becomes worthwhile.

Chapter 6

Conclusions and future work

6.1 Conclusions

In this thesis we have computationally and analytically investigated situations where we can construct simplified models of lateral carrier and photonic transport in solar cells, particularly focusing on perovskite cells. We have shown that coupling the drift-diffusion equations to photon transport within the cell need not be computationally challenging, and outlined how this helps us assess data from scanning photocurrent microscopy and the suitability of perovskite back-contact solar cells.

We firstly demonstrated that in many cases, a one-dimensional model will suffice for modelling the lateral behaviour of the solar cell, allowing for increased ease of interpreting experimental results on extended substrates. The current-extracting lower boundary condition can be replaced by an effective extraction velocity, for which we have derived appropriate analytic expressions in cases of slow extraction or for similar electron and hole diffusion constants. However we also show when this model may break down, primarily when the cell width is less than the height, or when the majority of generated carriers recombine with each other. We then apply this model to scanning photocurrent microscopy, which we would expect to require two lateral dimensions to be modelled. We show that we may analytically integrate over both lateral dimensions to generate analytic expressions for the current output and response time for a range of different physical setups.

Secondly, we investigated photon recycling in the context of one-dimensional lateral transport, and develop three models that are each suitable under different circumstances. Using the findings of the first chapter, we incorporated these into our one-dimensionalised lateral diffusion model and compare the models to device performance under scanning photocurrent microscopy. The three models we compared were two nonscattering models of differing complexity and a photon diffusion model appropriate for scattering systems. We

find that the best model includes a small degree of scattering, which is not normally included in short-range transport models.

Thirdly, we modelled different geometries of MAPbI perovskite back-contact solar cell and compared them to traditional vertical devices. We found that the vertical devices have superior internal transport properties, with a flat-based back-contact design showing the second-best characteristics. Although we anticipate that back-contacts will reduce front-surface shadowing, we would need more than 10% more light admitted to justify the manufacture. This suggests that back-contact solar cells will not offer perovskites the same degree of improvement that was found in silicon solar cells. A model for incorporating photon recycling effects into these two-dimensional models is outlined, but shown to be superfluous for the materials parameters of the perovskite cells investigated.

6.2 Future work

1. The utility of converting to a 1D model could be improved by investigating how to add the effects of applied voltages to the system. There will be fairly trivial drift effects of lateral transport, however there may also be significant height-dependent vertical fields, which will complicate the expression for extraction velocity.

2. This work is purely computational in nature and there are a number of related experiments that would clarify the applicability of its models. Chiefly needed are further studies to elucidate how light travels within a solar cell. This is complicated by the relationship between optical and electronic transport. One avenue to decouple these is to apply the models to nanocrystal films, where the conductivity can be modulated very easily. Unfortunately this may also change the optical behaviour of the film, and the findings will not necessarily be applicable to other film types. A second avenue of approach is to shine focused, sub-bandgap light into the cell and detect how much scatters out with distance. In this case, we minimise the absorption and have no secondary generation, allowing us to measure only the scattering and waveguiding. The sensitivity of this technique will depend on the film being reasonably scattering.

3. There are a large number of geometric parameters in all of the different back-contact cells that could easily affect device performance, for instance the extent of the electrodes and their separation. All of these could be investigated.

4. Having come to some conclusions as to the optimal geometries, we could couple this to full models of optical management to investigate both interference effects and the effects of a rough front surface.

5. We could also investigate how to formally incorporate the scattering model developed in chapter 4 into the 2D drift-diffusion model in chapter 5.

6. The models used in this thesis are a compromise between the specifics needed to model perovskites and the generality required to model other systems. We could adjust the models in either direction, by adding mobile dopants and full expressions for direct-indirect bandgap effects on absorption and emission characteristics for more complete perovskite models, or by making them suitable for strongly-doped systems like silicon solar cells by focusing on the minority carriers.

References

[1] Abramowitz, M. and Stegun, I. A. (1972). *Handbook of Mathematical Functions with Formulas, Graphs, and Mathematical Tables*. Dover Publications.

[2] Agarwal, S. and Nair, P. R. (2015). Device engineering of perovskite solar cells to achieve near ideal efficiency. *Applied Physics Letters*, 107(12):123901.

[3] Alvarez-Aramberri, J., Pardo, D., Paszynski, M., Collier, N., Dalcin, L., and Calo, V. M. (2012). On round-off error for adaptive finite element methods. In *Procedia Computer Science*, volume 9, pages 1474–1483.

[4] Aronson, R. and Corngold, N. (1999). Photon diffusion coefficient in an absorbing medium. *Journal of the Optical Society of America A*, 16(5):1066.

[5] Asghar, M., Zhang, J., Wang, H., and Lund, P. (2017). Device stability of perovskite solar cells – A review. *Renewable and Sustainable Energy Reviews*, 77:131–146.

[6] Ashcroft, N. W. and Mermin, N. D. (1976). Solid State Physics. *Solid-State Electronics*, 9(10):939–942.

[7] Azarhoosh, P., McKechnie, S., Frost, J. M., Walsh, A., and Van Schilfgaarde, M. (2016). Research Update: Relativistic origin of slow electron-hole recombination in hybrid halide perovskite solar cells. *APL Materials*, 4(9):091501.

[8] Babayigit, A., Ethirajan, A., Muller, M., and Conings, B. (2016). Toxicity of organometal halide perovskite solar cells. *Nature Materials*, 15(3):247–251.

[9] Badescu, V. and Landsberg, P. T. (1993). Theory of some effects of photon recycling in semiconductors. *Semiconductor Science and Technology*, 8(7):1267–1276.

[10] Balenzategui, J. and Martí, A. (2006). Detailed modelling of photon recycling: application to GaAs solar cells. *Solar Energy Materials and Solar Cells*, 90(7-8):1068–1088.

[11] Bandyopadhyay, S. (2012). *Physics of Nanostructured Solid State Devices*. Springer.

[12] Bank, R. E., Bulirsch, R., and Merten, K. (1990). *Mathematical Modelling and Simulation of Electrical Circuits and Semiconductor Devices*, volume 93. Springer Basel.

[13] Benisty, H., Stanley, R., and Mayer, M. (1998). Method of source terms for dipole emission modification in modes of arbitrary planar structures. *Journal of the Optical Society of America A*, 15(5):1192.

[14] Bhattacharya, R., Pal, B., and Bansal, B. (2012). On conversion of luminescence into absorption and the van Roosbroeck-Shockley relation. *Applied Physics Letters*, 100(22):222103.

[15] Born, M. and Wolf, E. (1999). *Principles of Optics: Electromagnetic Theory of Propagation, Interference and Diffraction of Light*.

[16] Brandt, R. E., Poindexter, J. R., Gorai, P., Kurchin, R. C., Hoye, R. L. Z., Nienhaus, L., Wilson, M. W. B., Polizzotti, J. A., Sereika, R., Žaltauskas, R., Lee, L. C., MacManus-Driscoll, J. L., Bawendi, M., Stevanović, V., and Buonassisi, T. (2017). Searching for "defect-tolerant" photovoltaic materials: combined theoretical and experimental screening. *Chemistry of Materials*, 29(11):4667–4674.

[17] Brendel, R. (2003). *Thin-Film Crystalline Silicon Solar Cells: Physics and Technology*. Wiley-VCH.

[18] Brenes, R., Guo, D., Osherov, A., Noel, N. K., Eames, C., Hutter, E. M., Pathak, S., Niroui, F., Friend, R. H., Islam, M. S., Snaith, H. J., Bulović, V., Savenije, T. J., and Stranks, S. D. (2017). Metal halide perovskite polycrystalline films exhibiting properties of single crystals. *in submission*.

[19] Brennesholtz, M. S. and Stupp, E. H. (2008). *Projection Displays, Second Edition*. John Wiley & Sons, Ltd, Chichester, UK.

[20] Brezzi, F., Marini, L. D., and Pietra, P. (1989). Two-dimensional exponential fitting and applications to drift-diffusion models. *SIAM Journal on Numerical Analysis*, 26(6):1342–1355.

[21] Brinkworth, B. J. (2002). A diffusion model of the transport of radiation from a point source in the lower atmosphere. *British Journal of Applied Physics*, 15(6):733–741.

[22] Brivio, F., Butler, K. T., Walsh, A., and van Schilfgaarde, M. (2014). Relativistic quasiparticle self-consistent electronic structure of hybrid halide perovskite photovoltaic absorbers. *Physical Review B*, 89(15):155204.

[23] Burden, R. L. and Faires, J. D. (2006). Numerical Analysis. *Princeton Companion to Mathematics*, 6(May).

[24] Byrnes, S. J. (2016). Multilayer optical calculations.

[25] Caironi, M. and Noh, Y.-Y. (2015). *Large Area and Flexible Electronics*. Wiley-VCH.

[26] Canali, C., Jacoboni, C., Nava, F., Ottaviani, G., and Alberigi-Quaranta, A. (1975). Electron drift velocity in silicon. *Physical Review B*, 12(6):2265–2284.

[27] Carrillo, J. A., Gamba, I. M., Majorana, A., and Shu, C.-W. (2003). A direct solver for 2D non-stationary Boltzmann-Poisson systems for semiconductor devices: A MESFET simulation by WENO-Boltzmann schemes. *Journal of Computational Electronics*, 2(2-4):375–380.

[28] Chen, Y., Yi, H. T., Wu, X., Haroldson, R., Gartstein, Y. N., Rodionov, Y. I., Tikhonov, K. S., Zakhidov, A., Zhu, X. Y., and Podzorov, V. (2016). Extended carrier lifetimes and diffusion in hybrid perovskites revealed by Hall effect and photoconductivity measurements. *Nature Communications*, 7:12253.

[29] Ciarlet, P. G. and Lions, J.-L. (1990). *Handbook of Numerical Analysis*. North-Holland.

[30] Crowell, C. and Sze, S. M. (1966). Current transport in metal-semiconductor barriers. *Solid-State Electronics*, 9(11-12):1035–1048.

[31] Cui, J., Yuan, H., Li, J., Xu, X., Shen, Y., Lin, H., and Wang, M. (2015). Recent progress in efficient hybrid lead halide perovskite solar cells. *Science and Technology of Advanced Materials*, 16(3):036004.

[32] Defrance, J., Lemaître, C., Ajib, R., Benedicto, J., Mallet, E., Pollès, R., Plumey, J.-P., Mihailovic, M., Centeno, E., Ciracì, C., Smith, D., and Moreau, A. (2016). Moosh: A Numerical Swiss Army Knife for the Optics of Multilayers in Octave/Matlab. *Journal of Open Research Software*, 4(1).

[33] Deinega, A. and John, S. (2012). Finite difference discretization of semiconductor drift-diffusion equations for nanowire solar cells. *Computer Physics Communications*, 183:2128–2135.

[34] DeQuilettes, D. W., Koch, S., Burke, S., Paranji, R. K., Shropshire, A. J., Ziffer, M. E., and Ginger, D. S. (2016). Photoluminescence lifetimes exceeding 8 μs and quantum yields exceeding 30% in hybrid perovskite thin films by ligand passivation. *ACS Energy Letters*, 1(2):438–444.

[35] Dhanker, R., Brigeman, A. N., Larsen, A. V., Stewart, R. J., Asbury, J. B., and Giebink, N. C. (2014). Random lasing in organo-lead halide perovskite microcrystal networks. *Applied Physics Letters*, 105(15):151112.

[36] Dicker, J., Sölter, J., Schumacher, J. O., Glunz, S. W., and Warta, W. (2000). Analysis of rear contacted solar cell structures for cost-effective processes and materials. 2000-Janua:387–390.

[37] Dong, Q., Fang, Y., Shao, Y., Mulligan, P., Qiu, J., Cao, L., and Huang, J. (2015). Electron-hole diffusion lengths > 175 m in solution-grown $CH_3NH_3PbI_3$ single crystals. *Science*, 347(6225):967–970.

[38] Dudko, O. K. and Weiss, G. H. (2005). Photon diffusion in biological tissues. *Diffusion Fundamentals*.

[39] Dumke, W. P. (1957). Spontaneous radiative recombination in semiconductors. *Physical Review*, 105(1):139–144.

[40] Durbin, S. and Gray, J. (1994). Numerical modeling of photon recycling in solar cells. *IEEE Transactions on Electron Devices*, 41(2):239–245.

[41] Durduran, T., Yodh, A. G., Chance, B., and Boas, D. A. (1997). Does the photon-diffusion coefficient depend on absorption? *Journal of the Optical Society of America A*, 14(12):3358.

[42] Durian, D. J. (1998). The diffusion coefficient depends on absorption. *Optics Letters*, 23(19):1502.

[43] Eames, C., Frost, J. M., Barnes, P. R. F., O'Regan, B. C., Walsh, A., and Islam, M. S. (2015). Ionic transport in hybrid lead iodide perovskite solar cells. *Nature Communications*, 6(May):7497.

[44] Edri, E., Kirmayer, S., Mukhopadhyay, S., Gartsman, K., Hodes, G., and Cahen, D. (2014). Elucidating the charge carrier separation and working mechanism of CH3NH3PbI(3-x)Cl(x) perovskite solar cells. *Nature Communications*, 5:3461.

[45] Eyderman, S. and John, S. (2016). Light-trapping and recycling for extraordinary power conversion in ultra-thin gallium-arsenide solar cells. *Scientific Reports*, 6(1):28303.

[46] Fang, Y., Wei, H., Dong, Q., and Huang, J. (2017). Quantification of re-absorption and re-emission processes to determine photon recycling efficiency in perovskite single crystals. *Nature communications*, 8:14417.

[47] Flämmich, M., Gather, M. C., Danz, N., Michaelis, D., Bräuer, A. H., Meerholz, K., and Tünnermann, A. (2010). Orientation of emissive dipoles in OLEDs: Quantitative in situ analysis. *Organic Electronics*, 11(6):1039–1046.

[48] Fournié, M. (2000). High order conservative difference methods for 2D drift-diffusion model on non-uniform grid. *Applied Numerical Mathematics*, 33(1-4):381–392.

[49] Fowles, G. R. (1968). Introduction to Modern Optics. *American Journal of Physics*, 36(8):770.

[50] Frost, J. M., Butler, K. T., Brivio, F., Hendon, C. H., van Schilfgaarde, M., and Walsh, A. (2014). Atomistic origins of high-performance in hybrid halide perovskite solar cells. *Nano Letters*, 14(5):2584–90.

[51] Furutsu, K. and Yamada, Y. (1994). Diffusion approximation for a dissipative random medium and the applications. *Physical Review E*, 50(5):3634–3640.

[52] Geissbuhler, J., Wolf, S. D., Faes, A., Badel, N., Jeangros, Q., Tomasi, A., Barraud, L., Descoeudres, A., Despeisse, M., and Ballif, C. (2014). Silicon Heterojunction Solar Cells With Copper-Plated Grid Electrodes: Status and Comparison With Silver Thick-Film Techniques. *IEEE Journal of Photovoltaics*, 4(4):1055–1062.

[53] Giorgi, G., Fujisawa, J.-I., Segawa, H., and Yamashita, K. (2013). Small Photocarrier Effective Masses Featuring Ambipolar Transport in Methylammonium Lead Iodide Perovskite: A Density Functional Analysis. *The Journal of Physical Chemistry Letters*, 4(24):4213–4216.

[54] Giustino, F. and Snaith, H. J. (2016). Toward lead-free perovskite solar cells. *ACS Energy Letters*, 1(6):1233–1240.

[55] Graaff, R. and Ten Bosch, J. J. (2000). Diffusion coefficient in photon diffusion theory. *Optics Letters*, 25(1):43.

[56] Gradshtein, I. S., Moiseevich, R. I., and Jeffrey, A. (2000). *Table of Integrals, Series, and Products*. Academic Press.

[57] Graham, R. and Yu, D. (2013). Scanning photocurrent microscopy in semiconductor nanostructures. *Modern Physics Letters B*, 27(25):1330018.

[58] Green, M. A., Emery, K., Hishikawa, Y., Warta, W., Dunlop, E. D., Levi, D. H., and Ho-Baillie, A. W. Y. (2017). Solar cell efficiency tables (version 49). *Progress in Photovoltaics: Research and Applications*, 25(1):3–13.

[59] Green, M. A., Ho-Baillie, A., and Snaith, H. J. (2014). The emergence of perovskite solar cells. *Nature Photonics*, 8(7):506–514.

[60] Guerrero-Lemus, R., Vega, R., Kim, T., Kimm, A., and Shephard, L. E. (2016). Bifacial solar photovoltaics - A technology review.

[61] Hall, R. N. (1952). Electron-Hole Recombination in Germanium. *Physical Review*, 87(2):387–387.

[62] Hangarter, C. M., Hamadani, B. H., Guyer, J. E., Xu, H., Need, R., and Josell, D. (2011). Three dimensionally structured interdigitated back contact thin film heterojunction solar cells. *Journal of Applied Physics*, 109(7).

[63] Herz, L. M. (2017). Charge-carrier mobilities in metal halide perovskites: fundamental mechanisms and limits. *ACS Energy Letters*, pages 1539–1548.

[64] Hu, Z., Kapil, G., Shimazaki, H., Pandey, S. S., Ma, T., and Hayase, S. (2017). Transparent conductive oxide layer and hole selective layer free back-contacted hybrid perovskite solar cell. *Journal of Physical Chemistry C*, 121(8):4214–4219.

[65] Hubner, A., Aberle, A. G., and Hezel, R. (1997). Novel cost-effective bifacial silicon solar cells with 19.4% front and 18.1% rear efficiency. *Applied Physics Letters*, 70(8):1008.

[66] Hutter, E. M., Gélvez-Rueda, M. C., Osherov, A., Bulović, V., Grozema, F. C., Stranks, S. D., and Savenije, T. J. (2016). Direct-indirect character of the bandgap in methylammonium lead iodide perovskite. *Nature materials*.

[67] Ihara, T., Maruyama, S., Yoshita, M., Akiyama, H., Pfeiffer, L. N., and West, K. W. (2009). Thermal-equilibrium relation between the optical emission and absorption spectra of a doped semiconductor quantum well. *Physical Review B - Condensed Matter and Materials Physics*, 80(3).

[68] Jeon, N. J., Noh, J. H., Yang, W. S., Kim, Y. C., Ryu, S., Seo, J., and Seok, S. I. (2015). Compositional engineering of perovskite materials for high-performance solar cells. *Nature*, 517(7535):476–480.

[69] Johnsson, M. and Lemmens, P. (2007). *Crystallography and Chemistry of Perovskites*.

[70] Jumabekov, A., Della Gaspera, E., Xu, Z.-q., Chesman, A., van Embden, J., Bonke, S., Bao, Q., Vak, D., and Bach, U. (2016). Back-contacted hybrid organic-inorganic perovskite solar cells. *Journal of Materials Chemistry C*, 4(15):3125–3130.

[71] Jungel, A. (2009). *Transport Equations for Semiconductors*, volume 773 of *Lecture Notes in Physics*. Springer Berlin Heidelberg, Berlin, Heidelberg.

[72] Kabra, D. and Narayan, K. S. (2007). Direct estimate of transport length scales in semiconducting polymers. *Advanced Materials*, 19(11):1465–1470.

[73] Kabra, D., Shriram, S., Vidhyadhiraja, N. S., and Narayan, K. S. (2007). Charge carrier dynamics in organic semiconductors by position dependent optical probing. *Journal of Applied Physics*, 101(6):064510.

[74] Kamat, P. V., Bisquert, J., and Buriak, J. (2017). Lead-free perovskite solar cells. *ACS Energy Letters*, 2(4):904–905.

[75] Kang, K., Lee, Y., Kim, J., Lee, H., and Yang, B. (2016). A generalized Fabry-Perot formulation for optical modeling of organic light-emitting diodes considering the dipole orientation and light polarization. *IEEE Photonics Journal*, 8(2):1–19.

[76] Katsidis, C. C. and Siapkas, D. I. (2002). General transfer-matrix method for optical multilayer systems with coherent, partially coherent, and incoherent interference. *Applied Optics*, 41(19):3978.

[77] Kim, J., Lee, S.-H., Lee, J. H., and Hong, K.-H. (2014). The role of intrinsic defects in methylammonium lead iodide perovskite. *The Journal of Physical Chemistry Letters*, 5(8):1312–1317.

[78] Kirchartz, T., Staub, F., and Rau, U. (2016). Impact of photon-recycling on the open-circuit voltage of metal halide perovskite solar cells. *ACS Energy Lett.*, 1(4):731–739.

[79] Klug, M. T., Osherov, A., Haghighirad, A. A., Stranks, S. D., Brown, P. R., Bai, S., Wang, J. T.-W., Dang, X., Bulović, V., Snaith, H. J., Belcher, A. M., Wen, T.-C., Ginger, D. S., Friend, R. H., Snaith, H. J., Sutton, R. J., Ma, W., Moghadam, F., Conings, B., Babayigit, A., Boyen, H.-G., Bent, S., Giustino, F., Herz, L. M., Johnston, M. B., McGehee, M. D., and Snaith, H. J. (2017). Tailoring metal halide perovskites through metal substitution: influence on photovoltaic and material properties. *Energy Environ. Sci.*, 10(1):236–246.

[80] Kluska, S., Granek, F., Rüdiger, M., Hermle, M., and Glunz, S. W. (2010). Modeling and optimization study of industrial n-type high-efficiency back-contact back-junction silicon solar cells. *Solar Energy Materials and Solar Cells*, 94(3):568–577.

[81] Kojima, A., Teshima, K., Shirai, Y., and Miyasaka, T. (2008). Novel photoelectrochemical cell with mesoscopic electrodes sensitized by lead-halide compounds (11). *214th ECS Meeting*, MA2008-02(1):27.

[82] Kojima, A., Teshima, K., Shirai, Y., and Miyasaka, T. (2009). Organometal halide perovskites as visible-light sensitizers for photovoltaic cells. *Journal of the American Chemical Society*, 131(17):6050–6051.

[83] Kuan-Ying Ho, Chung-Yu Hong, Peichen Yu, and Yuh-Renn Wu (2015). Optimization of all-back-contact GaAs solar cells. In *2015 International Conference on Numerical Simulation of Optoelectronic Devices (NUSOD)*, pages 143–144. IEEE.

[84] Kuriyama, T., Kamiya, T., and Yanai, H. (1977). Effect of photon recycling on diffusion length and internal quantum efficiency in AlxGa1–xAs-GaAs heterostructures. *Japanese Journal of Applied Physics*, 16(3):465–477.

[85] Lai, M. L., Tay, T. Y. S., Sadhanala, A., Dutton, S. E., Li, G., Friend, R. H., and Tan, Z. K. (2016). Tunable near-infrared luminescence in tin halide perovskite devices. *Journal of Physical Chemistry Letters*, 7(14):2653–2658.

[86] Laks, D. B., Neumark, G. F., and Pantelides, S. T. (1990). Accurate interband-Auger-recombination rates in silicon. *Physical Review B*, 42(8):5176–5185.

[87] Lammert, M. D. and Schwartz, R. J. (1977). The interdigitated back contact solar cell: a silicon solar cell for use in concentrated sunlight. *IEEE Transactions on Electron Devices*, ED-24(4):337–342.

[88] Lee, J.-W., Kim, S.-G., Bae, S.-H., Lee, D.-K., Lin, O., Yang, Y., and Park, N.-G. (2017). The interplay between trap density and hysteresis in planar heterojunction perovskite solar cells. *Nano Letters*, 17(7):4270–4276.

[89] Lee, S.-W., Kim, C.-H., Lee, S.-G., Jeong, J.-H., Choi, J.-H., and Lee, E.-S. (2013). Mobility improvement of P3HT thin film by high-voltage electrostatic field-assisted crystallization. *Electronic Materials Letters*, 9(4):471–476.

[90] Leo, K. (2015). Perovskite photovoltaics: Signs of stability. *Nature Nanotechnology*, 10(7):574–575.

[91] LeVeque, R. J. (2007). *Finite Difference Methods for Ordinary and Partial Differential Equations*. Society for Industrial and Applied Mathematics.

[92] Libbrecht, K. G., Black, E. D., and Hirata, C. M. (2003). A basic lock-in amplifier experiment for the undergraduate laboratory. *American Journal of Physics*, 71(11):1208–1213.

[93] Lin, Q., Armin, A., Nagiri, R. C. R., Burn, P. L., and Meredith, P. (2014). Electro-optics of perovskite solar cells. *Nature Photonics*, 9(2):106–112.

[94] Liu, T., Zong, Y., Zhou, Y., Yang, M., Li, Z., Game, O. S., Zhu, K., Zhu, R., Gong, Q., and Padture, N. P. (2017). High-performance formamidinium-based perovskite solar cells via microstructure-mediated delta-to-alpha phase transformation. *Chemistry of Materials*, 29(7):3246–3250.

[95] Lombardo, C. J., Glaz, M. S., Ooi, Z.-E., Vanden Bout, D. A., and Dodabalapur, A. (2012). Scanning photocurrent microscopy of lateral organic bulk heterojunctions. *Physical Chemistry Chemical Physics*, 14(38):13199.

[96] Löper, P., Stuckelberger, M., Niesen, B., Werner, J., Filipič, M., Moon, S.-J., Yum, J.-H., Topič, M., De Wolf, S., and Ballif, C. (2015). Complex refractive index spectra of CH 3 NH 3 PbI 3 perovskite thin films determined by spectroscopic ellipsometry and spectrophotometry. *The Journal of Physical Chemistry Letters*, 6(1):66–71.

[97] Lu, M., Das, U., Bowden, S., Hegedus, S., and Birkmire, R. (2011). Optimization of interdigitated back contact silicon heterojunction solar cells: Tailoring hetero-interface band structures while maintaining surface passivation. *Progress in Photovoltaics: Research and Applications*, 19(3):326–338.

[98] Lumb, M. P., Bailey, C. G., Adams, J. G., Hillier, G., Tuminello, F., Elarde, V. C., and Walters, R. J. (2013). Extending the 1-d Hovel model for coherent and incoherent back reflections in homojunction solar cells. *IEEE Journal of Quantum Electronics*, 49(5):462–470.

[99] Lumb, M. P., Steiner, M. A., Geisz, J. F., and Walters, R. J. (2014). Incorporating photon recycling into the analytical drift-diffusion model of high efficiency solar cells. *Journal of Applied Physics*, 116(19):194504.

[100] Maezawa, H. and Miyauchi, H. (2009). Rigorous expressions for the Fresnel equations at interfaces between absorbing media. *Journal of the Optical Society of America A*, 26(2):330.

[101] Markvart, T. (2016). From steam engine to solar cells: can thermodynamics guide the development of future generations of photovoltaics? *Wiley Interdisciplinary Reviews: Energy and Environment*, 5(5):543–569.

[102] Martí, A., Balenzategui, J. L., and Reyna, R. (1997). Photon recycling and Shockley's diode equation. *Journal of Applied Physics*, 82(8):4067–4075.

[103] Mat Desa, M., Sapeai, S., Azhari, A., Sopian, K., Sulaiman, M., Amin, N., and Zaidi, S. (2016). Silicon back contact solar cell configuration: A pathway towards higher efficiency. *Renewable and Sustainable Energy Reviews*, 60:1516–1532.

[104] MATLAB (2017). *Partial Differential Equation Toolbox User's Guide*. R2017a edition.

[105] Mauri, A., Bortolossi, A., Novielli, G., and Sacco, R. (2015). 3D finite element modeling and simulation of industrial semiconductor devices including impact ionization. *Journal of Mathematics in Industry*, 5(1):1–18.

[106] Miller, O. D., Yablonovitch, E., and Kurtz, S. R. (2012). Strong internal and external luminescence as solar cells approach the Shockley-Queisser limit. *IEEE Journal of Photovoltaics*, 2(3):303–311.

[107] Mitalas, R. and Sills, K. R. (1992). On the photon diffusion time scale for the sun. *The Astrophysical Journal*, 401:759.

[108] Mitsas, C. L. and Siapkas, D. I. (1995). Generalized matrix method for analysis of coherent and incoherent reflectance and transmittance of multilayer structures with rough surfaces, interfaces, and finite substrates. *Applied Optics*, 34(10):1678.

[109] Moulin, E., Müller, T. C. M., Warzechac, M., Hoffmann, A., Paetzold, U. W., and Aeberhard, U. (2015). Highly transparent front electrodes with metal fingers for p-i-n thin-film silicon solar cells. *EPJ Photovoltaics*, 6(60501):60501.

[110] Mukhopadhyay, S., Das, A. J., and Narayan, K. S. (2013). High-resolution photocurrent imaging of bulk heterojunction solar cells. *The Journal of Physical Chemistry Letters*, 4(1):161–169.

[111] Mukhopadhyay, S. and Narayan, K. S. (2012). Rationalization of donor-acceptor ratio in bulk heterojunction solar cells using lateral photocurrent studies. *Applied Physics Letters*, 100(16):163302.

[112] Nachaoui, A. (1999). Iterative solution of the drift–diffusion equations. *Numerical Algorithms*, 21:323–341.

[113] Neamen, D. A. (2003). *Semiconductor Physics and Devices: Basic Principles*. McGraw-Hill, 3rd edition.

[114] Nelson, J. (2003). *The Physics of Solar Cells*. Imperial College Press.

[115] Neyts, K. A. (1998). Simulation of light emission from thin-film microcavities. *Journal of the Optical Society of America A*, 15(4):962.

[116] NREL (1999). Solar Spectral Irradiance: Air Mass 1.5.

[117] NREL (2017). Best research-cell efficiencies.

[118] O'Kane, S. E. J., Richardson, G., Pockett, A., Niemann, R. G., Cave, J. M., Sakai, N., Eperon, G. E., Snaith, H. J., Foster, J. M., Cameron, P. J., and Walker, A. B. (2017). Measurement and modelling of dark current decay transients in perovskite solar cells. *J. Mater. Chem. C*, 5(2):452–462.

[119] Padilha, L. A., Stewart, J. T., Sandberg, R. L., Bae, W. K., Koh, W.-K., Pietryga, J. M., and Klimov, V. I. (2013). Carrier multiplication in semiconductor nanocrystals: influence of size, shape, and composition. *Accounts of Chemical Research*, 46(6):1261–1269.

[120] Paradisi, P., Cesari, R., Mainardi, F., and Tampieri, F. (2001). The fractional Fick's law for non-local transport processes. *Physica A: Statistical Mechanics and its Applications*, 293(1):130–142.

[121] Parks, J. W., Brennan, K. F., and Smith, A. W. (1997). Two-dimensional model of photon recycling in direct gap semiconductor devices. *Journal of Applied Physics*, 82(7):3493–3498.

[122] Parrott, J. (1993). Radiative recombination and photon recycling in photovoltaic solar cells. *Solar Energy Materials and Solar Cells*, 30(3):221–231.

[123] Pazos-Outon, L. M., Szumilo, M., Lamboll, R., Richter, J. M., Crespo-Quesada, M., Abdi-Jalebi, M., Beeson, H. J., Vrucinic, M., Alsari, M., Snaith, H. J., Ehrler, B., Friend, R. H., and Deschler, F. (2016). Photon recycling in lead iodide perovskite solar cells. *Science*, 351(6280):1430–1433.

[124] Pelant, I. and Valenta, J. (2012). *Luminescence Spectroscopy of Semiconductors*. Oxford University Press.

[125] Poindexter, J. R., Hoye, R. L. Z., Nienhaus, L., Kurchin, R. C., Morishige, A. E., Looney, E. E., Osherov, A., Correa-Baena, J.-P., Lai, B., Bulović, V., Stevanović, V., Bawendi, M. G., and Buonassisi, T. (2017). High tolerance to iron contamination in lead halide perovskite solar cells. *ACS Nano*.

[126] Rau, U. (2007). Reciprocity relation between photovoltaic quantum efficiency and electroluminescent emission of solar cells. *Physical Review B*, 76(8):085303.

[127] Rau, U., Paetzold, U. W., and Kirchartz, T. (2014). Thermodynamics of light management in photovoltaic devices. *Physical Review B*, 90(3):035211.

[128] Rhee, J. H., Chung, C.-C., and Diau, E. W.-G. (2013). A perspective of mesoscopic solar cells based on metal chalcogenide quantum dots and organometal-halide perovskites. *NPG Asia Materials*, 5(10):e68.

[129] Richardson, G., O'Kane, S. E. J., Niemann, R. G., Peltola, T. A., Foster, J. M., Cameron, P. J., and Walker, A. B. (2016). Can slow-moving ions explain hysteresis in the current–voltage curves of perovskite solar cells? *Energy Environ. Sci.*, 9(4):1476–1485.

[130] Richter, J. M., Abdi-Jalebi, M., Sadhanala, A., Tabachnyk, M., Rivett, J. P., Pazos-Outón, L. M., Gödel, K. C., Price, M., Deschler, F., and Friend, R. H. (2016). Enhancing photoluminescence yields in lead halide perovskites by photon recycling and light outcoupling. *Nature Communications*, 7:13941.

[131] Riley, K. F., Hobson, M. P., and Bence, S. J. (2006). *Mathematical Methods For Physics and Engineering*. Cambridge University Press.

[132] Riordan, C. and Hulstron, R. (1990). What is an air mass 1.5 spectrum? *IEEE Conference on Photovoltaic Specialists*, pages 1085–1088.

[133] Ross, R. T. (1967). Some thermodynamics of photochemical systems. *The Journal of Chemical Physics*, 46(12):4590.

[134] Ruhle, S. (2016). Tabulated values of the Shockley–Queisser limit for single junction solar cells. *Solar Energy*, 130:139–147.

[135] Ruzicka, B. A., Werake, L. K., Samassekou, H., and Zhao, H. (2010). Ambipolar diffusion of photoexcited carriers in bulk GaAs. *Applied Physics Letters*, 97(26):262119.

[136] Sah, C.-T. (1991). *Fundamentals of Solid State Electronics*, volume 1. World Scientific Publishing Company.

[137] Savenije, T. J., Ponseca, C. S., Kunneman, L., Abdellah, M., Zheng, K., Tian, Y., Zhu, Q., Canton, S. E., Scheblykin, I. G., Pullerits, T., Yartsev, A., and Sundström, V. (2014). Thermally activated exciton dissociation and recombination control the carrier dynamics in organometal halide perovskite. *The Journal of Physical Chemistry Letters*, 5(13):2189–2194.

[138] Scharfetter, D. and Gummel, H. (1969). Large-signal analysis of a silicon Read diode oscillator. *IEEE Transactions on Electron Devices*, 16(1):64–77.

[139] Schnitzer, I., Yablonovitch, E., Caneau, C., Gmitter, T. J., and Scherer, A. (1993). 30% external quantum efficiency from surface textured, thin-film light-emitting diodes. *Applied Physics Letters*, 63(16):2174–2176.

[140] Seeger, K. (1973). *Semiconductor Physics: an Introduction*. Springer-Verlag.

[141] Seo, J., Noh, J. H., and Seok, S. I. (2016). Rational strategies for efficient perovskite solar cells.

[142] Service, R. F. (2016). Perovskite solar cells gear up to go commercial. *Science*, 354(6317).

[143] Shao, Y., Xiao, Z., Bi, C., Yuan, Y., and Huang, J. (2014). Origin and elimination of photocurrent hysteresis by fullerene passivation in CH3NH3PbI3 planar heterojunction solar cells. *Nature Communications*, 5:5784.

[144] Shi, D., Adinolfi, V., Comin, R., Yuan, M., Alarousu, E., Buin, A., Chen, Y., Hoogland, S., Rothenberger, A., Katsiev, K., Losovyj, Y., Zhang, X., Dowben, P. A., Mohammed, O. F., Sargent, E. H., and Bakr, O. M. (2015). Low trap-state density and long carrier diffusion in organolead trihalide perovskite single crystals. *Science*, 347(6221):519–522.

[145] Shockley, W. and Queisser, H. J. (1961). Detailed balance limit of efficiency of p-n junction solar cells. *Journal of Applied Physics*, 32(3):510.

[146] Shockley, W. and Read, W. T. (1952). Statistics of the recombinations of holes and electrons. *Physical Review*, 87(5):835–842.

[147] Snaith, H. J. (2013). Perovskites: the emergence of a new era for low cost high efficiency solar cells. *The Journal of Physical Chemistry Letters*.

[148] Snaith, H. J., Abate, A., Ball, J. M., Eperon, G. E., Leijtens, T., Noel, N. K., Stranks, S. D., Wang, J. T.-W., Wojciechowski, K., and Zhang, W. (2014). Anomalous hysteresis in perovskite solar cells. *The Journal of Physical Chemistry Letters*, 5(9):1511–1515.

[149] Steiner, M. A., Geisz, J. F., García, I., Friedman, D. J., Duda, A., and Kurtz, S. R. (2013). Optical enhancement of the open-circuit voltage in high quality GaAs solar cells. *Journal of Applied Physics*, 113(12):123109.

[150] Stranks, S. D., Eperon, G. E., Grancini, G., Menelaou, C., Alcocer, M. J. P., Leijtens, T., Herz, L. M., Petrozza, A., and Snaith, H. J. (2013). Electron-hole diffusion lengths exceeding 1 micrometer in an organometal trihalide perovskite absorber. *Science (New York, N.Y.)*, 342(6156):341–4.

[151] Sun, X., Asadpour, R., Nie, W., Mohite, A. D., and Alam, M. A. (2015). A physics-based analytical model for perovskite solar cells. *IEEE Journal of Photovoltaics*, 5(5):1389–1394.

[152] Syzgantseva, O. A., Saliba, M., Grätzel, M., and Rothlisberger, U. (2017). Stabilization of the perovskite phase of formamidinium lead triiodide by methylammonium, Cs, and/or Rb doping. *The Journal of Physical Chemistry Letters*, 8(6):1191–1196.

[153] Szabo, B. A. and Babuska, I. (1991). *Finite Element Analysis*. New Age International (P) Ltd., Publishers.

[154] Sze, S. M. (1985). *Semiconductor Devices, Physics and Technology*. Wiley.

[155] Tan, G.-L., Yuan, X.-L., Zhang, Q.-M., Ku, W., and Shey, A.-J. (1989). Two-dimensional semiconductor device analysis based on new finite-element discretization employing the S-G scheme. *IEEE Transactions on Computer-Aided Design of Integrated Circuits and Systems*, 8(5):468–478.

[156] Tan, Z.-K., Moghaddam, R. S., Lai, M. L., Docampo, P., Higler, R., Deschler, F., Price, M., Sadhanala, A., Pazos, L. M., Credgington, D., Hanusch, F., Bein, T., Snaith, H. J., and Friend, R. H. (2014). Bright light-emitting diodes based on organometal halide perovskite. *Nature Nanotechnology*, 9(9):687–692.

[157] Ubrig, N., Jo, S., Berger, H., Morpurgo, A. F., and Kuzmenko, A. B. (2014). Scanning photocurrent microscopy reveals electron-hole asymmetry in ionic liquid-gated WS2 transistors. *Applied Physics Letters*, 104(17):171112.

[158] Van Kerschaver, E. and Beaucarne, G. (2006). Back-contact solar cells: a review. *Progress in Photovoltaics: Research and Applications*, 14(2):107–123.

[159] van Reenen, S., Kemerink, M., and Snaith, H. J. (2015). Modeling anomalous hysteresis in perovskite solar cells. *The Journal of Physical Chemistry Letters*, 6(19):3808–3814.

[160] van Roosbroeck, W. and Shockley, W. (1954). Photon-radiative recombination of electrons and holes in germanium. *Physical Review*, 94(6):1558–1560.

[161] Vasileska, D. and Goodnick, S. M. (2006). *Computational Electronics : Semiclassical and Quantum Device Modeling and Simulation*. Number 1. CRC Press.

[162] Vasileska, D. and Goodnick, S. M. (2011). *Nano-electronic Devices : Semiclassical and Quantum Transport Modeling*. Springer.

[163] Volovichev, I., Velázquez-Pérez, J., and Gurevich, Y. (2009). Transport boundary conditions for solar cells. *Solar Energy Materials and Solar Cells*, 93(1):6–10.

[164] Walker, A. W., Hohn, O., Micha, D. N., Blasi, B., Bett, A. W., and Dimroth, F. (2015). Impact of photon recycling on GaAs solar cell designs. *IEEE Journal of Photovoltaics*, 5(6):1636–1645.

[165] Wang, X., Khan, M. R., Gray, J. L., Alam, M. A., and Lundstrom, M. S. (2013). Design of GaAs solar cells operating close to the Shockley–Queisser limit. *IEEE Journal of Photovoltaics*, 3(2):737–744.

[166] Weber, H. (2014). The Fresnel equations for lossy dielectrics and conservation of energy. *Journal of Modern Optics*, 61(15):1219–1224.

[167] Yablonovitch, E. (1982). Statistical ray optics. *J. Opt. Soc. Am*, 72(7).

[168] Yablonovitch, E., Miller, O. D., and Kurtz, S. R. (2012). The opto-electronic physics that broke the efficiency limit in solar cells. In *2012 38th IEEE Photovoltaic Specialists Conference*, pages 001556–001559. IEEE.

[169] Yang, Y. and You, J. (2017). Make perovskite solar cells stable. *Nature*, 544(7649):155–156.

[170] Yin, W.-J., Shi, T., and Yan, Y. (2014). Unusual defect physics in CH3NH3PbI3 perovskite solar cell absorber. *Applied Physics Letters*, 104(6):063903.

[171] Yoo, K., Liu, F., and Alfano, R. (1990). When does the diffusion approximation fail to describe photon transport in random media? *Physical review letters*, 64(22):2647–2650.

[172] Yu, Z. G. (2017). Rashba effect and indirect electron-hole recombination in hybrid organic-inorganic perovskites. *Physical Chemistry Chemical Physics*.

[173] Zakutayev, A., Caskey, C. M., Fioretti, A. N., Ginley, D. S., Vidal, J., Stevanovic, V., Tea, E., and Lany, S. (2014). Defect tolerant semiconductors for solar energy conversion. *The Journal of Physical Chemistry Letters*, 5(7):1117–1125.

[174] Zhou, Y., Yang, M., Pang, S., Zhu, K., and Padture, N. P. (2016). Exceptional morphology-preserving evolution of formamidinium lead triiodide perovskite thin films via organic-cation displacement. *Journal of the American Chemical Society*, 138(17):5535–5538.

[175] Zhu, H., Trinh, M. T., Wang, J., Fu, Y., Joshi, P. P., Miyata, K., Jin, S., and Zhu, X. Y. (2017). Organic cations might not be essential to the remarkable properties of band edge carriers in lead halide perovskites. *Advanced Materials*, 29(1).

[176] Zin, N., Blakers, A., McIntosh, K. R., Franklin, E., Kho, T., Chern, K., Wong, J., Mueller, T., Aberle, A. G., Yang, Y., Zhang, X., Feng, Z., Huang, Q., and Verlinden, P. J. (2013). Continued development of all-back-contact silicon wafer solar cells at ANU. *Energy Procedia*, 33:50–63.

Chapter 7

Appendix 1: Linear fit error analysis

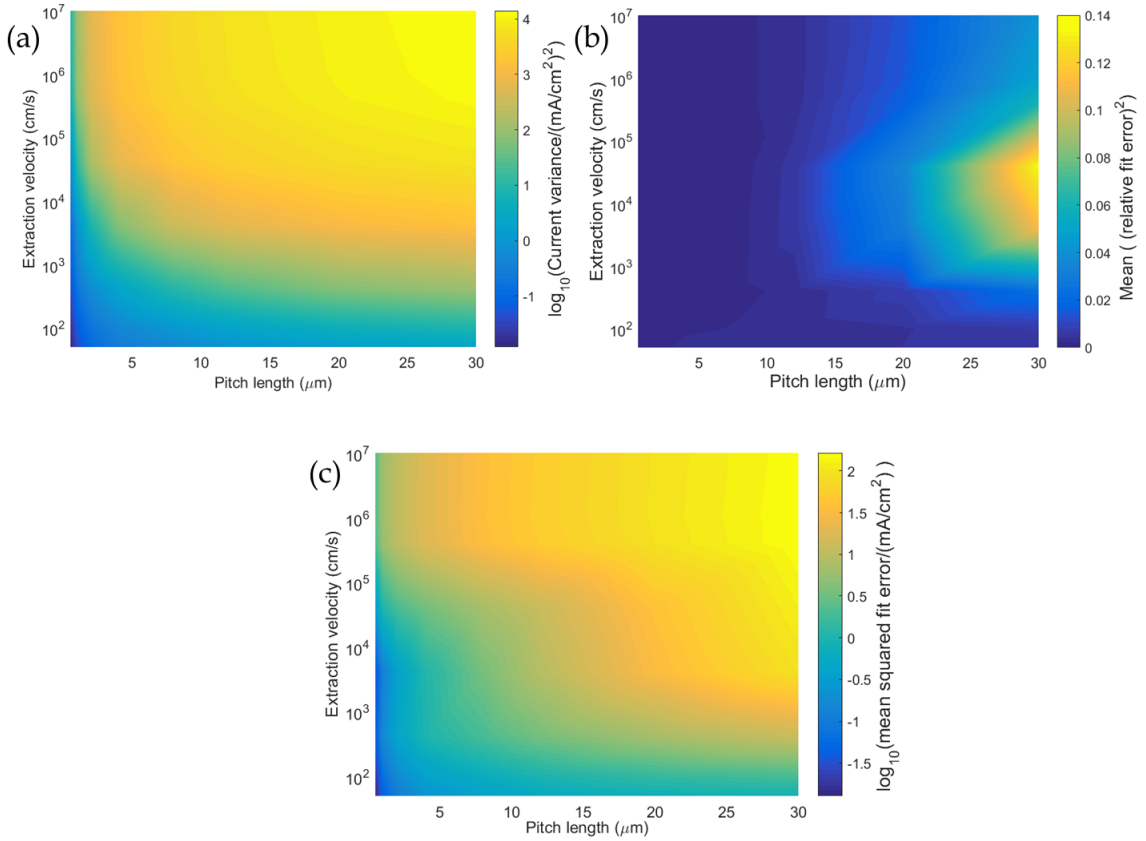

Fig. 7.1 (a): The variance in the current entering one electrode as a function of the distance along the electrode, plotted against the pitch length of the system and the extraction velocity at that electrode. (b): Mean squared relative error between the linear fit to the current density and the actual current density. (c): the absolute values of the error in (b).

Appendix 1: Linear fit error analysis

When considering the R^2 values for the goodness of the linear fit to the carrier density-current curves, we should be aware of the different components that influence this value. In practical applications, a poor R^2 alongside a low variability of both carrier density and current may be irrelevant: in many simulations, only the absolute error may be of interest. Figure 7.1a plots the current variance across an electrode. We see that this increases for larger systems and for systems with faster extraction. This means that these systems can 'afford' higher absolute errors before developing lower R^2 values.

Figure 7.1b simply plots the mean squared proportional error in the current fit, defined as

$$\langle \Delta J_R \rangle \equiv \left\langle \frac{(J(x) - qv_{1D}n(x))^2}{J(x)} \right\rangle.$$

We see that this increases with pitch distance too. The change in relative error is non-monotonic as we increase the extraction velocity, but there is a mild tendency for it to increase.

$$R^2 = 1 - \frac{\sum(J - qv_{1D}n)^2)}{\sum(J - \langle J \rangle)^2},$$

so R^2 does not depend on the relative error, but on the absolute error, shown in Figure 7.1c, divided by the variance in current. This shows monotonic behaviour, on the whole a similar pattern to the variance but with a smaller change. As the variation in current variance is larger than the variation in relative fit error, this consideration dominates R^2, however considering the relative fit error alone, we see that this will be worse for very large systems, becoming unreliable when the pitch distance is around a hundred times the film thickness.

Chapter 8

Appendix 2: Equilibration time relation for different lock-in amplifiers

The equilibration time, t_{eq}, described in the text, is similar to but not quite the value of the measured phase offset multiplied by the period of the lock-in amplifier. We will here derive the precise relationship between these two values for two different lock-in amplifier waveforms. We will assume the system becomes arbitrarily close to equilibrium after time T, which is much shorter than the period of the modulating waveform of the lock-in amplifier.

The phase delay in a signal, $f(t)$, detected by the lock-in is given by

$$\Phi = \arctan\left(\frac{S_{qu}}{S_{in}}\right) \tag{8.1}$$

for the signals modulated in-phase and in quadrature, S_{qu} and S_{in} respectively. We assume the signal has a maximum value of (approximately) $f_m = f(T)$ and behaves linearly so that after the light is chopped at time T_P, we have $f(T_P + t) = f_m - f(t)$.

If the waveform is sinusoidal, we may express

$$S_{qu} = \int_0^{2T_P} f\cos\left(\frac{\pi t}{T_P}\right) dt \tag{8.2}$$

$$= \int_0^{T} f\cos\left(\frac{\pi t}{T_P}\right) dt + \int_T^{T_P} f_m\cos\left(\frac{\pi t}{T_P}\right) dt - \int_0^{T} (f_m - f)\cos\left(\frac{\pi t}{T_P}\right) dt \tag{8.3}$$

$$= 2\int_0^{T} f\cos\left(\frac{\pi t}{T}\right) dt - 2f_m\frac{T_P}{\pi}\sin\left(\frac{\pi T}{T_P}\right) \tag{8.4}$$

$$S_{in} = \int_0^{2T_P} f \sin\left(\frac{\pi t}{T_P}\right) dt \tag{8.5}$$

$$= 2\int_0^{T} f \sin\left(\frac{\pi t}{T_P}\right) dt + 2f_m \frac{T_P}{\pi} \cos\left(\frac{\pi T}{T_P}\right) \tag{8.6}$$

Therefore, after Taylor expanding all trigonometric expressions and discarding small terms, equation 8.1 gives us

$$\Phi \approx \pi \frac{\int_0^T f dt - f_m T}{T_P f_m}. \tag{8.7}$$

$$\Rightarrow \frac{2T_P \Phi}{2\pi} \approx t_{eq}. \tag{8.8}$$

Applying a similar process to a square wave function, we instead obtain

$$S_{qu} = \int_0^{T_P/2} f dt - \int_{T_P/2}^{T_P} f dt - \int_0^{T_P/2} (f_m - f) dt \tag{8.9}$$

$$= 2\int_0^T f dt - 2f_m T \tag{8.10}$$

$$S_{in} = \int_0^{T_P} f dt - \int_0^{T_P} (f_m - f) dt \tag{8.11}$$

$$= 2\int_0^T f dt + f_m (T_P - 2T). \tag{8.12}$$

Again discarding small terms, we have

$$\Phi \approx 2 \frac{\int_0^T f dt - f_m T}{T_P f_m}. \tag{8.13}$$

We recognise that in both cases, when $f = I$, ΦT_P is proportional to the expression for t_{eq} as used in the main text, but with different prefactors.